

M.TAYYIP GÜRBÜZ

IZMIR KATIP CELEBI UNIVERSITY

2019

**IZMIR KATIP CELEBI UNIVERSITY
GRADUATE SCHOOL OF NATURAL AND APPLIED SCIENCES**

**SIMULATIONS OF A NOVEL LOW PRESSURE COMPRESSION SYSTEM
FOR VARIABLE-SPEED MICRO TURBOFAN**



M.Sc. THESIS

Muhammet Tayyip GÜRBÜZ

Department of Mechanical Engineering

JUNE 2019

**IZMIR KATIP CELEBI UNIVERSITY
GRADUATE SCHOOL OF NATURAL AND APPLIED SCIENCES**

**SIMULATIONS OF A NOVEL LOW PRESSURE COMPRESSION SYSTEM
FOR VARIABLE-SPEED MICRO TURBOFAN**



M.Sc. THESIS

**Muhammet Tayyip GÜRBÜZ
(Y150105013)**

Department of Mechanical Engineering

Thesis Advisor: Asst. Prof. Dr. Sercan ACARER

JUNE 2019

İZMİR KATİP ÇELEBİ ÜNİVERSİTESİ
FEN BİLİMLERİ ENSTİTÜSÜ

DEĞİŞKEN HIZLI MİKRO TURBOFAN İÇİN ÖZGÜN BİR DÜŞÜK BASINÇ
KOMPRESÖR SİSTEMİNİN SİMULASYONLARI

YÜKSEK LİSANS TEZİ

Muhammet Tayyip GÜRBÜZ
(Y150105013)

Makine Mühendisliği Ana Bilim Dalı

Tez Danışmanı: Dr.Öğr.Üyesi Sercan ACARER

HAZİRAN 2019

Muhammet Tayyip GÜRBÜZ, a **M.Sc.** student of **IKCU Graduate School Of Natural And Applied Sciences**, successfully defended the thesis entitled “**Simulations of a Novel Low Pressure Compression System for Variable-Speed Micro Turbofan**”, which he prepared after fulfilling the requirements specified in the associated legislations, before the jury whose signatures are below.

Thesis Advisor :

Asst.Prof.Dr. Sercan ACARER
İzmir Katip Çelebi University

Jury Members :

Asst.Prof.Dr. Z.Haktan KARADENİZ
İzmir Katip Çelebi University

Assoc.Prof.Dr. Ünver ÖZKOL
İzmir Institute of Technology

Date of Submission : 20.05.2019

Date of Defense : 17.06.2019





To my family,



FOREWORD

First and foremost, I would like to thank my advisor, Asst.Prof.Dr. Sercan ACARER for his advises, guidance, support, encouragement, and inspiration through the thesis. His patience and kindness are greatly appreciated. I have been fortunate to have Dr. Acarer as my advisor and I consider it an honor working with him.

I am also grateful to my friends for their support, encouragement and contributions.

Lastly, I would like to thank my family who have supported and encouraged me during my graduate studies.

This thesis was supported by the NATO Science for Peace and Security Programme under grant G5202-Versatile UAV Engine Development and by the U.S. Office of Naval Research Global under award number N62909-17-1-2176.

June 2019

M.Tayyip GÜRBÜZ



TABLE OF CONTENTS

	<u>Page</u>
FOREWORD	vii
TABLE OF CONTENTS	ix
ABBREVIATIONS	xi
LIST OF TABLES	xiii
LIST OF FIGURES	xv
ABSTRACT	xvii
ÖZET	xix
1. INTRODUCTION	1
1.1 Gas Turbine (Aircraft) Engine	5
1.2 Types of Gas Turbine Engine.....	5
1.2.1 Turbojet	6
1.2.2 Turbofan	6
1.2.3 Turboprop.....	7
1.2.4 Turboshaft	8
1.3 Thermodynamics of Gas Turbine Engine	9
1.3.1 Compression process.....	10
1.3.1.1 Axial compressor	11
1.3.1.2 Centrifugal compressor	13
1.3.2 Combustion process	14
1.3.3 Expansion process	15
1.3.4 Exhaust process.....	16
1.4 Aerodynamics of Turbomachinery in Gas Turbines	17
1.5 Design Princibles and Methods of Turbomachinery	19
1.6 Goal and Scope Definition	24
1.6.1 Motivation.....	24
1.6.2 Scope of the current thesis	25
2. HIGH FIDELITY AERODYNAMIC SIMULATION (CFD)	
METHODOLOGY	28
2.1 The Solver Theory and Utilized Software.....	28
2.2 Experimental Validation of the Solver	32
3. DETAILED AERODYNAMIC OFF-DESIGN STUDY	35
3.1 Design of the Fan	35
3.2 Aerodynamics Off-design Performance Investigation	48
4. ENGINE PERFORMANCE SIMULATION	68
4.1 Core Turbojet Engine Performance Study	71
4.1.1 Matching of core compressor and turbine.....	71
4.1.2 Turbojet engine performance simulations.....	75
4.2 Adaptive Turbofan Engine Performance Study	79
4.2.1 Matching of fan and core compressor to turbine	79
4.2.2 Turbofan engine performance simulations	81

5. AEROMECHANICAL INVESTIGATION OF THE FAN BLADE	87
5.1 Static Structural Simulations	87
5.2 Finite Element Modal Analysis	89
5.3 Aerodynamic Damping Calculation	91
5.4 Unsteady Rotor-Stator Interaction Simulations.....	94
5.5 Harmonic Response Analysis.....	94
6. CONCLUSION.....	97
REFERENCES	99
CURRICULUM VITAE.....	103



ABBREVIATIONS

UAV	: Unmanned Aerial Vehicle
CVT	: Continuously Variable Transmission
LPC	: Low Pressure Compressor
SFC	: Specific Fuel Consumption
GTF	: Geared Turbofan Engines
OPR	: Overall Pressure Ratio
IGV	: Inlet Guide Vane
TET	: Turbine Entry Temperature
CFD	: Computational Fluid Dynamics
RANS	: Reynolds Avarage Navier Stokes
LPT	: Low Pressure Turbine
HPT	: High Pressure Turbine
SST	: Shear Stress Transport
RSM	: Reynolds Stress Model
LE	: Leading Edge
TE	: Trailing Edge
DCA	: Double Circular Arc
GE	: General Electric
SS	: Suction Side
PS	: Pressure Side
STP	: Standart sea-level temperature and pressure
C_{pr}	: Compressor pressure ratio
BPR	: Bypass ratio
EGT	: Exit Gas Temperature
MALE	: Medium-altitude long endurance
EO	: Enginer Order
ND	: Nodal Diameter
IBPA	: Inter Blade Phase Angle



LIST OF TABLES

	<u>Page</u>
Table 2.1 : Four different grid levels of NASA Rotor 37.	32
Table 3.1 : Preliminary design cycle requirements [28].	35
Table 3.2 : Overall performance comparison with and without IGV [28].	43
Table 3.3 : Overall performance study for four different stator configurations [28].	47
Table 4.1 : Comparison of engine technical specifications and simulation results...	78
Table 4.2 : Comparison of turbojet and adaptive turbofan at S.T.P. condition.	85
Table 4.3 : Reference turbojet and adaptive turbofan performance comparison at 10000 m altitude.	86



LIST OF FIGURES

	<u>Page</u>
Figure 1.1 : Gas turbine engine with its stages (Turbojet class) [22].	5
Figure 1.2 : Turbojet engine.	6
Figure 1.3 : Turbofan engine.	7
Figure 1.4 : Turboprop engine.	8
Figure 1.5 : Turboshaft engine.	8
Figure 1.6 : Gas turbine engine cycle (open cycle).	9
Figure 1.7 : Turbofan engine axial fan and compressor stages [23].	10
Figure 1.8 : Multistage axial compressor with its components [23].	11
Figure 1.9 : 3D-printed micro turbofan fan rotor of the current study.	13
Figure 1.10 : A centrifugal compressor stage.	14
Figure 1.11 : Combustors of combustion chamber in a gas turbine engine [23].	15
Figure 1.12 : Multistage axial turbine with its components [23].	16
Figure 1.13 : Exhaust nozzle and its components [22].	17
Figure 1.14 : Flow around an airfoil shaped fan blade (from the current study).	18
Figure 1.15 : Airflow behaviour through convergent and divergent nozzle.	19
Figure 1.16 : Representative sample of inlet and outlet velocity components on a radial turbomachinery.	21
Figure 1.17 : a) Combination of 3D & meridional view, b) Blade-to-blade view.	22
Figure 1.18 : Basic representation of the concept; a) Fan , b) CVT , c) variable bypass nozzle [21].	24
Figure 1.19 : Typical and proposed LPC systems comparison for similar bypass ratio [28].	25
Figure 2.1 : Spanwise measured and calculated results of Rotor 37 [34].	33
Figure 2.2 : Measured and calculated performance maps.	34
Figure 3.1 : Computational domain of designed LPC [28].	36
Figure 3.2 : Spanwise total pressure distribution (above), meridional pressure distribution (below) [28].	36
Figure 3.3 : Work and flow coefficient [28].	38
Figure 3.4 : Meridional Mach number distribution [28].	39
Figure 3.5 : Flow and metal angles [28].	40
Figure 3.6 : Blade solidity and chord length distributions [28].	40
Figure 3.7 : Spanwise distribution of De-Haller number and equivalent diffusion factor [28].	41
Figure 3.8 : Computational domain of LPC with IGV [28].	42
Figure 3.9 : Spanwise counter-swirl distribution [28].	42
Figure 3.10 : IGV effects on stator [28].	43
Figure 3.11 : Three-dimensional LPC system without IGV.	44
Figure 3.12 : Computational mesh of LPC at surfaces.	45
Figure 3.13 : Different stator configurations; (a) Case A (original geometry), (b) Case B, (c) Case C, (d) Case D [28].	46

Figure 3.14 : a) Final LPC geometry, b) Spanwise pressure distribution comparison [28].	48
Figure 3.15 : LPC system performance maps.	49
Figure 3.16 : Comparison of Throughflow code and CFD numerical solver at design point.	50
Figure 3.17 : LPC system velocity streamlines.	51
Figure 3.18 : Relative Mach distribution for three operating conditions; near-choke (top), design point (mid), near-stall (bottom).	52
Figure 3.19 : Static Pressure chordwise distribution for 0.9 (top), 0.5 (mid), and 0.1 (bottom) spans.	54
Figure 3.20 : Static Pressure distribution on fan rotor for different operating conditions.	55
Figure 3.21 : Three operating point streamlines on rotor blade suction side from different perspectives, View 1 (left), View 2 (right).	56
Figure 3.22 : Streamwise distribution of absolute Mach at design point (top) and near-stall (bottom).	58
Figure 3.23 : Streamwise meridional velocity evaluation at design point.	58
Figure 3.24 : Streamwise total pressure distribution.	59
Figure 3.25 : Vorticity characteristics of the flow in the streamwise direction (Higher values were clipped).	60
Figure 3.26 : Shear strain streamwise evaluation (Higher values were clipped).	60
Figure 3.27 : Streamwise evaluation of turbulent viscosity.	60
Figure 3.28 : Relative Mach distribution for different shaft speeds; 100% design speed (top), 80% speed (mid), 60% speed (bottom).	62
Figure 3.29 : Static Pressure chordwise distribution for 0.9 (top), 0.5 (mid), and 0.1 (bottom) spans.	63
Figure 3.30 : Near tip section (0.98 span) Relative Mach distribution.	64
Figure 3.31 : From 0.95 span to 0.995 span tip clearance flow influence.	65
Figure 3.32 : Entropy generation and blade tip flow characteristics (lower and higher values were clipped).	66
Figure 4.1 : AMT Nike core compressor performance maps.	69
Figure 4.2 : AMT Nike turbine performance maps.	70
Figure 4.3 : Core turbojet engine sections and its indices [25].	71
Figure 4.4 : Turbojet engine operating line on each performance maps.	74
Figure 4.5 : Turbojet and turbofan engine operating lines across each performance maps.	80
Figure 4.6 : Turbofan engine sections and its indices [25].	81
Figure 5.1 : Aeromechanical study flow chart.	87
Figure 5.2 : Rotor blisk design, computational domain and boundary conditions.	88
Figure 5.3 : Total deformation and max equivalent Von-misses stress.	88
Figure 5.4 : Campbell Diagram of the fan rotor.	90
Figure 5.5 : Resonanced mode shapes.	91
Figure 5.6 : Imported nodes of the specific mode.	92
Figure 5.7 : Non-normalized and normalized aerodynamic damping as a function of several IBPA's near 33000 rpm.	93
Figure 5.8 : Unsteady complex real (left) and imaginary (right) pressure mapping.	95
Figure 5.9 : Deformation-frequency response graph.	95
Figure 5.10 : Alternating stress-frequency response graph.	95

SIMULATIONS OF A NOVEL LOW PRESSURE COMPRESSION SYSTEM FOR VARIABLE-SPEED MICRO TURBOFAN

ABSTRACT

Unmanned Aerial Vehicles (UAVs) are commonly propeller-driven and intended towards low-speed applications. The challenges on the field demand cost-efficient, high-speed and longer range applications of micro-scaled jet engines which can be applied both ‘loiter’ and ‘fly-fast’ modes. The micro-turbojet applications on the field have shorter ranges because of higher rates of fuel consumption. On the other hand, turbofan engines instead of turbojets are limited due to the price and complexity problems in micro-scales. In order to cope with this problem and meet the demand on the field, an existing basic turbojet engine was converted into a single spool turbofan without using additional components of booster and low pressure turbine. Normally, this situation emerges matching problems since two spools are required to adjust the fan speed independently. A simple solution was to use a Continuously Variable Transmission (CVT) gearbox to adjust optimal speed for the fan. As a result, missing of the positive functionality of the booster would lump into the fan root to form a unified low pressure compression system (unified-LPC), to the author’s best knowledge, it is the first time in the open literature.

Such a unified-LPC demands unique characteristics of having an extreme twist, very high pressure ratio and mass flux at the core section than at the bypass section so as to obtain maximum thrust and efficiency. Correspondingly, many challenges arise with respect to aerodynamics and structural perspective. The former one includes the difficulty to design a unified fan and booster concept within a single stage compressor. Resultant design demands a transonic and highly loaded stator design because of the excessive root mass flux which causes high mixing losses downstream of the stator. Combining this unconventional design with the desired high-area-ratio diffuser shaped duct which is the connection between the fan stage and the engine core compressor, produces notable disability for the unified-LPC to pass the required pressurized air. The latter one includes the vibrational response of an excessively twisted fan rotor. Furthermore, a systematic existence of negative aerodynamic damping (flutter) may show that the concept is infeasible.

In light of these challenges, this thesis aimed to investigate detailed aerodynamics (predominantly) and aeromechanical behaviour of a suitable unified-LPC designed simultaneously with the co-researchers of a research group. ANSYS CFX solver, validated against Rotor 37 test case, was used to obtain sea-level corrected off-design characteristics of the LPC. Detailed aerodynamic characteristics of the unified-LPC system were analyzed for design and different shaft speeds considering different operating conditions. Moreover, mixing loss and tip leakage flow characteristics of such an unconventional LPC system were examined for design point operating condition. In the aeromechanical section, Modal analysis was performed in ANSYS Mechanical to obtain resonance points (Campbell Diagram) of the rotor natural

frequencies originating from the stator excitation frequency. Mode shapes were exported into CFX to perform CFD simulations with periodically moving mesh and aerodynamic damping calculations were made. Then, forced response analysis in ANSYS Harmonic Response solver was performed to estimate the life cycle of the fan. It was shown that the unified-LPC has flutter-free (modes are damped) behaviour, indicating an infinite life.

Finally, the estimated off-design characteristics of the unified-LPC was simulated in an in-house developed map-based engine thermodynamic code. The code was validated against the existing core engine results. 105% increase in maximum thrust and a 33% decrease in specific fuel consumption was shown with the proposed concept over the existing one.



DEĞİŞKEN HIZLI MİKRO TURBOFAN İÇİN ÖZGÜN BİR DÜŞÜK BASINÇ KOMPRESÖR SİSTEMİNİN SİMULASYONLARI

ÖZET

İnsansız Hava Araçları (İHA) genellikle pervaneli ve düşük hızlı uygulamalara yöneliktir. Sahadaki zorluklar, hem “keşif” hem de “hızlı uçuş” modlarına uygulanabilen, mikro-ölçekli jet motorlarının düşük maliyetli, yüksek hızlı ve daha uzun menzilli uygulamalarını gerekli kılmaktadır. Bu alana yönelik mikro-turbojet uygulamaları yüksek yakıt tüketim oranları nedeniyle çok kısa menzillere sahiptir. Öte yandan, turbojetler yerine düşünülebilecek turbofan motorları, mikro ölçeklerde fiyat ve yapı karmaşıklığı sorunları ile kısıtlanmıştır. Bu sorunla başa çıkmak ve sahadaki talepleri karşılamak adına var olan bir mikro-turbojet motoru, takviye (booster) kompresörü ve düşük basınçlı türbin ilave bileşenleri kullanılmadan tek-milli bir turbofana dönüştürülmektedir. Normalde bu durum, fan hızını bağımsız olarak ayarlamak için ikili mil sistemi gerektirdiğinden eşleşme sorunları ortaya çıkarır. Basit bir çözüm olarak fanın optimum hızını ayarlamak için Sürekli Değişken Aktarma Sistemi kullanılmaktadır. Sonuç olarak, takviye kompresörünün olumlu işlevinin eksikliği fan kökünde toplanmış bir birleşik Düşük Basınç Kompresörü sistemi tasarımı oluşturur. Bu konsept yazarların bilgisi dahilinde açık literatürde ilk kez uygulanmaktadır.

Böyle bir birleşik Düşük Basınç Kompresörü, maksimum itki ve verim elde etmek için core tarafında bypass tarafına kıyasla kanat yapısında aşırı büküm, çok yüksek basınç oranı ve kütle akışına sahip olmak gibi benzersiz özellikleri gerekli kılmaktadır. Buna bağlı olarak, aerodinamik ve yapısal bakımdan birçok zorluk ortaya çıkmaktadır. Bu birinci durum, tek kademeli bir kompresör içinde birleşik bir fan ve takviye kompresör konsepti tasarlama zorluğunu içerir. Ortaya çıkan tasarım, statorun aşağı akışında yüksek karışım kayıplarına neden olan aşırı kök kütle akışı nedeniyle bir transonik ve çok yüklü stator tasarımını gerektirir. Bu sıradışı tasarımın, fan kademesi ile çekirdek motor kompresörü arasındaki bağlantı olan ve istenen yüksek alan oranlı difüzör şekilli kanalla birleştirilmesi, birleşik Düşük Basınç Kompresörünün gerekli basınçlı havayı geçirmesi adına dikkate değer bir engel oluşturur. Bu ikinci durum ise aşırı bükülmüş bir fan rotorunun titreşimsel tepkisini içerir. Ayrıca, negatif aerodinamik sönümlenmenin (titreşim) sistematik varlığı konseptin uygulanabilir olmadığını gösterebilir.

Bu zorluklar ışığında, bu tez, bir araştırma grubunun ortak araştırmacılarıyla eşzamanlı olarak tasarlanan uygun bir birleşik Düşük Basınç Kompresörünün ayrıntılı aerodinamik (ağırlıklı olarak) ve aeromekanik davranışını incelemeyi amaçlamıştır. Düşük Basınç Kompresörünün deniz seviyesinde düzeltilmiş performans karakteristiğini elde etmek için Rotor 37 test kompresörüne göre doğrulanan ANSYS CFX çözücüsü kullanılmıştır. Birleşik Düşük Basınç Kompresör sistemin ayrıntılı aerodinamik karakteristiği, farklı çalışma koşulları dikkate alınarak

tasarım ve farklı mil hızları için analiz edilmiştir. Ayrıca, böyle alışılmadık bir Düşük Basınç Kompresör sisteminin karışım kayıpları ve kanat uç sızıntı akış karakteristikleri de tasarım noktası çalışma koşulu açısından incelenmiştir. Aeromekanik bölümünde ise stator uyarım frekansından kaynaklı rotor doğal frekanslarının rezonans noktalarını (Campbell Diyagramı) elde etmek için ANSYS Mechanical da Modal analiz yapılmıştır. Mod şekilleri, periyodik olarak hareketli ağ ile CFD simülasyonları gerçekleştirmek için CFX'e girdi olarak verilmiş ve aerodinamik sönümlenme hesaplamaları yapılmıştır. Daha sonra, fanın ömrünü tahmin etmek için ANSYS Harmonic Response çözücüsünde zorlamalı tepki analizi gerçekleştirilmiştir. Birleşik Düşük Basınç Kompresörünün sonsuz bir ömre işaret eden titreşimsiz (modlar sönümlenmiş) bir davranışa sahip olduğu gösterilmiştir.

Son olarak, birleşik Düşük Basınç Kompresörünün tahmini performans karakteristiği, in-house bir performans haritası tabanlı motor termodinamik kodunda simüle edilmiştir. Kod mevcut çekirdek motor sonuçlarına karşı doğrulanmıştır. Önerilen turbofan tasarımı ile mevcut motor tasarım durumuna kıyasla maksimum itkide %105 artış ve yakıt tüketiminde %33 oranında düşüş görülmüştür.

1. INTRODUCTION

Unmanned Aerial Vehicles (UAV) are commonly known and used in recent years. The research studies about them are progressively being increased due to their several advantages such as remote control by human or autonomous control by onboard computers and sustained level flights. Their propulsion technology is generally utilized from reciprocating engine which drives a propeller. This engine is the key elements of recent UAV propulsion technology in order to develop efficient aerial vehicles. Considering this, a stepped piston engine [1] which combines two-cycle and four-cycle piston engines by eliminating their disadvantages was examined for UAV applications. Its performance was compared to two and four cycle engine types separately by respect to Specific Fuel Consumption (SFC) and noise and heat signature levels. Further multi-fuel development was applied to improve this specific engine performance. Hybrid propulsion technology specified by UAVs are also in demand. Lieh et al [2] discussed the advantages of hybrid electric propulsion with its clean source of energy, low noise and reduced heat releases comparing to Internal Combustion Engines. The study also presented the history of hybrid propulsion technology and its challenges for future UAV applications. Cirigliano et al. [3] studied several different propulsion systems from Internal Combustion Engines (two and four stroke types) to Gas turbines and hybrid Electric Motors at medium subsonic levels and compared them for long endurance flight. Power, size and weight were the main considerations in order to evaluate the engines. The study showed that reciprocating engines, especially diesel types presented more efficient performance with reduced SFC comparing to gas turbines. Yet, the reliability issue, noise signature and size had significant importance for long range flights. On the other hand, hybrid electric motors was emphasized for their potential to increase the performance in the future by superconductivity technology.

Although these studies have been made great progress in UAV propulsion, the technology still demands further development in the field that the majority are low speed applications within a limited efficiency levels. Besides, reciprocating engines

are not suitable for high-speed flights that severe vibrations happen in engine components with high level of noise and excessive heat release. Therefore, future UAV applications require for more advanced propulsion technology which provides high-speed flights, long-range capability and low-cost applications for combat, rescue and surveillance in risky and hazardous environments. To achieve long range flight and high-speed application over UAVs, small-scale turbojet engine design and its integration was investigated by some researches [4;5]. However, the main challenge for turbojets from small-scales to larger platforms is its inefficient off-design performance and poor fuel consumption.

As an alternative, larger platforms with improved performance characteristics also corresponding to efficient fuel burn, turbofans which are derived from the turbojets are highly demanded. There are research fields focusing on turbofans to obtain more efficient and optimized designs with numerous research efforts for decades. One of the main obstacles for such a complex structure is its aerodynamical and thermomechanical conformity and matching for each component. Especially, uncontrolled tip leakage phenomenon has a great impact on overall performance, specifically in SFC of the engine. Therefore, a global optimization study coupling with 3D transient numerical solutions of a turbofan structure [6] focused on minimizing tip leakage flow of high pressure compressor. The multidisciplinary optimization of whole-engine achieved 3.44% improvement on SFC of the test engine. On the other hand, size of tip clearance gap has also significant importance on the engine performance. Wadia et al. [7] studied the role of tip clearance level (tip clearance to tip blade chord ratio) from 0.27 to 1.87%. Results showed that while tip clearance level was increasing from minimum to maximum, efficiency considerably dropped by 6% and flow range by 30%.

Three-dimensional blade shaping is another field with its importance especially for transonic compressor/fan rotor performance of the engine. Nature of transonic aerodynamics allows shock structure at the blade and its interference with secondary flows requires an optimization process in order to improve better propulsion characteristics. Benini and Biollo [8;9] investigated axial sweep and tangential lean effects on rotor blade performance of typical NASA Rotor 37 transonic compressor. They observed that especially forward lean (blade stacking line inclination through the direction of rotation) on blade considerably increases overall performance

approximately 1.5% by moving shock structure downstream and reducing its strength at a minor cost of operating range. Another study [10] examined a conventional transonic compressor rotor developed by Darmstadt and MTU Aero Engines by applying aft sweep on rotor blade (downstream axial inclination of rotor blade stacking line). Comparing with conventional design, aft-swept rotor showed an 1.5% improvement of efficiency at design point with a wider operation range.

Bypass nozzle area control option on turbofans has also significant effect for overall engine performance. Efficient fuel burn corresponding to reduced SFC could be achieved by applying variable bypass nozzle on a turbofan architecture. A study [11] showed that using such a nozzle configuration reduced fuel consumption by 10% at take-off and 2% during cruise condition. This concept also improved aeroacoustic performance as reducing the level of noise about 1 to 2 dB for different operating conditions. Further study about the effect of bypass nozzle area change having a great effect on aeroacoustic performance for a turbofan can be found in Ref. [12].

There are further efforts to develop eco-friendly core engine concepts for the future emission goals within NEWAC Framework (New Aero-engine core concepts) [13;14]. One of the main focus of these efforts is on Intercooled Recuperative Core concepts. Effect of recuperation in turbofan engine was studied by Goulas et al. [15] and showed the possibility of SFC improvement at a cost of relatively low pressure drop. Effect of recuperator and intercooling combination in a turbofan engine was detailly presented in another study [16] by a global optimizer considering performance maps, recuperator and intercooling losses, take-off, cruise conditions and more of them. The resulted SFC improvement was 5.56% percent for intercooled and recuperated engine concept comparing to conventional design. It was achieved by modifying fan, compressor and LPT (low pressure turbine) design.

For future emissions goals, another focus of these efforts is on active core structures applicable with geared turbofan engines (GTF) for long range applications. Kyprianidis et al. [17;18] proposed intercooled core engine cycle combined with geared fan and increased Overall Pressure Ratio (OPR) in order to provide 2020 service entry requirements for eco-friendly engines. Focusing on SFC improvement by emissions reduction and engine structure weight and drag issue, intercooled core with GTF engines showed a potential to reach future goals. Ultra high-bypass ratio or open rotor aero engine also known as contra-rotating engine concept was detailly

investigated by the NASA research team with respect to its off-design performance and engine weight. Then, the results were compared to GTF and direct-drive Turbofan concepts [19]. Although, open rotor engine was much heavier (because of the open rotor's weight and size) comparing to GTF and direct-drive turbofan, the SFC reduction was around 13% at the highest altitude (10000 m) and around 42% at sea level. For further studies, Alexiou et al. [20] investigated a conventional GTF and estimated 10% weight reduction by engine simplification with the help of counter-rotating rotor architecture. As a result, the weight reduction provided 3.2% total SFC improvement for the engine.

Most of the gas turbine engine types has been shown significant improvements with respect to off-design performance and overall efficiency especially in the recent years, yet micro-scaled gas turbine (under 2 kN of thrust) is the only one have been left to be investigated. In the market search, application of gas turbines for UAV propulsion technology is generally restricted by reciprocating engines and turbojets with a lack of micro-scaled advanced turbofans [21]. The reviewed concepts are not suitable for those small engines, since cost and simplicity are the main problems together with demanding high engine performance at high-subsonic and transonic flights. Considering these challenges and the gap on the field, an existing micro-turbojet was converted into a single spool turbofan without using additional booster and low pressure turbine (LPT). To adjust the fan speed independently, a CVT gearbox was used. As a result, missing of the positive functionality of the booster was integrated into the fan root to form a unified fan and booster, in other words unified low pressure compression system (unified-LPC). In this direction, this thesis focused on the unique unified-LPC for a micro-turbofan engine that was converted from an existing micro-turbojet. The thesis will examine this LPC system in three main subtitles;

- Off-design and aerodynamics performance study of the LPC system
- With the integration of the LPC system, the performance improvement of the micro-turbofan over the existing micro-turbojet by carrying out engine performance simulations
- Structural integrity and vibrational behaviour of the LPC rotor blade, in other words aeromechanical study of the fan rotor

In conclusion, such an innovative concept will be the first time in the open literature. It is expected to present a unique guidelines for future UAV engine applications, outside of the conventional fan (LPC) design concepts.

1.1 Gas Turbine (Aircraft) Engine

Gas turbine engine is commonly used engine type in the aviation industry. It is the main and the most complex part of an aircraft as called ‘jet engine’ as well. This component is responsible for the propulsion system of an aircraft and generation of mechanical power.

The operating gas of a gas turbine engine is atmospheric air. The propulsion and the mechanical power is produced using the air as an operating gas by five main processes; Air intake, Compression, Combustion, Expansion (Power Generation) and Exhaust (Propulsion). The first process is to suck air into gas turbine engine by a rotating fan or a compressor. Air is then compressed to higher pressure through compression stage. The fuel is then sprayed over the compressed air and ignited in the combustion chamber. Air with high temperature and pressure, enters the turbine stage. The turbine extracts energy from the high energized air and converts it into mechanical shaft power, and expands it down to the exhaust pressure. Lastly, exhausted gas is used to produce thrust. A commonly used gas turbine engine is shown in Figure 1.1.

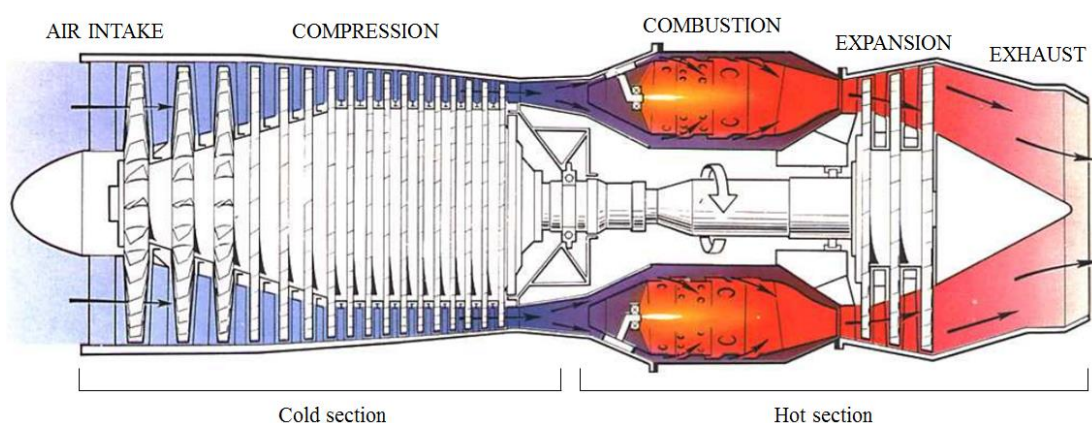


Figure 1.1 : Gas turbine engine with its stages (Turbojet class) [22].

1.2 Types of Gas Turbine Engine

There are four types of gas turbine engines;

- Turbojet
- Turbofan
- Turboprop
- Turboshaft

1.2.1 Turbojet

Turbojet is a type of gas turbine engine produces all of its thrust by ejecting a high energy gas stream from the engine exhaust nozzle. It is named as a gas generator (core engine) with propelling nozzle.

Turbojet engine works on the principle on accelerating relatively small mass of air to a higher speed. It is not efficient in subsonic speeds because of the low mass flow rate levels and higher speed of the exhaust stream than aircraft itself. This type of engine reaches its optimum (peak) efficiency level when the accelerated air approximates the aircraft speed (approximately in Mach=2). Turbojet engine is used in high speed military aircrafts and missiles. A simplified representation of a turbojet engine is shown in Figure 1.2.

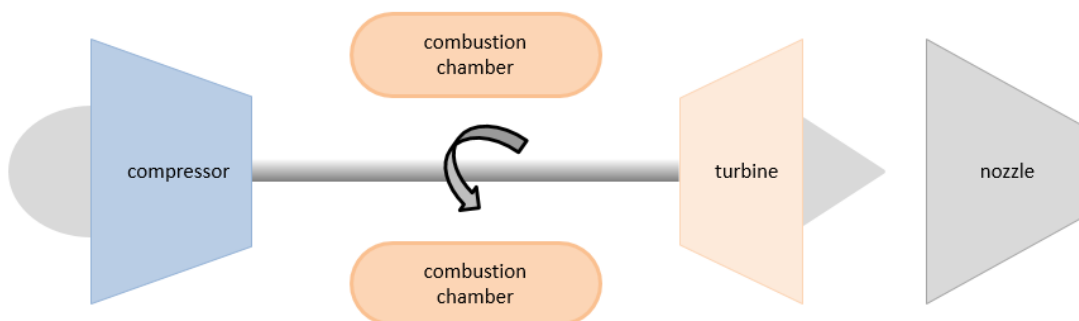


Figure 1.2 : Turbojet engine.

1.2.2 Turbofan

Turbofan engine produces thrust with a combination of jet core stream and by-passed air which is accelerated by a ducted fan that is driven by jet core. It is sometimes referred to as a fanjet or by-pass engine. This engine is commonly used in commercial aviation jets and civil aircrafts.

Turbofan engine works on the principle on accelerating large mass of air to a relatively low (subsonic-near transonic) speed. Turbofan engine with a large fan at the front sucks air in , most of the air flows around the outside of the core engine and

by-passes. This by-passed air makes engine quieter and gives more thrust at low speed. The objective of this by-pass system is to increase engine's thrust without effecting the fuel consumption. This process achieved by increasing total mass flow in return reducing the velocity within the same total energy supply. Therefore, turbofan engine is efficient by more closely matching the speed of the exhaust flow to the aircraft speed. A schematic demonstration of a turbofan is shown in Figure 1.3.

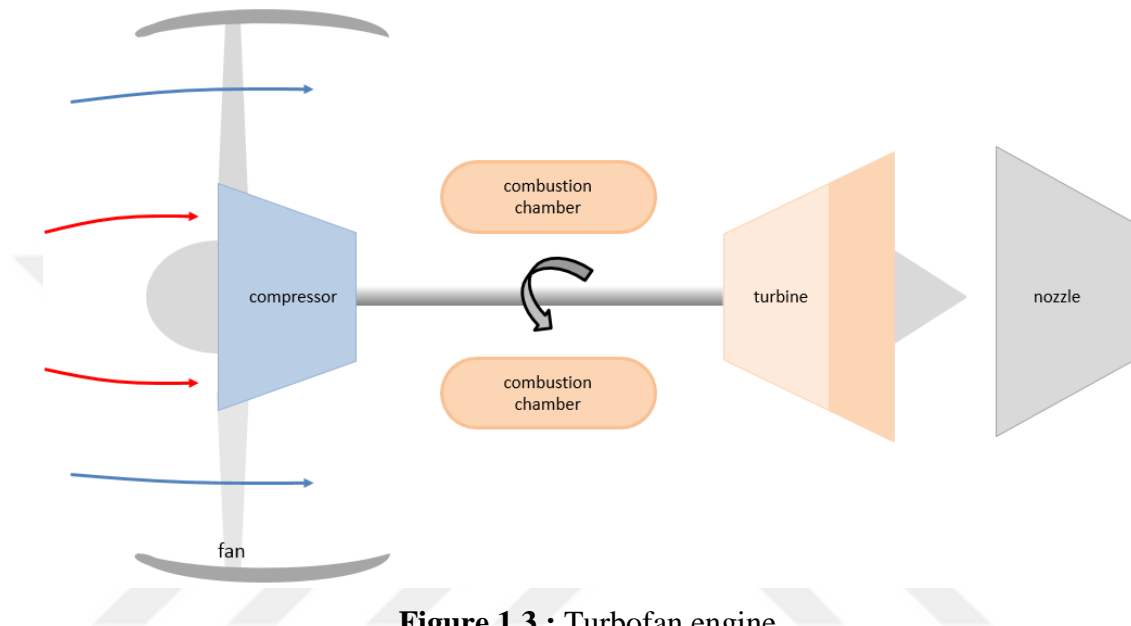


Figure 1.3 : Turbofan engine.

1.2.3 Turboprop

Turboprop is a jet engine attached to a propeller. The turbine at the back of the engine is turned by hot gases, then it rotates a shaft that drives the propeller. Very high portion of air is flown through the propeller. The propelling nozzle provides a relatively small proportion of the thrust and most of the thrust is generated by the propeller.

Turboprop equipped aircraft is more efficient at lower flight speeds (less than mach 0.7), and it has better fuel consumption per seat-mile and requires considerably shorter landing field than a same size turbojet or turbofan powered aircraft. Some small airliners and transport aircrafts are powered by turboprops. A simplified representation of a turboprop engine is shown in Figure 1.4.

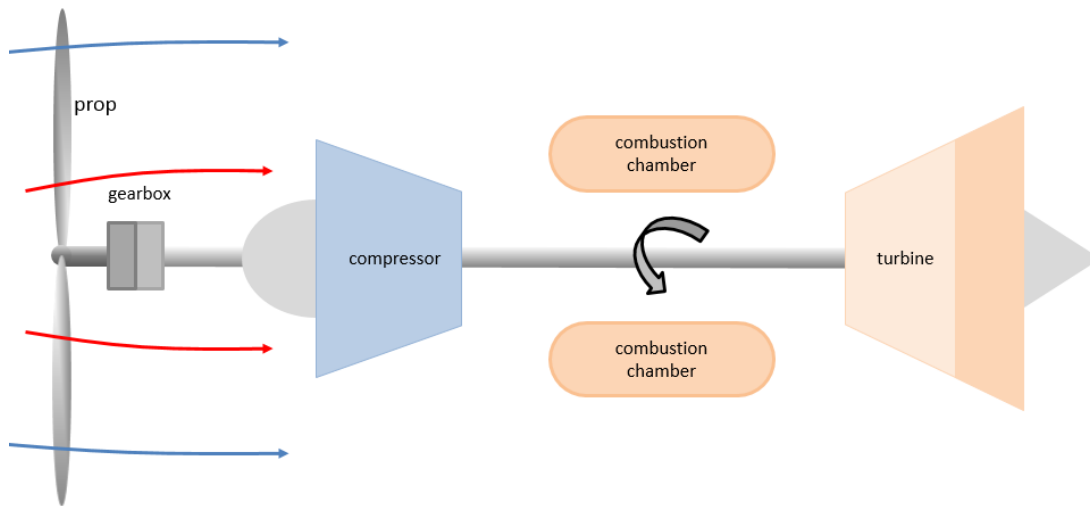


Figure 1.4 : Turboprop engine.

1.2.4 Turboshaft

A turboshaft, a variant of a gas turbine engine is designed to produce shaft power to drive the machinery instead of producing thrust. The mechanism of the turboshaft allows a helicopter rotor to rotate freely and at a constant speed to stabilize the amount of power produced notwithstanding core engine (generator) speed modulation due to the mass change. Turboshaft engines are desired for a small but powerful, lightweight engine application, and for reliability as well. It is used for helicopters, auxiliary power units, tanks, boats, and ships.

A turboshaft engine has a very similar concept like a turboprop with only minor differences. The main difference between these engines is that the turbine shaft of the turboshaft engine is connected to a gearbox that drives the rotor shaft instead of driving a propeller (Figure 1.5).

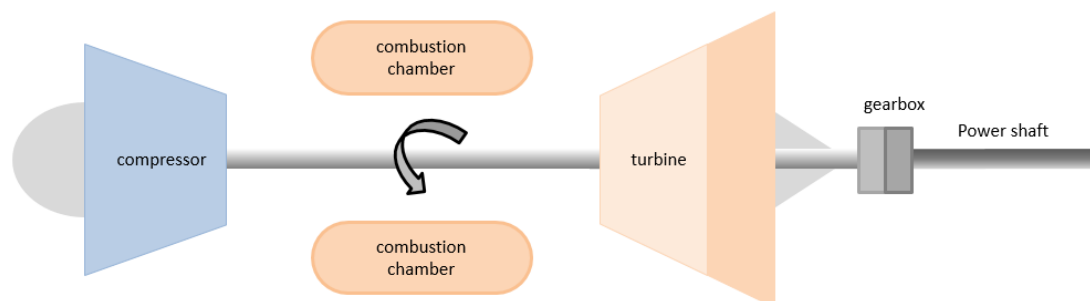


Figure 1.5 : Turboshaft engine.

1.3 Thermodynamics of Gas Turbine Engine

Gas turbine engines are used to generate power for an aircraft or for a power plant, or to produce propulsion to move an aircraft. As mentioned before, there are various types of gas turbine engines. However, they have some points in common; a compressor to compress the operating gas, a combustor for a combustion process and a turbine to generate power, as a result the process for all types has a similarity in point of thermodynamic cycle of the engine. To understand how to produce thrust or to generate power, the basic thermodynamics of the process and operating gas should have known.

Brayton Cycle represents this basic thermodynamics of the process in gas turbine engines. It is used as a thermodynamic cycle in gas turbine engines and firstly developed by George Brayton in 1870 to be used in piston engine. Today, it is commonly used in gas turbine engines that compression and expansion processes occur.

Gas turbine engines generally operate on an open cycle (Figure 1.6). Fresh air is sucked by a compressor in order to increase mainly the pressure of the engine. High pressurized air is burned with the help of fuel in a combustion chamber at a constant pressure. The mixed gas having high pressure and temperature then enters to turbine stage and its energy is extracted by turbine to generate power. The expanded gas is discharged from the turbine and exhausted to the atmosphere (no circulation), resulted cycle to be called as an open cycle [23].

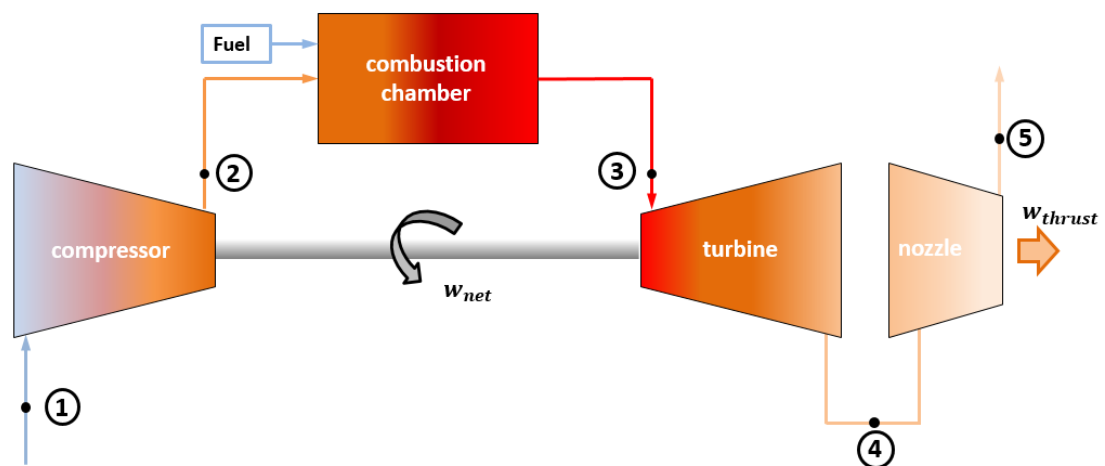


Figure 1.6 : Gas turbine engine cycle (open cycle).

In this cycle;

1-2 : Compression Process

2-3 : Combustion Process

3-4 : Expansion Process

4-5 : Exhaust Process

1.3.1 Compression process

In the compression process, a fan or a compressor or both provide the compression process of the gas turbine engine. A fan moves large amounts of air with a low increase in pressure. However, a compressor is a component that rises relatively small amounts of air into higher levels of pressure with many stages and making the air denser by cramming it into a small space. An example for an axial fan and compressor stages (cascades) is presented in Figure 1.7.

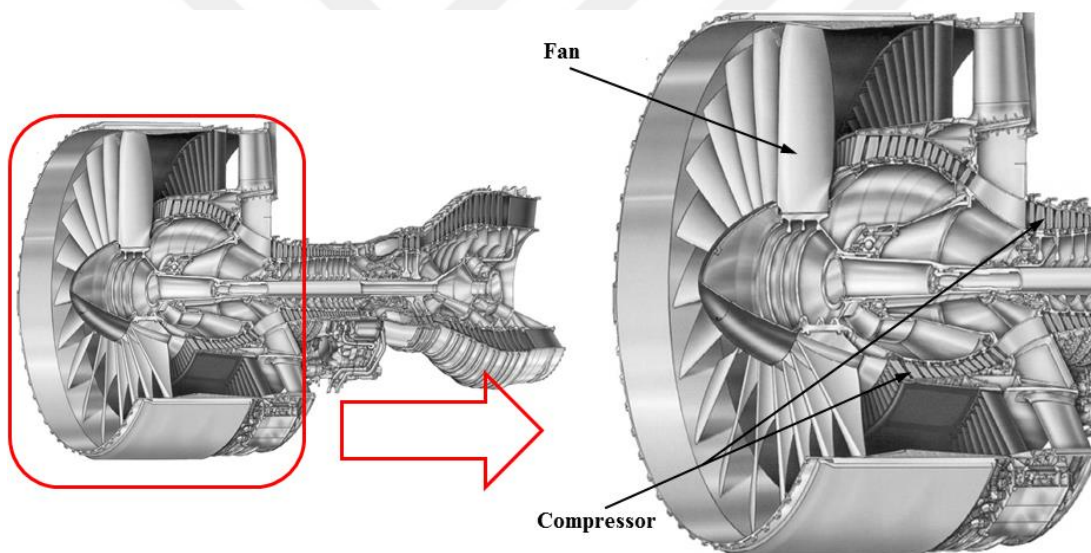


Figure 1.7 : Turbofan engine axial fan and compressor stages [23].

It should be known that compressor and its variations work against nature. As a consequence, there are more compressor stages than turbine stages in a typical gas turbine engine. Besides, compressor blades have less curvature in order to accomplish desired pressure ratio by sharing pressure contribution within the multistage rows.

There are two basic configurations for a gas turbine engine compressors: axial compressor and centrifugal compressor.

1.3.1.1 Axial compressor

The air flows in and flows out across the component parallel to the axis of rotation in an axial compressor. Axial compressor is preferable to use generally in medium and large thrust gas turbine applications in comparison to centrifugal compressor which consumes far less air within the same frontal area. This means that an axial compressor is more efficient than a centrifugal compressor due to amount of air mass flux. If a centrifugal compressor is designed to consume same amount of air, it would be too heavy and too large in the cross-sectional area. Since an axial compressor allows larger amount of air to flow in and out, the engine gives also more thrust for the same frontal area. It is known that the amount of air is one of the key factors (the other is the velocity of air) in determining the amount of thrust.

A similar average axial compressor increases the pressure by only a factor of approximately 1.2, while a centrifugal compressor does this work by a factor of 4. However, axial compressor has an ability to link together several stages easily and produce multistage axial compressors. A multi-stage unit employing alternate rows of 'rotating (rotor) blades' and 'stationary (stator) vanes' to accelerate and diffuse the air until the required pressure rise is obtained (Figure 1.8). This advantage gives higher pressure increase multiplied from row to row and has led to the adoption of axial compressors in most engine designs.

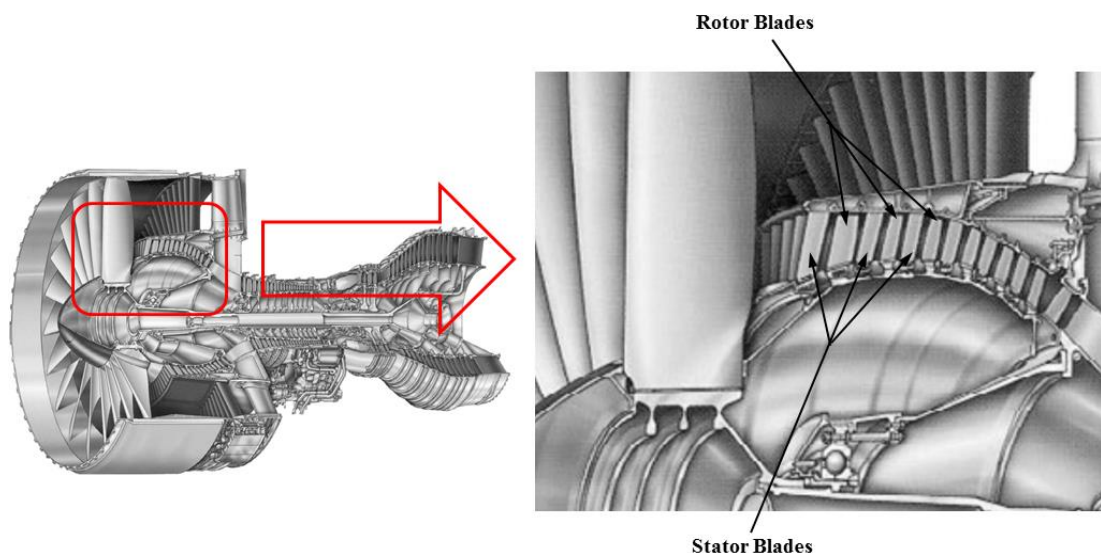


Figure 1.8 : Multistage axial compressor with its components [23].

Axial compressors have some some advantages and disadvantages;

Advantages:

- Capable of handling large volumes of airflow and high-pressure ratio
- Smaller frontal area for a given mass flow rate
- Axial-through flow, allowing high efficiency levels

Disadvantages:

- More critical to foreign object damage
- Expensive to manufacture
- Much heavier in comparison to the centrifugal compressor in point of the same compression ratio.
- Less reliable from the aeromechanical perspective

As mentioned, one of the other type of axial flow compressors is fan stages.

‘Fan stage’ of a gas turbine engine exists in turbofans. It is located upstream air intake station of the core engine and the duct of the fan surrounds the core engine. The upstream air flows through the fan stage before splitted between the core and the by-pass ducts. As a result, a turbofan gets some of its thrust from the core section and some of its thrust from the by-passed air. The ratio of the air that by-passes to the air that goes inside the core is called the bypass ratio. Fan stage is suitable arrangement for passanger and transport aircrafts flying at just below the speed of sound. The fan may be coupled to the front of a number of core compressor stages (two shaft engine) or a separate shaft driven by its own turbine (three shaft engine).

While a fan is similar in principle to the core compressor stage, the tip diameter of a fan rotor is considerably larger. By-pass flow pressure rises almost 1.6 times the inlet pressure. This is achieved in the fan by utilizing very high tip speed and high supersonic inlet (Mach 1.5) velocity. The capability of this type of compressor stage achieves the cycle requirement of

- high flow per unit of frontal area
- high efficiency
- high pressure ratio

in a single rotating blade row without IGV (inlet guide vanes) within an acceptable engine diameter. Thus, keeping weight and mechanical complexity at an acceptable level. 3D printed fan rotor of the current study is shown in Figure 1.9.

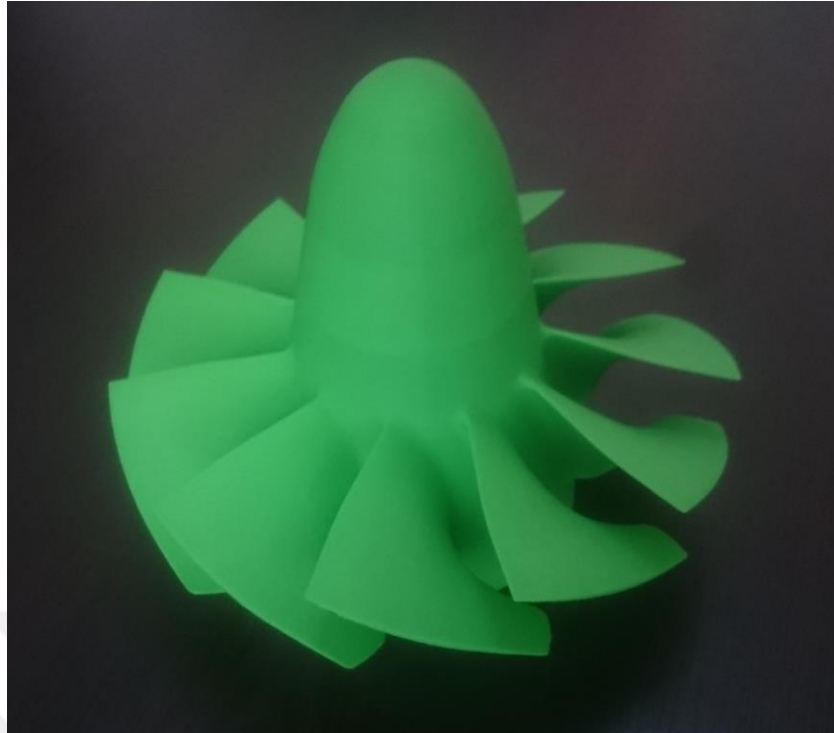


Figure 1.9 : 3D-printed micro turbofan fan rotor of the current study.

1.3.1.2 Centrifugal compressor

The air flows in, through the impeller parallel to the axis of rotation and flows out, from the compressor turned perpendicular to the axis of rotation. The impeller is supported in a casing that also contains a ring of diffuser vanes instead of stators used in axial compressors. Centrifugal compressor is generally used in gas turbine applications requiring small thrust especially in turboprop/turboshaft engines. Looking from the pressure ratio in a single stage operation, a centrifugal compressor is much better than an axial compressor. A basic centrifugal compressor can increase the pressure by a factor of 4.

The impeller is rotated by the turbine and sucks the air continuously through the inlet. Centrifugal principle drives the air radially outwards from the impeller tip, accelerating it and causing a pressure rise. The air then passes into the diffuser section where the passages form divergent nozzles that convert kinetic energy into pressure rise. Pressure rise is provided generally half of this from the impeller section and half of this from the diffuser section. A centrifugal compressor (impeller and diffuser components) is shown in Figure 1.10.

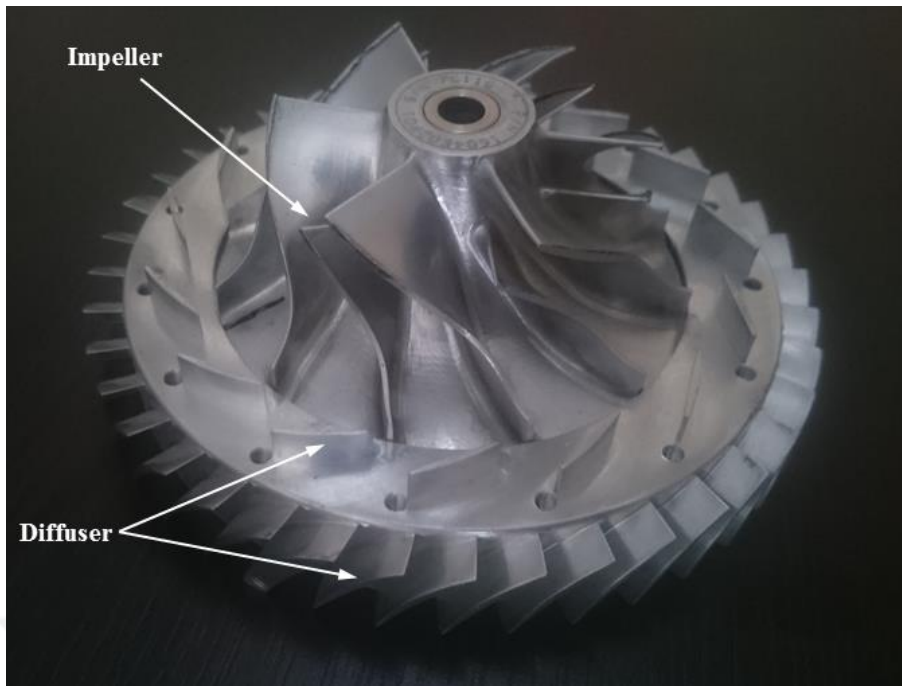


Figure 1.10 : A centrifugal compressor stage.

Centrifugal compressors have some advantages and disadvantages;

Advantages;

- Lightweight
- High-pressure rise per stage
- Simplicity of manufacture, therefore low cost

Disadvantages;

- Large frontal area for given airflow
- More than two stages are not practical because of losses in turns between stages

1.3.2 Combustion process

Combustion chamber, also called as combustor or burner is fed by high pressurized air, mixed with the fuel and burned. As the high-pressure air which is produced at the compression process and the fuel are burned, the resulting mixture of gas has high pressure and high temperature. The mixture expands throughout the turbine stages to produce shaft power and exhausts from the nozzle to produce thrust. The combustion process must be completed with the minimum pressure drop and maximum heat release before entering the turbine stage in order to provide required energy conversion to shaft power and/or to thrust production.

After compression process, the high pressurized air arrives combustion chamber (see Figure 1.11) with a very high speed. However, the combustion chamber operation must maintain stable during the process for efficient combustion. To maintain the stability, combustors are designed to mix air and fuel carefully and ignite them.

Combustion chamber is a key factor determining some properties of gas turbine engine;

- fuel efficiency
- thrust level due to efficient burn
- levels of emissions

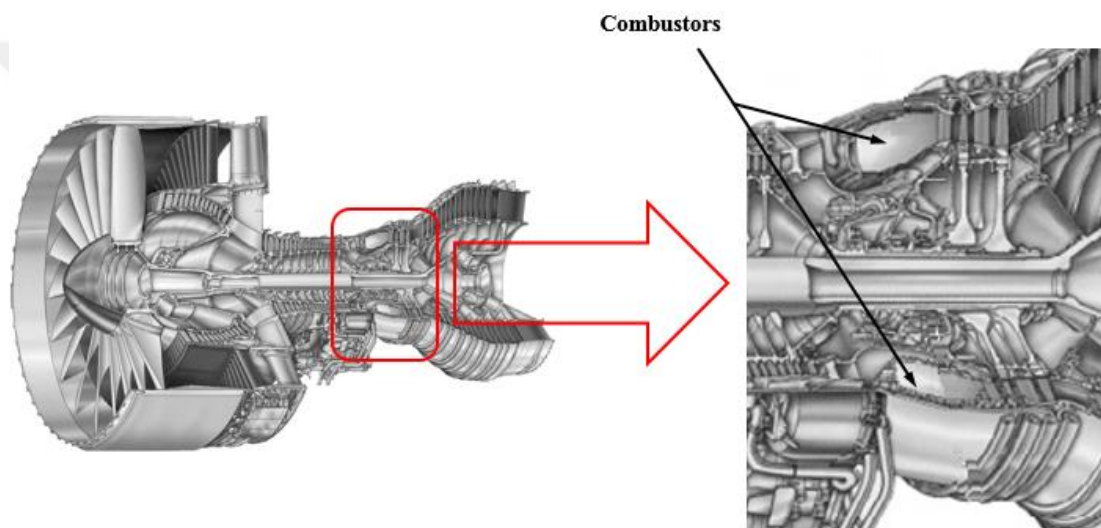


Figure 1.11 : Combustors of combustion chamber in a gas turbine engine [23].

1.3.3 Expansion process

In a gas turbine engine, expansion process is performed by turbine stages. All type of gas turbine engines have a turbine stage which is called power turbine. It is located downstream of the combustion chamber in order to extract energy from the hot and high pressurized gas mixture. Extracted energy provides the power to drive the compressor and the accesories. The expansion process occurs by extracting energy from this hot and high pressure gas mixture released from the combustion chamber and expanding it to a lower temperature and pressure. After that expanded gas is discharged from the nozzle to produce thrust. The process is challenging for the turbine blades. High stresses are involved because of the hot gas stream, the turbine entry temperature (TET) varies between 850°C and 1700°C and its velocity reaches

750 m/s at some locations of the turbine stage for efficient operation [22]. This hot gas temperature is more than the melting temperature of turbine blade material for some engines. Therefore, there are some blade cooling methods and thermal barrier coatings so as to protect the turbine blades from melting.

It should be known that turbine works for nature. Therefore, a turbine needs fewer stages than a compressor to extract the required energy. Besides, turbine blades have more curvature and high tip speed velocities. Turbine stages, each is employed one row of stationary nozzle guide vanes (stator) and one row of moving blades (rotor) (Figure 1.12).

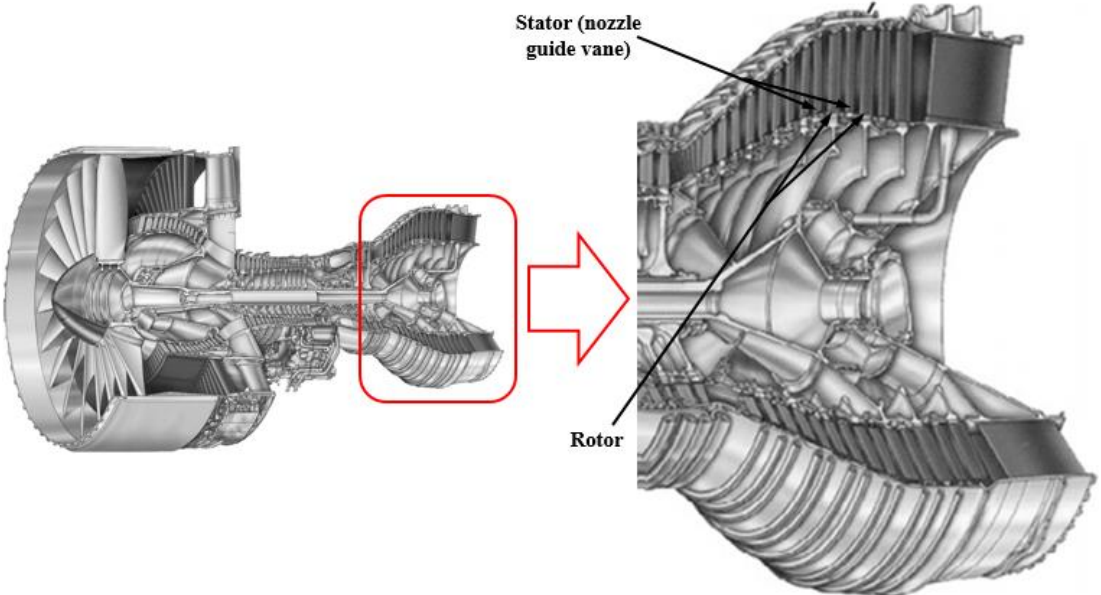


Figure 1.12 : Multistage axial turbine with its components [23].

1.3.4 Exhaust process

Gas discharged from the turbine stage passes the exhaust nozzle and discharges to the atmosphere with a exhaust velocity. Nozzle provides thrust by the help of this discharged gas for the aircraft in the required direction. The velocity and pressure of the exhaust gas produces thrust in turbojet and turbofan engines. However, in a turboprop engine most of the gas energy is absorbed by the turbine to drive the propeller which produces most of the thrust, and only a small amount of thrust is provided by the nozzle. In a turboshaft engine the gas energy is absorbed by two different turbines, one drives compressor sets, the other drives rotorshaft. The expanded useless gas is discharged by the nozzle and does not provide any thrust.

Therefore, the design of the exhaust system has an important effect on the engine performance.

Gases entered to the exhaust nozzle have a temperature between 550° and 850° according to the engine type. This parameter determines the appropriate material for the nozzle construction to avoid distortion and cracking. There are two components giving the nozzle effect to the exhaust section; nozzle shaped jet pipe that surrounds the exhaust cone, and the conical shaped exhaust cone fitting with the air stream to avoid any separation. Air stream cross-sectional area becomes smaller across the exhaust process by these two components and provides required thrust to the engine. A jet engine nozzle system is shown in Figure 1.13.

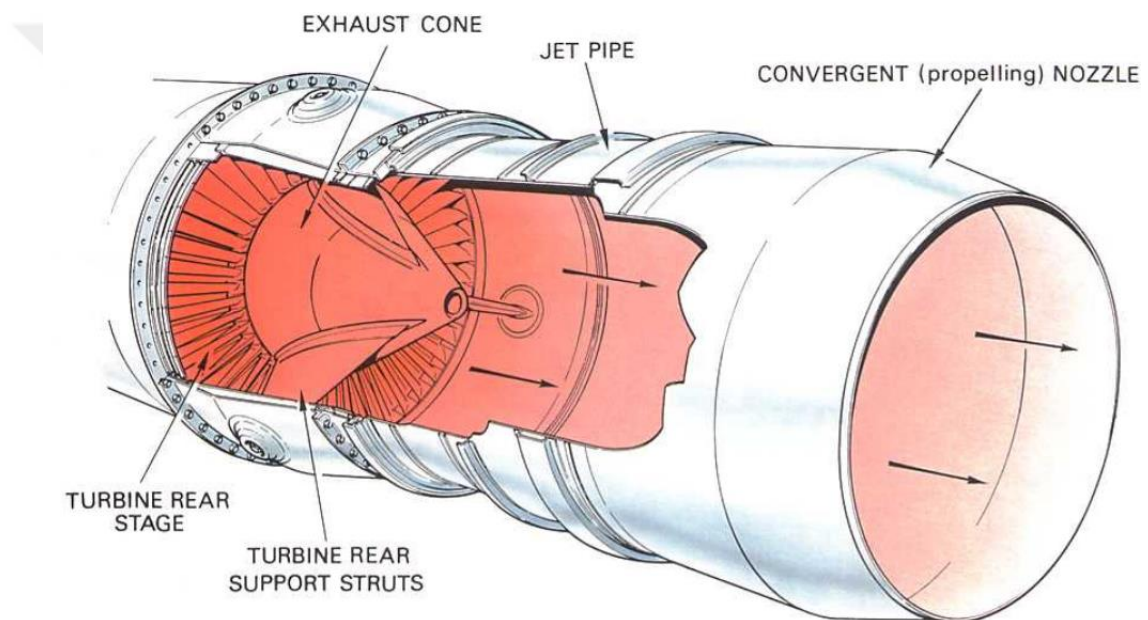


Figure 1.13 : Exhaust nozzle and its components [22].

1.4 Aerodynamics of Turbomachinery in Gas Turbines

Gas turbine engine components like compressors and turbines are turbomachines which have numerous blades. These blades have variant airfoil shapes (Figure 1.14) and produce aerodynamic force as called ‘lift’ as blades rotate. The principle of producing lift by an airfoil is very simple. When airflow encounters the leading edge of an object with positive angle of attack such as a flat plate or an airfoil, it is forced to split upper and lower sides of the object. This sudden change of the airflow produces low pressure zone at the upper surface of the object near leading edge. In response to this, flow over the object accelerates down throughout the upper surface

due to this pressure gradient and flow viscosity. At the same time, the flow lower side of the object is suddenly slowed and even stagnated causing a high pressure zone. The flow at both sides, produces momentum at the bottom side as leaving from the trailing edge of the object and produces lift.

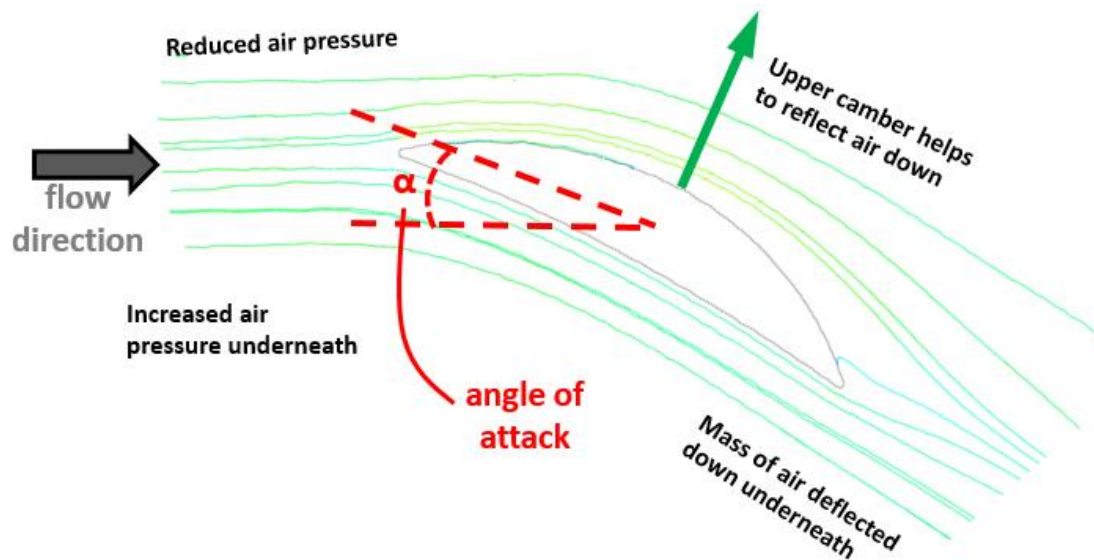


Figure 1.14 : Flow around an airfoil shaped fan blade (from the current study).

Apart from airflow behavior on the airfoil shaped object, during a gas turbine engine operation, pressure and velocity of the airflow are changed depending of the process. As the airflow passes through the engine, its pressure and velocity modifies its demands with respect to aerodynamics and pressure requirements. After the airflow is sucked by the fan or compressor at the inlet section, the compression process occurs. During compression process, the air pressure needs to be increased for combustion process to provide efficient burn. In the combustion chamber, air is heated and its internal energy is increased, and the demand of velocity increase is required for airflow in order to force the turbine blades to rotate. At the exit nozzle, a high velocity stream is necessary to produce thrust for the engine as changing its momentum. These pressure and velocity change in airflow is provided by the ducts inside the engine depending on their type in other words by their shape and size [22].

A demand for velocity or pressure determines the shape of the ducts. When there is a demand for velocity (kinetic energy), the pressure of airflow is converted into kinetic energy by convergent shape nozzle. This operation occurs by narrowing the cross-sectional area and accelerates the airflow. On the contrary, a divergent shape nozzle is used when combustion gases needs to be expanded to provide efficient burn in

combustion chamber. These convergent and divergent shape nozzles are shown in Figure 1.15. It should also be known that these properties of airflow are valid in subsonic conditions. In supersonic conditions, airflow behaves in an opposite way in these ducts. These supersonic ducts which used in supersonic engines (out of this topic) are used in rocket engines or in some jet engines.

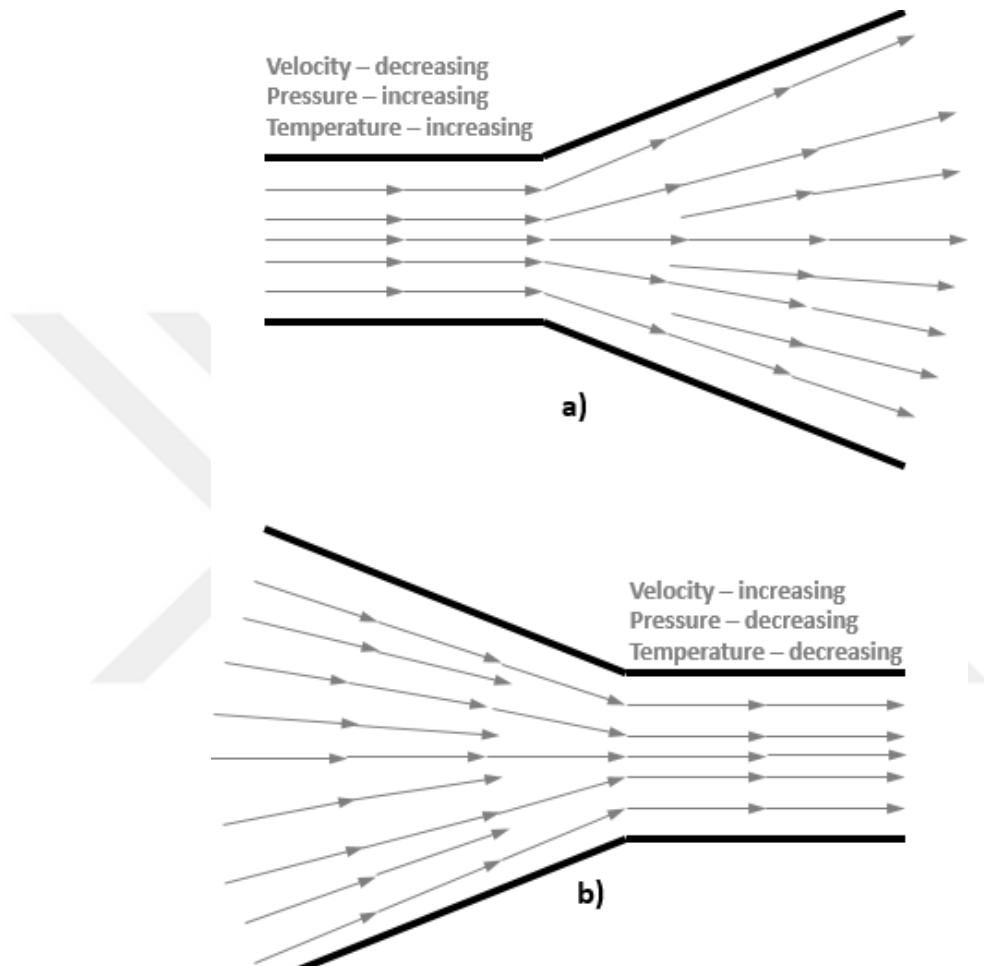


Figure 1.15 : Airflow behaviour through convergent and divergent nozzle.

1.5 Design Principles and Methods of Turbomachinery

Turbomachinery designing mentioned in this section is considered under three main subjects; one-dimensional design as Euler's turbomachinery equation and velocity triangles, two-dimensional design as meridional throughflow design methods, three-dimensional design as commercial CFD (Computational Fluid Dynamics) tools.

One-dimensional design principle of turbomachinery is the basis of the design principle. It is essentially based on Newton's second law; 'The acceleration of a body

is proportional to the net force acting on it and is inversely proportional to its mass' [24]. Newton's second law definition for a body of mass m is;

$$\vec{F} = m\vec{a} = m \frac{d\vec{V}}{dt} = \frac{d(m\vec{V})}{dt} \quad (1.1)$$

where \vec{F} (net force) is acting on the body, \vec{a} is the acceleration under the effect of \vec{F} . The law then leads to the momentum equations (linear and angular momentum equations). A system of a mass 'm' under a net force \vec{F} is expressed by Newton's second law;

$$\sum \vec{F} = m\vec{a} = m \frac{d\vec{V}}{dt} = \frac{d(m\vec{V})}{dt} \quad (1.2)$$

where $m\vec{V}$ term is the linear momentum of the system. On the other hand, turbomachinery components are rotating machines which are analyzed by the moment of linear momentum of the flow stream.

Considering a point O and a force vector \vec{F} assumes point O as the center, then the moment of the force \vec{F} ;

$$\vec{M} = \vec{r} \times \vec{F} \quad (1.3)$$

where \vec{r} is the distance from point O to any point where is on the line of vector \vec{F} . Replacing the vector \vec{F} by the linear momentum vector $m\vec{V}$ gives the moment of momentum (angular momentum);

$$\vec{H} = \vec{r} \times (m\vec{V}) \quad (1.4)$$

In many fluid problems, forces and momentum flows are in the same plane and same axis. Therefore angular momentum equation in a control volume of a steady flow, can be presented in scalar form;

$$\sum M = \sum_{out} r\dot{m}V - \sum_{in} r\dot{m}V \quad (1.5)$$

where \dot{m} is the mass flow rate in a control volume. While considering turbomachinery design, only the tangential component of velocity (Figure 1.16) is

contributed to torque production and consequently to the power production or consumption of the rotor together with the rotational speed. In this case;

$$\tau_{\text{shaft}} = \dot{m} (r_2 V_{\theta 2} - r_1 V_{\theta 1}) \quad (1.6)$$

This equation is known as Euler's turbomachinery equation. $r_2 V_{\theta 2}$ and $r_1 V_{\theta 1}$ are angular momentum terms at the outlet and inlet stations, respectively. Multiplying torque production by shaft speed (ω), power consumption can be obtained.

$$P = \omega \tau_{\text{shaft}} = \omega \dot{m} (r_2 V_{\theta 2} - r_1 V_{\theta 1}) \quad (1.7)$$

Note that, these two are representative equations for power-absorbing turbomachines as ducted-fans, blowers and compressors. However, a propeller can not be classified as turbomachinery because of its unbounded working area. Work supplying turbomachines as turbines, left-hand side of these equations become negative. Therefore, the angular-momentum terms should be reversed for turbines.

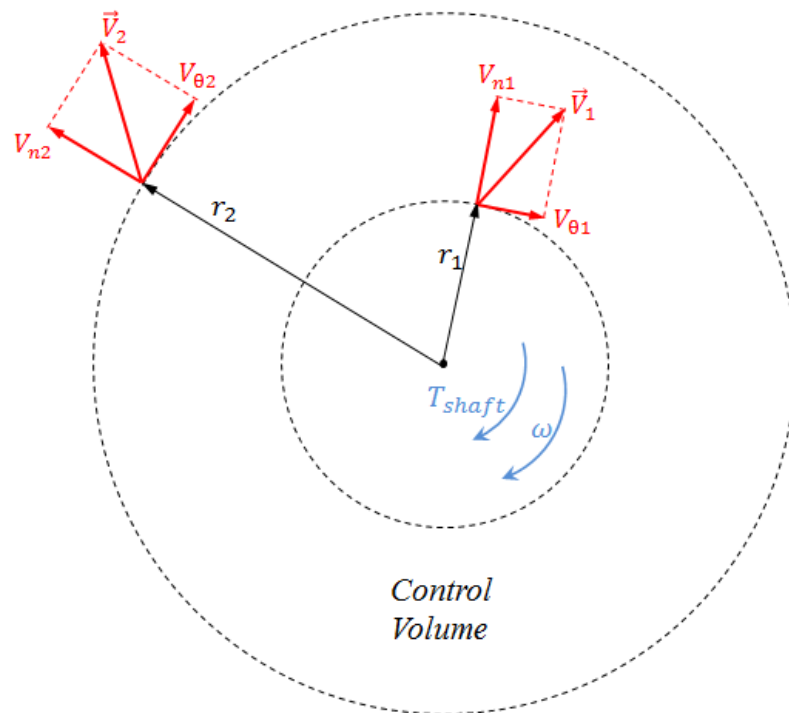


Figure 1.16 : Representative sample of inlet and outlet velocity components on a radial turbomachinery.

Euler’s turbomachinery equation determines the energy transfer between fluid and turbomachinery rotor. This equation and its derivatives are fundamentals for turbomachinery design by providing power, efficiency and other factors.

In the preceding section, basic components of velocity is simply mentioned on a radial turbomachinery. However, they should be properly analyzed by stationary and rotating observers. In this case, U is called the blade rotational velocity and with respect to this term, absolute velocity (V) which is observed by a stationary observer and relative velocity (W) which is observed by a rotating observer are obtained and these three components are together velocity-triangle contributors. Figure 1.17.a) shows the three-dimensional view of axial fan which is the focus of the current thesis, combined with the meridional view of it and 17.b) shows blade-to-blade view of the fan with inlet and outlet velocity triangles. Briefly;

$$V = W + U \tag{1.8}$$

gives the relationship between stationary and rotating frames of reference. The velocity difference between these two observers is the vector U .

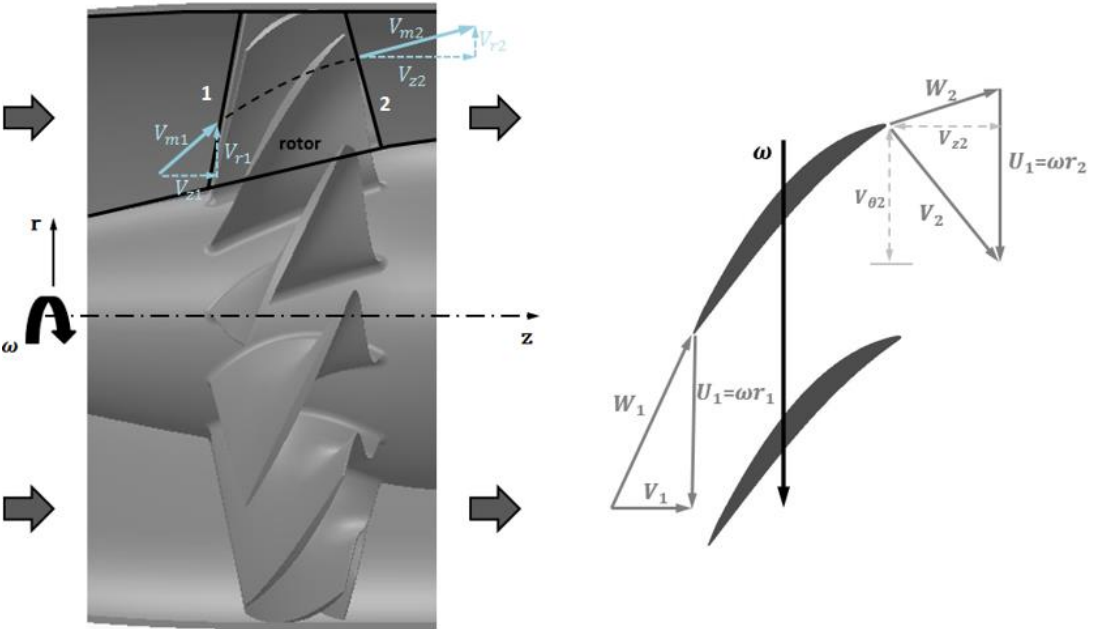


Figure 1.17 : a) Combination of 3D & meridional view, b) Blade-to-blade view.

In situations where to find torque and power variables, absolute velocity (V) should be used. In real effects such as choking and friction, relative velocity (W) should be in consideration [25].

Apart from one-dimensional design concept there is two-dimensional throughflow design that uses streamline curvature method. Two-dimensional design method is the extended and advanced configuration of one-dimensional design method that uses Euler's turbomachinery equation and its derivatives. One-dimensional method also called meanline method considers only the average flow properties on mean streamline of the turbomachinery. However, from blade root (hub) to blade tip (shroud) in other words in spanwise direction, blade tangential velocity (U) changes considerably. In this direction, two-dimensional throughflow design approach that both considers spanwise and streamwise changes in flowfield is an important tool for turbomachinery design process.

The two-dimensional throughflow method usually referred as quasi-3D (quasi three-dimensional) based on pioneering work of Wu [26], has a key role from one-dimensional to three-dimensional design for turbomachinery. It considers blade effects in axisymmetric swirling flow by employing Euler's turbomachinery equation, pressure loss, blockage and turning effects. It both covers the simplicity of one-dimensional design and high accuracy of three-dimensional design. It is important from the aspect of providing fast and reliable simulation solutions in order to give an insight for three-dimensional design and saves calculation time.

Three-dimensional design of turbomachinery is the most advanced technique, yet it is still time-consuming in contrast with the preliminary methods. It is only applied at the final stage of the design phase for fine-tuning before prototype and production processes. Therefore, it considerably reduces the costs of these processes. It is a numerical approach and uses Navier-Stokes equations which cover motion of fluids (Newton's second law). Application of a numerical design tool which is called Computational Fluid Dynamics (CFD) reflects the real performance of turbomachinery by a higher fidelity. However, numerical CFD tools which use Reynolds-Averaged Navier Stokes (RANS) equations are required to be validated with the experimental data of representative flow. Since this method can model a three-dimensional turbulent flow that requires time-dependent (transient) solution and very fine mesh structure, with a coarse mesh structure as a steady state condition.

This part of the thesis provided a brief summary of turbomachinery design principles from one-dimensional mean line method to three-dimensional advanced numerical method. Next part will express the aim and motivation of this thesis.

1.6 Goal and Scope Definition

1.6.1 Motivation

Most of the gas turbine classes have been shown great advancements with respect to performance and efficiency in recent years, and it is seem that there is only one class have been left – micro-scaled gas turbines (under 2 kN of thrust). In the market, searching of micro gas turbine engines compatible with Unmanned Aerial Vehicles (UAVs), reciprocating or turbojet engines are generally preferred and there is a lack of advanced micro turbofans. However, recent studies [21; 27] suggested an innovative and advanced turbofan architecture which is feasible and applicable for small scales. An existing concept of a single shaft micro turbojet engine conversion into micro turbofan was examined thermodynamically. The concept also included a continuously variable transmission (CVT) with a variable bypass nozzle in order to provide more efficient and versatile design. It was simplified by removing low pressure turbine (LPT) and booster with a minor change in the core compressor. Therefore, existing high pressure turbine (HPT) drives both the low pressure compressor (LPC) which is the focus of this thesis and the core compressor. The basic illustration of the concept is shown in Figure 1.18.

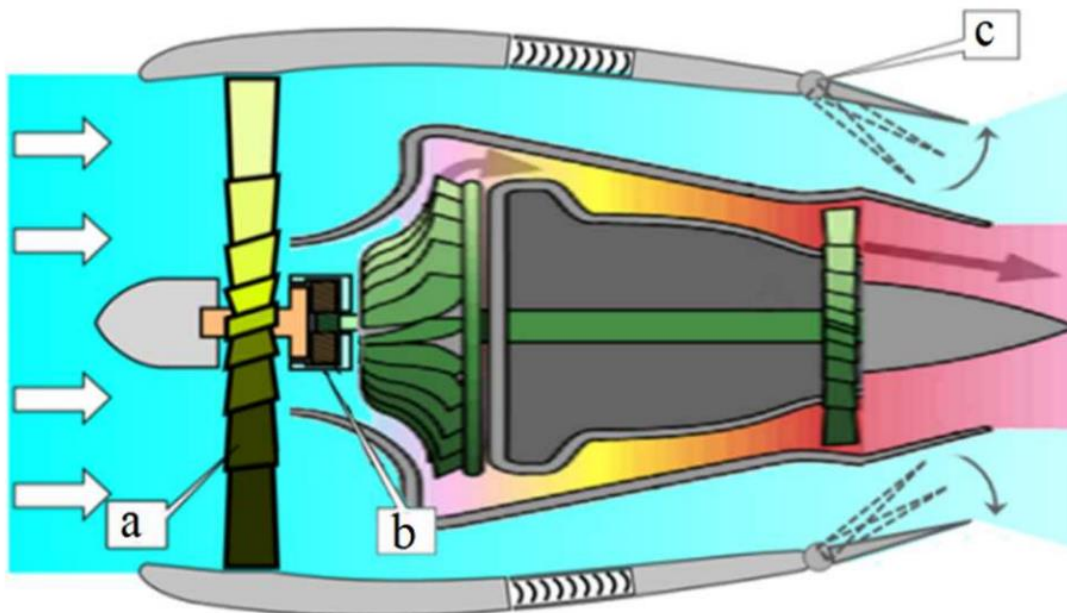


Figure 1.18 : Basic representation of the concept; a) Fan , b) CVT , c) variable bypass nozzle [21].

1.6.2 Scope of the current thesis

As mentioned above, LPC system will be unified as a single stage axial compressor (denoted as ‘fan’). Such an innovative design which will be the first time in the open literature is expected to be a guideline for micro turbofan concepts for especially future UAV engines. The unified concept schematic comparison with typical LPC system is shown in Figure 1.19.

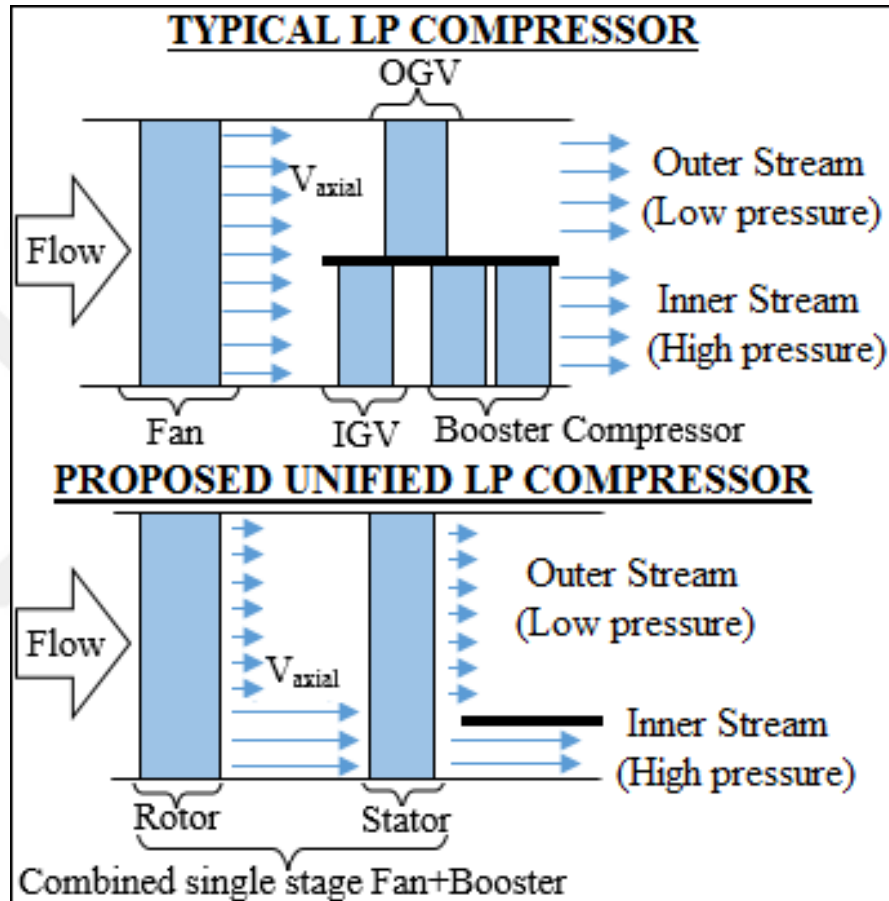


Figure 1.19: Typical and proposed LPC systems comparison for similar bypass ratio [28].

For such a unified design, a requirement of more power by the fan from HPT will increase the inlet pressure of core compressor, resulting not only higher thermodynamic cycle efficiencies also making possible of additional power extraction from the turbine. Unified fan without any booster should be additionally loaded at the hub and relaxed at the rest. Increasing work potential from hub to tip because of centrifugal effect, this fan is radically unconventional hub-loaded, tip relaxed, highly twisted design resulting reduced even reversed rotor chamber at the tip and makes itself different from the conventional highly-loaded concepts [29; 30].

Maximum limits of core and bypass pressure ratio difference is examined in order to obtain maximum thermodynamic cycle. Drawback of such a fan rotor design makes the hub transonic and highly-loaded. Transonic flow at the hub considerably reduces core duct inlet area to avoid entropy rise by flow separation and increases core duct diffusion demands.

On-design requirements were determined from the thermodynamic cycle of a representative microjet by axisymmetric through-flow modeling [31]. In on-design stage, comparison of two alternative concepts with and without IGV were presented. More promising concept was studied by experimentally validated CFD solver to determine the potential of the concept. After that, stator optimization by applying three-dimensional aerodynamic configurations (lean - sweep) was further examined.

Scope of the current thesis, off-design study of the low-pressure compressor system was investigated after on-design process and design point determination. The performance maps were created for each core and bypass streams individually. Results were obtained both for stage only (rotor + stator) configuration and whole LPC system (rotor + stator + exit ducts). Operational range of the system was therefore determined and investigated detailly by the help of velocity and pressure illustrations. Some suggestions were made about aerodynamic design of this novel fan blade for further improvements.

Moreover, thermodynamic matching study was carried out for the engine. At first, an AMT Nike Compressor that will be used as a core compressor for this engine, off-design performance map was created. Turbine off-design performance maps were provided from collaborative team at Purdue University. Thermodynamic matching study was then performed in two steps (one for core turbojet, one for whole turbofan);

- Core compressor – turbine matching
- Core compressor+fan – turbine matching

Core turbojet and adaptive turbofan matching results were compared with respect to SFC, operation performance, efficiency etc. Some suggestions and comments were made to represent the improvements of this novel concept over the existing one.

Finally, aeromechanical study of the fan blade was performed. In this direction, natural frequencies of the fan rotor blade were obtained. Crossing mode shapes were

determined from the Campbell Diagram. Each mode was investigated in deformed mesh blade flutter CFD analysis to obtain aerodynamic damping. In parallel, unsteady rotor-stator interaction CFD analysis was performed to obtain unsteady pressure distribution based on stator excitation. Both aerodynamic damping and unsteady pressure distribution were used for Harmonic Response Analysis to determine the maximum alternating stress. This stress directly determines the life cycle of the fan blade. Therefore, structural integrity study of the fan blade was accomplished.



2. HIGH FIDELITY AERODYNAMIC SIMULATION (CFD) METHODOLOGY

2.1 The Solver Theory and Utilized Software

ANSYS Turbogrid 18.2 which is a special meshing tool for turbomachinery was used to create the computational grid. ANSYS CFX 18.2 numerical solver was used to analyze the flow domain.

Ideal gas equation is related to density with its absolute values of pressure and temperature;

$$\rho = \frac{P}{R_{\text{air}} T} \quad [\text{kg/m}_3] \quad (2.1)$$

Navier-Stokes Equation considers three-dimensional flow field turbulence in respect to all time and length and it requires very high computational capacity. Time dependent velocity terms of any direction are separated from original Navier-Stokes Equation and then integrated as average velocities to Reynolds-Averaged Navier Stokes (RANS) Equation. Time-averaged Compressible Newtonian Flow RANS Equation [32] is;

$$\frac{\partial \rho V_i}{\partial t} + \frac{\partial}{\partial x_j} (\rho V_i V_j) = -\frac{\partial P}{\partial x_i} + \frac{\partial}{\partial x_j} \left[\mu \left(\frac{\partial V_i}{\partial x_j} + \frac{\partial V_j}{\partial x_i} \right) - \overline{\rho v_i v_j} \right] \quad (2.2)$$

The term $\overline{\rho v_i v_j}$ expresses Reynolds stresses and calculates mixing because of turbulent fluctuations. Mass continuity equation can be rewritten as;

$$\frac{\partial \rho}{\partial t} + \frac{\partial}{\partial x_j} (\rho V_j) = 0 \quad (2.3)$$

As a result, energy equation is;

$$\frac{\partial \rho H}{\partial t} - \frac{\partial P}{\partial t} + \frac{\partial}{\partial x_j} (\rho V_j H) = \frac{\partial}{\partial x_j} \left(k \frac{\partial T}{\partial x_j} - \overline{\rho u_j h} \right) + \frac{\partial}{\partial x_j} \left\{ V_i \left[\mu \left(\frac{\partial V_i}{\partial x_j} + \frac{\partial V_j}{\partial x_i} \right) - \overline{\rho v_i v_j} \right] \right\} \quad (2.4)$$

Total enthalpy term (H) includes turbulent kinetic energy contribution in this equation. $\overline{\rho u_j h}$ term calculates additional flux because of the turbulence while the term including Reynolds stresses estimates viscous dissipation through both mean and fluctuating velocity components [32].

Effective viscosity approach so-called Boussinesq approach for turbulent terms was utilized to model Reynolds stresses. Instead molecular viscosity, molecular+turbulent viscosity field was used so as to estimate turbulent fluctuation effects for an isotropic manner. Therefore;

$$-\overline{\rho v_i v_j} = \mu_{\text{turbulent}} \left(\frac{\partial V_i}{\partial x_j} + \frac{\partial V_j}{\partial x_i} \right) \quad (2.5)$$

Following similar calculations, turbulent conductivity ($\mu_{\text{turbulent}}/Pr_{\text{turbulent}}$) was expressed as follows;

$$-\overline{\rho u_j h} = \frac{\mu_{\text{turbulent}}}{Pr_{\text{turbulent}}} \frac{\partial h}{\partial x_j} \quad (2.6)$$

where $Pr_{\text{turbulent}}$ is the Prandtl number depending upon turbulent viscosity. Consequently, the problem was simplified by resulting $\mu_{\text{turbulent}}$ as a function of space.

For the CFD calculations Shear Stress Transport (SST) turbulence model [32] was chosen in order to model turbulent viscosity domain, as it provides robust and reliable results with adverse pressure gradients in the flow domain [33]. Turbulent viscosity both depends on specific dissipation (ω) and turbulent kinetic energy (k), within a low Reynolds number limiter as;

$$\mu_{\text{turbulent}} = \frac{\rho k}{\omega} \frac{1}{\max \left[\frac{1 + \rho k / 6 \mu \omega}{0.024 + \rho k / 6 \mu \omega}, \left(\frac{\partial V_i}{\partial x_j} + \frac{\partial V_j}{\partial x_i} \right) \frac{F_2}{0.62 \omega} \right]} \quad (2.7)$$

Following equations are expressed governing equations used for k and ω , respectively [32]. For the turbulent kinetic energy (k);

$$\frac{\partial(\rho k)}{\partial t} + \frac{\partial}{\partial x_j}(\rho V_j k) = \frac{\partial}{\partial x_j} \left[\left(\mu + \frac{\mu_{\text{turbulent}}}{0.176F_1 + 1} \right) \frac{\partial k}{\partial x_j} \right] + P_k - 0.09\rho k\omega \quad (2.8)$$

And for the specific dissipation (ω);

$$\begin{aligned} \frac{\partial \rho \omega}{\partial t} + \frac{\partial(\rho V_j \omega)}{\partial x_j} = \frac{\partial}{\partial x_j} \left[\left(\mu + \frac{\mu_{\text{turbulent}}}{0.8317757F_1 + 1.168224299} \right) \frac{\partial \omega}{\partial x_j} \right] \\ + (1-F_1) \frac{1.712\rho}{\omega} \frac{\partial k}{\partial x_j} \frac{\partial \omega}{\partial x_j} + \left(\frac{5}{9}F_1 + 0.44(1-F_1) \right) \frac{\omega}{k} P_k + (0.0828 - 0.0078F_1)\rho\omega^2 \end{aligned} \quad (2.9)$$

In the second equation P_k term is the production of turbulence because of viscous forces and expressed as;

$$P_k = \mu_{\text{turbulent}} \left(\frac{\partial V_i}{\partial x_j} + \frac{\partial V_j}{\partial x_i} \right) \frac{\partial V_i}{\partial x_j} - \frac{2}{3} \frac{\partial V_k}{\partial x_k} \left(3\mu_{\text{turbulent}} \frac{\partial V_k}{\partial x_k} + \rho k \right) \quad (2.10)$$

SST submodels were also considered, which were transition from laminar to turbulent (intermittency and cross-flow) and reattachment modification for flow reattachments. F_1 and F_2 from above equations are blending factors. Their values are '1' near the wall surfaces ($y=0$ m), and it decreases to '0' as moving away from the wall surface ($y \gg 0$ m). The definition of F_1 is;

$$F_1 = \tanh(\arg_1^4) \quad (2.11)$$

where \arg_1 term in the paranthesis is defined as follows;

$$\arg_1 = \min \left(\max \left(\frac{\sqrt{k}}{0.09\omega y}, \frac{500\mu}{\rho\omega^2 y^2} \right), \frac{3.424\rho k}{\max \left(\frac{1.712\rho}{\omega} \frac{\partial k}{\partial x_j} \frac{\partial \omega}{\partial x_j}, 10^{-10} \right) y^2} \right) \quad (2.12)$$

and the definition of F_2 is;

$$F_2 = \tanh(\arg_2^2) \quad (2.13)$$

where \arg_2 term in the paranthesis is defined as follows;

$$\arg_2 = \max\left(\frac{2\sqrt{k}}{0.09\omega y}, \frac{500\mu}{\rho\omega y^2}\right) \quad (2.14)$$

For numerical solution, finite volume method that is vertex-centered was applied to governing equations. ‘High-Resolution Scheme’ [32] (upwind scheme with the second order accuracy) of CFX for the advection terms interpolation was applied.

‘Sutherland’s law’ was used in order to model dynamic viscosity of air flow for absolute temperature function ($0 < T < 555$ K);

$$\mu = 1.716/10^5 \left(\frac{T}{273.15}\right)^{3/2} \frac{383.55}{T+110.4} \left[\frac{\text{kg}}{\text{ms}}\right] \quad (2.15)$$

For heat capacity of air at constant pressure (c_p), pressure dependency was neglected, instead polynomial equation was used (100-1000 K);

$$c_p = (1161.482) - (2.368819)T + (0.01485511)T^2 - (5.034909/10^5)T^3 + (9.928569/10^8)T^4 - (1.111097/10^{10})T^5 + (6.540196/10^{14})T^6 - (1.573588/10^{17})T^7 \quad [\text{J/kgK}] \quad (2.16)$$

Heat capacity of air at constant volume (c_v) definition is as follows;

$$c_v(T) = c_p(T) - R_{\text{air}} \quad (2.17)$$

The entalpy change formula;

$$h - h_{\text{ref}} = \int_{T_{\text{ref}}}^T c_p(T) dT \quad (2.18)$$

Internal energy (e) equation;

$$e - e_{\text{ref}} = \int_{T_{\text{ref}}}^T c_v(T) dT \quad (2.19)$$

Finally, entropy change expression is as follows;

$$s-s_{ref} = \int_{T_{ref}}^T \frac{c_p(T)}{T} dT - R_{air} \ln\left(\frac{P}{P_{ref}}\right) \quad (2.20)$$

2.2 Experimental Validation of the Solver

Validation study of the solver was performed with a representative NASA Rotor 37 transonic compressor. The experimental data of the component was taken from Suder's study [34]. The computational domain density was specified by coarse, medium, fine and finest mesh densities. Near-wall cell y^+ values were kept less than 5, and maximum growth rate of elements were kept less than 1.3. Inlet boundary condition was applied as total values of measured spanwise distribution of P_t and T_t . P_s with radial equilibrium method was used for outlet to match the proper mass flow values radially. Table 2.1 represents some main parameter of the mesh structures at design point of Rotor 37 (17188.7 rpm and 20.31 kg/s mass flow).

Table 2.1 : Four different grid levels of NASA Rotor 37.

	Number of Volumes			Π	$\eta_{isentropic}$
	Total	Spanwise	Tip gap		
Coarse	$0.85 \cdot 10^6$	40	20	2.05	0.85
Medium	$3.40 \cdot 10^6$	100	35	2.08	0.86
Fine	$8.50 \cdot 10^6$	160	50	2.08	0.86
Finest	$14.40 \cdot 10^6$	100	60	2.08	0.86

As a turbulence model, SST (Shear Stress Transport) which is well-known to capture excessive streamwise pressure gradients in turbomachinery [35], was chosen. Preliminary analyses of SST (Shear Stress Transport) turbulence model was applied without any submodel. However, it showed large discrepancy comparing to experimental data in the results of radial distributed pressure and temperature ratio. Therefore, submodels of SST turbulence model were studied to obtain the closest result to experimental data of Rotor 37. Transition models of intermittency and crossflow and also reattachment modification submodel which captures separated flows reattachment to the boundary wall, showed an improvement of the results for validation (tuned SST - Figure 2.1). Moreover, k-epsilon and further Reynolds Stress Models (RSM) are applied as well, but none of these obtained results as close as SST turbulence model.

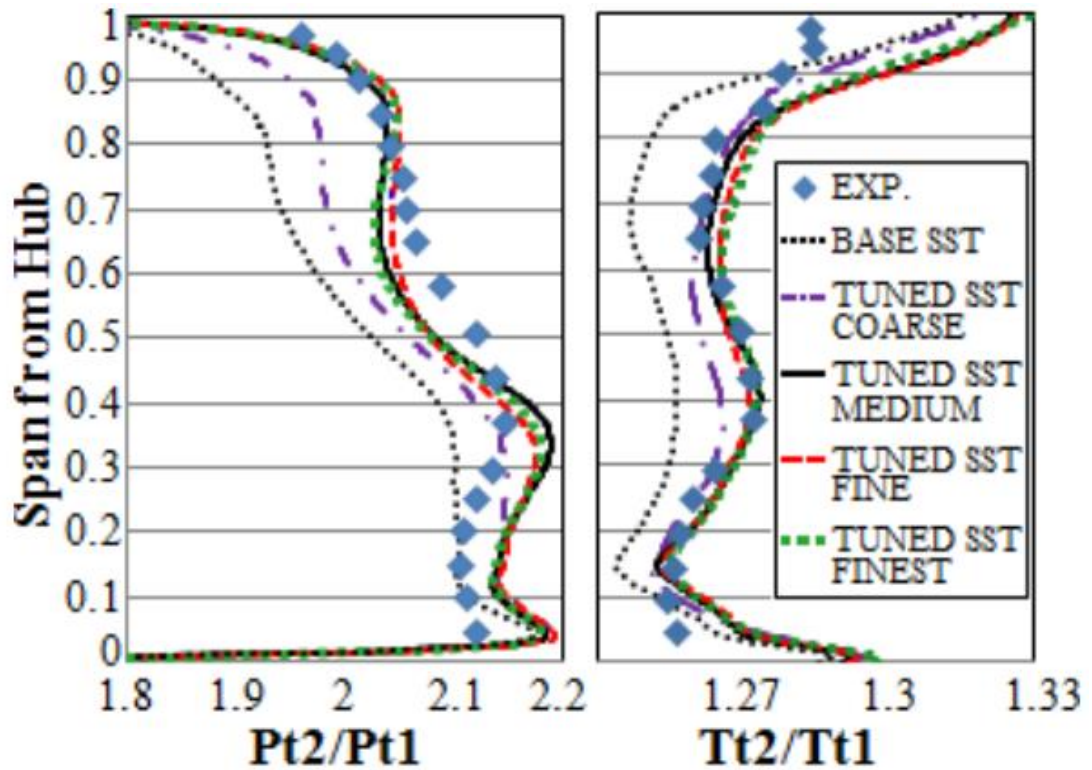


Figure 2.1 : Spanwise measured and calculated results of Rotor 37 [34].

Back in Table 2.1, medium, fine and finest levels of grid densities are shown in good agreement with the experimental data. Therefore, medium mesh is sufficient in order to obtain accurate simulation results in point of reducing calculation costs. The discrepancy level through spanwise direction is in acceptable range based on CFD code assessment study [36].

Moreover, off-design performance of NASA Rotor 37 was obtained and compared to experimental results. Design (100%) and partial speeds (60% 80%) were applied for total pressure ratio and isentropic efficiency of the rotor. The performance results presented in Figure 2.2 also shows good agreement for all speedlines. For the efficiency, there is some discrepancy. The reason is not clear, however in the experiments, temperature measurement locations and the averaging technique may be the reason. Besides, geometrical differences and the utilized turbulence model may also be responsible for this discrepancy.

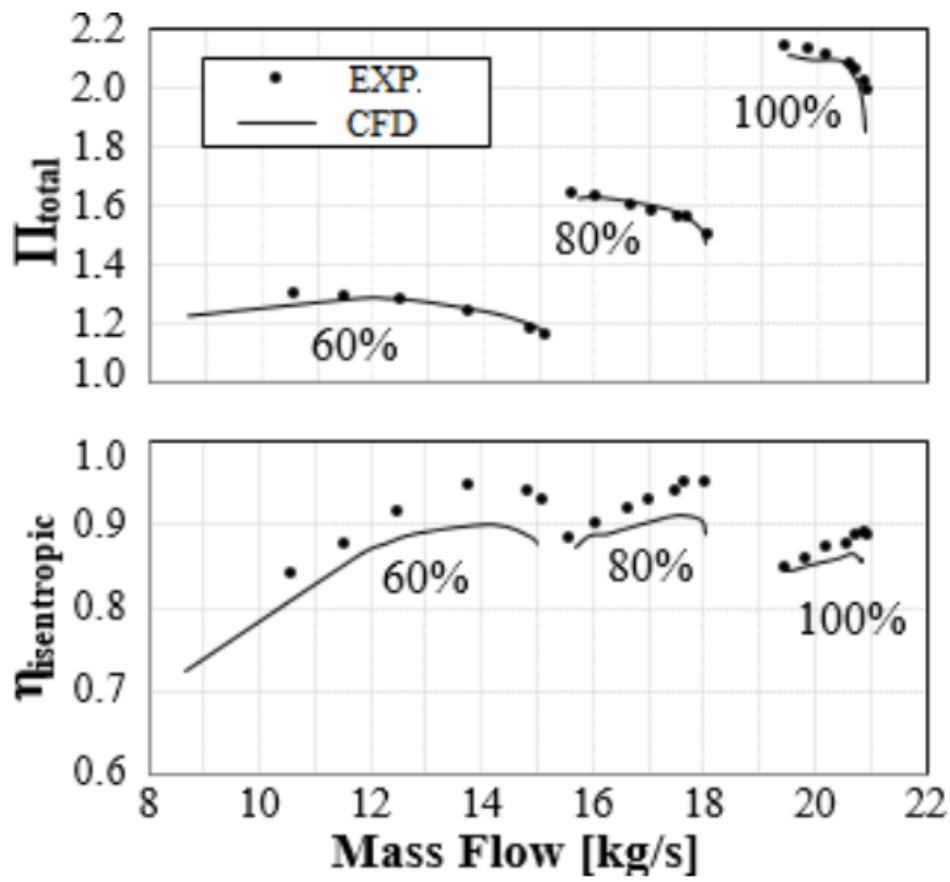


Figure 2.2 : Measured and calculated performance maps.

3. DETAILED AERODYNAMIC OFF-DESIGN STUDY

The design of the fan was done by my colleagues and professor. However, in this section, the design of the LPC system (fan) will be briefly explained in subtitle 3.1. The design cycle requirements and the cases with and without IGV will be discussed. Then, the stator optimization study will be presented. After that, in subtitle 3.2 which is one of the main focuses of this thesis, the off-design performance and aerodynamics of the fan will be detailly investigated in every respect by considering the mixing losses, passage and tip leakage characteristics of the flow and some suggestions will be proposed.

3.1 Design of the Fan

Preliminary aerodynamic design requirements were performed by a thermodynamics cycle that applies the similar method of pre-cited study [21] which used both a micro turbojet engine and a scaled-down fan (NASA High Speed Quite Fan) performance maps [37]. Maximum rotational speed of the fan at take-off condition was determined as design point while thrust was 1.7 kN. Prior throughflow calculations were performed considering radial equilibrium theory and Table 3.1 shows core and bypass performance requirements for such a challenging fan design.

Table 3.1 : Preliminary design cycle requirements [28].

	\dot{m} [kg/s]	$\dot{m}_{\text{bypass}}/\dot{m}_{\text{core}}$	Π	$\eta_{\text{isentropic}}$
Core Section	1.25	-	1.6	0.80
Bypass Section	5.48	-	1.4	0.82
Total	6.73	4.38	-	-

Depending on cycle requirements, core pressure ratio (1.6) should be higher than the bypass pressure ratio (1.4) and therefore created significant axial velocity difference between hub and tip. Tip performance deterioration and reduced inlet high of core duct where most of air stream passes near hub, were the results of significant pressure ratio difference. Target efficiencies were predicted 80% for core and 82% for bypass considering long ducts and low Re (Reynolds) numbers.

Preliminary aerodynamic design was done by an axisymmetric throughflow design tool [31]. The distinctive feature of this tool is that it considers coupled modeling of core and bypass ducts which are separated by a flow-splitter, taking into account of compression stage as well.

Using the axisymmetric throughflow design tool, the first concept and its environment were created. Single stage LPC without IGV are presented in Figure 3.1.

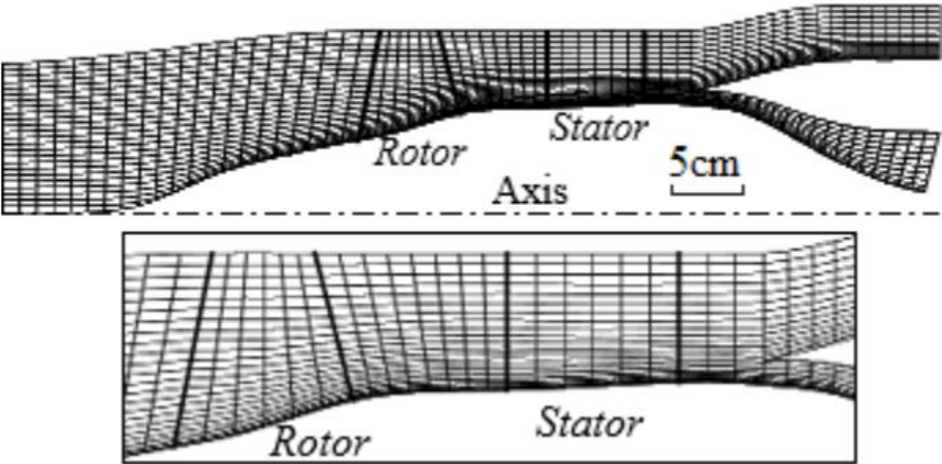


Figure 3.1 : Computational domain of designed LPC [28].

Resulting pressure ratio distribution from hub to tip and meridional contour are shown in Figure 3.2.

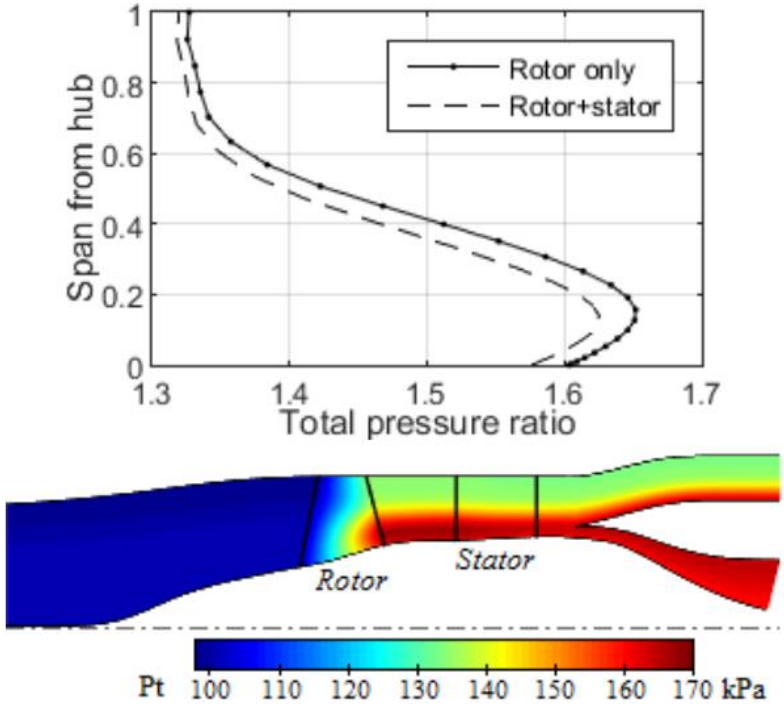


Figure 3.2 : Spanwise total pressure distribution (above), meridional pressure distribution (below) [28].

At the beginning, rotor and stator chord length in axial direction were determined to meet the demand from manufacturing perspective and to avoid high Re numbers' viscous effects. Corresponding axial chord lengths were designed as 4, 7 and 6.7 cm, (Figure 3.1) for rotor tip, rotor hub and stator, respectively, while tip radius was 12.5 cm. Blade thickness was determined 16% of relative thickness (maximum thickness/chord) at hub to overcome high velocity values and 4% of relative thickness at tip to be adapted for supersonic airstream. Resulting maximum thickness values by respect to the longer axial chord lengths varied from 12 at hub to minimum of 4 mm at tip for rotor and was constant for stator (4 mm). Minimum thickness values belonged to leading edge (LE) and trailing edge (TE) by 2% of the chord length for each blade.

Next, main dimension of the flow path was examined by throughflow design tool. As mentioned above, rotational speed of the fan rotor, determined by maximum at takeoff condition was 29000 rpm. The resulted diameter of fan shroud was 25 cm which is a suitable value of a 20 cm-diameter bypass duct design for a micro-scaled core engine. Mach number exceeded 1.2 and demanded reversed cambered design as a result of such a high diameter at shroud. This negatively effected structural concerns and efficiency of tip depending upon both lower tip pressure ratio of 1.4 and work coefficient of $\psi_{tip} < 0.2$. However, higher shroud diameter avoided higher inlet axial Ma values (~ 0.6). Considering the shroud diameter, inlet hub diameter was calculated as 10 cm. The main considerations were to keep enough pitch distance between rotor and stator while keeping hub diameter smaller enough, making inlet Ma lesser (~ 0.5) as well. Bigger hub diameter would result rotor aspect ratio to below unity which increases stronger secondary flows and higher Ma values to create blockage at the hub region. Hub diameter was increased from LE (10 cm) to TE (13 cm) to prevent excessive load at rotor hub region and to reduce stator hub turning. Resulting work coefficient at hub was $\psi_{hub} < 1.34$ (Figure 3.3). Hub increase was applied by endwall contouring method [38] (more adaptive to secondary flows) instead a planar increase. Endwall of hub and tip LE was also considered to adapt its design for upstream flow. In this direction, endwall of hub LE was designed as a concave shape in order to reduce Ma value and expand choke limit. Besides, tip LE was shaped as convex to accelerate air stream more and relax the blade at tip by reduction of loading. Equation 3.1 and 3.2 defines work and flow coefficients. Work

coefficient distribution from hub to tip for such a highly loaded fan was applied by considering Dickens and Day study [39]. The flow coefficient is as follows;

$$\Phi = \frac{V_{axial}}{\omega r} \quad (3.1)$$

and the work coefficient is;

$$\psi = \frac{\Delta H}{(\omega r)^2} \quad (3.2)$$

Determined work and flow coefficients spanwise distribution is shown in Figure 3.3. Stator diameters are the same as rotor exit diameters. Resulting core duct channel inlet was designed relatively narrow (see Figure 3.1) so as to provide desired bypass ratio. A higher hub design diameter for stator would create further narrower inlet channel and extremely increased diffuser channel before core compressor. Conversely, lower hub diameter would further increase stator loading at hub region, exceeding the limit of De-haller number (<0.72).

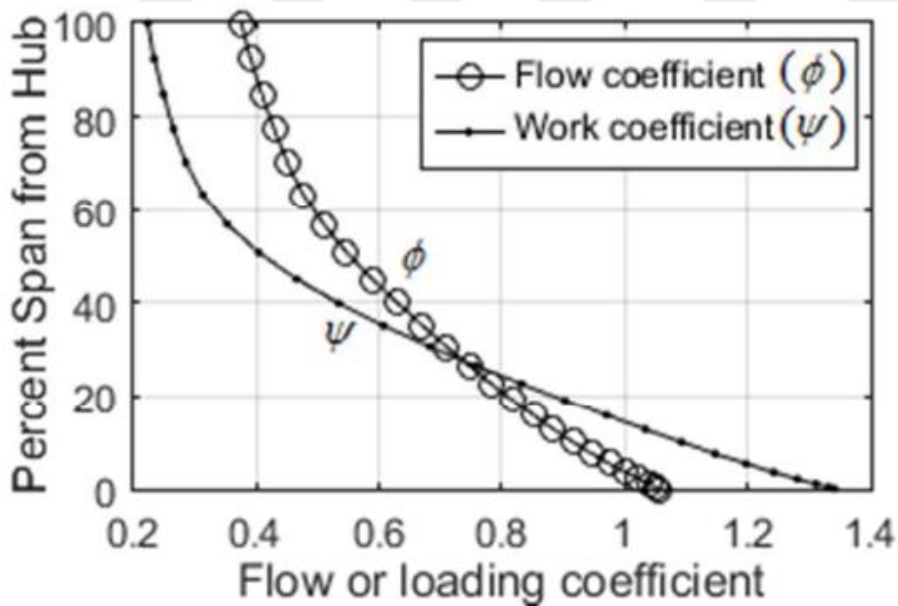


Figure 3.3 : Work and flow coefficient [28].

Meridional Mach number distribution is shown in Figure 3.4. It is in compliance with spanwise pressure distribution shown in Figure 3.2.

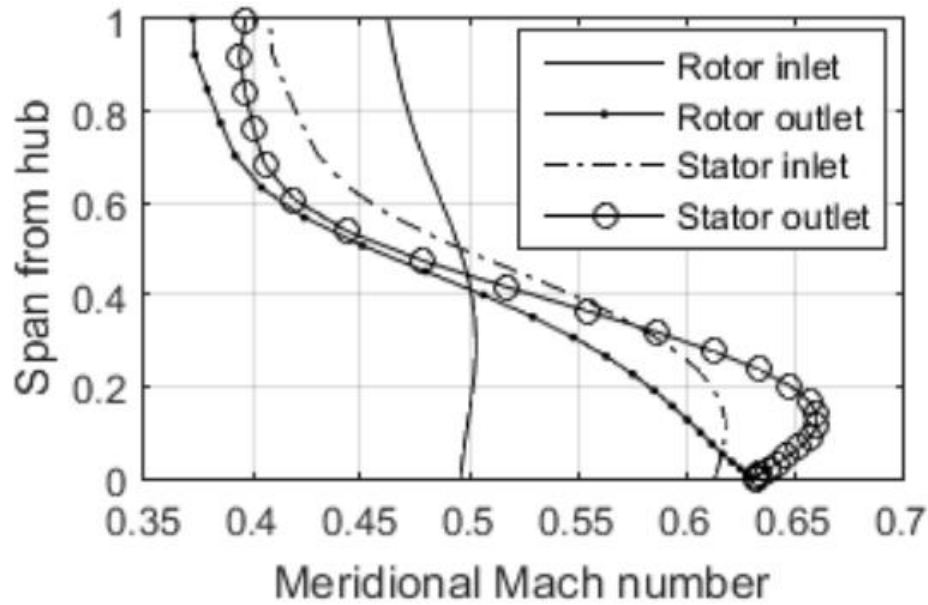


Figure 3.4 : Meridional Mach number distribution [28].

Mach values seen in Figure 3.4 would result acoustic concerns between rotor and stator interaction. To prevent this issue stator was located one-chord far from rotor. Furthermore, stator is at upstream of the splitter after rotor to provide simplicity.

Based on main dimensions and parameters of LPC, calculated relative Mach number at rotor tip was around 1.2 (380 m/s) which is appropriate for bypass pressure ratio and 1.45 (460 m/s) at overload operation of 35000 rpm. While rotor hub Mach was around 0.65, stator Mach was 0.85 making hub section transonic and tip section was around 0.5.

The flow angle results and estimated metal angle values were determined based on the incidence and deviation correlations [31]. Throughflow code determined the choke by predicting higher incidences to make the rotor blades more opened to incoming flow. By a given flow angle, the throat area was increased. Yet, choke which is a 3D phenomenon can not be determined by 2D throughflow code. Considering also shock and friction losses in order to predict total pressure of throat, it is obviously more appropriate to apply 3D numerical methods. In this direction, predicted incidence values were considered lower by multiplying them 1/3 (Figure 3.5). As a result, design point was reached near-choke from near-stall (increased stall margin in return for minor efficiency lost) in the performance maps.

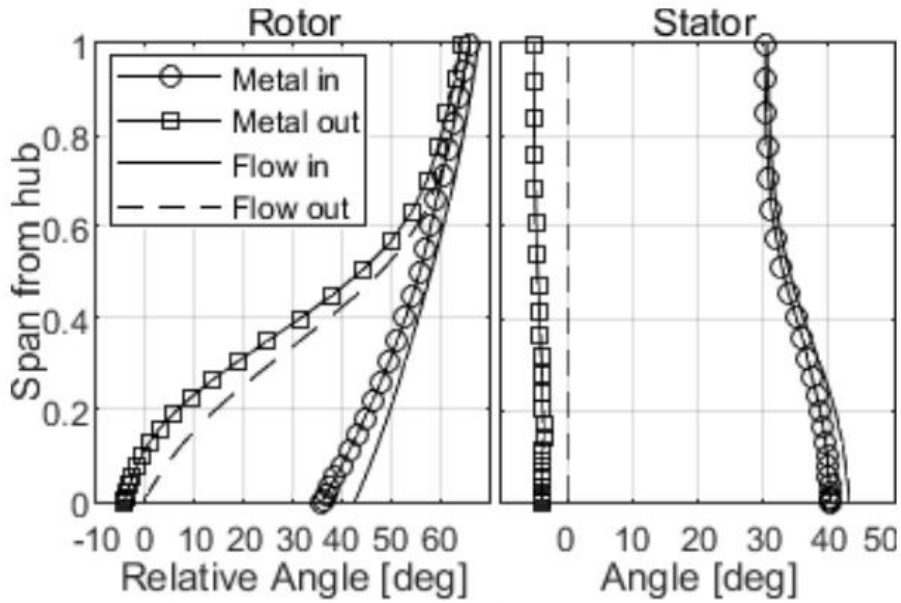


Figure 3.5 : Flow and metal angles [28].

Number of rotor (11 blades) and stator (20 blades) blades were determined by deviation values (metal exit angle). Solidity and chord length spanwise distribution was presented in Figure 3.6. Chord values were kept as thicker as possible for structural and manufacturing concerns with a negligible change in rotor aspect ratio. Blade cross-section was preferred as mid-loaded Double Circular Arc (DCA) which is more suitable for such a transonic blade based on metal angles, thickness values and radial location of the section.

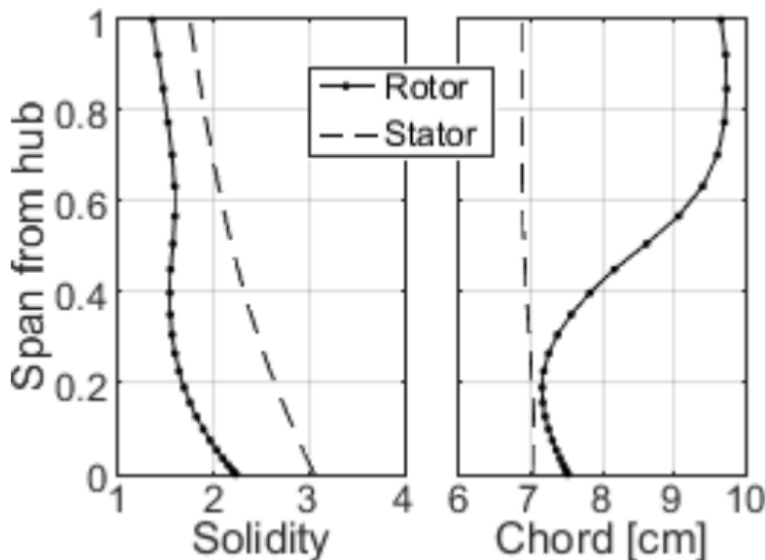


Figure 3.6 : Blade solidity and chord length distributions [28].

Resulting De-Haller (W_2/W_1) and Equivalent Diffusion Factor ($D_{eq}=W_{max}/W_2$) from hub to tip is seen in Figure 3.7.

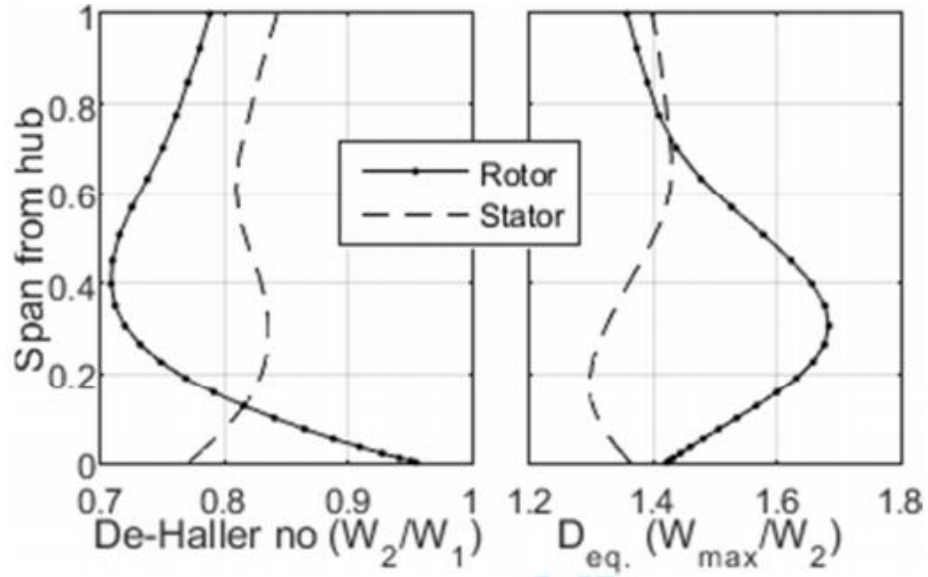


Figure 3.7 : Spanwise distribution of De-Haller number and equivalent diffusion factor [28].

In Figure 3.7, rotor hub De-Haller number reaching to 0.95 indicates reduced loading. This is the reason of higher axial velocity at hub and increased hub diameter (from rotor LE to TE). In respect to De-Haller number, stator hub is highly loaded within an acceptable levels (>0.72). In addition, higher solidity makes the Equivalent Diffusion Factor suitable for both rotor and stator. The De-Haller number is;

$$\text{De-Haller} = \frac{W_2}{W_1} \quad (3.3)$$

and Equivalent Diffusion Factor is as follows;

$$D_{eq} = \frac{W_{max}}{W_2} \quad (3.4)$$

Apart from all of these design parameters, the intake duct and the nosecone of fan (out of this study) were designed roughly so as to assume inlet diffuser effect. Core and bypass ducts were also rough designs which both will be further investigated in the future. Core and bypass lengths are determined by utilizing the experimental data of an annular diffuser [40] for an appropriate flow reattachment (pressure recovery).

Using Inlet Guide Vanes (IGV) as an alternative configuration were considered due to the stator which has high inlet Mach and high loading at hub region. IGV's role in this concept was to increase Mach by creating counter-swirl at upstream of the rotor. As a result, rotor exit and stator inlet flow swirl could be reduced for the same energy

consumption. To prevent choking risk of off-design performance, swirl values were not aggressive, instead kept relatively small. Reduction of stator hub loading by IGV did not change the flowpath, but splitter front nose was rearranged in order to provide desired bypass ratio (Figure 3.8).

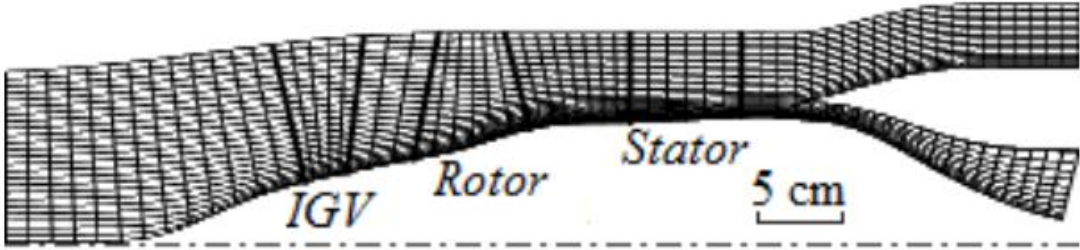


Figure 3.8 : Computational domain of LPC with IGV [28].

Counter-swirl provided by IGV would further relax rotor tip and reduce losses. However, it was actually as a result of hub performance deterioration. To avoid this negative effect, rotor tip had a counter-swirl to improve hub performance. Spanwise counter-swirl distribution of the IGV exit beta angle is presented in Figure 3.9.

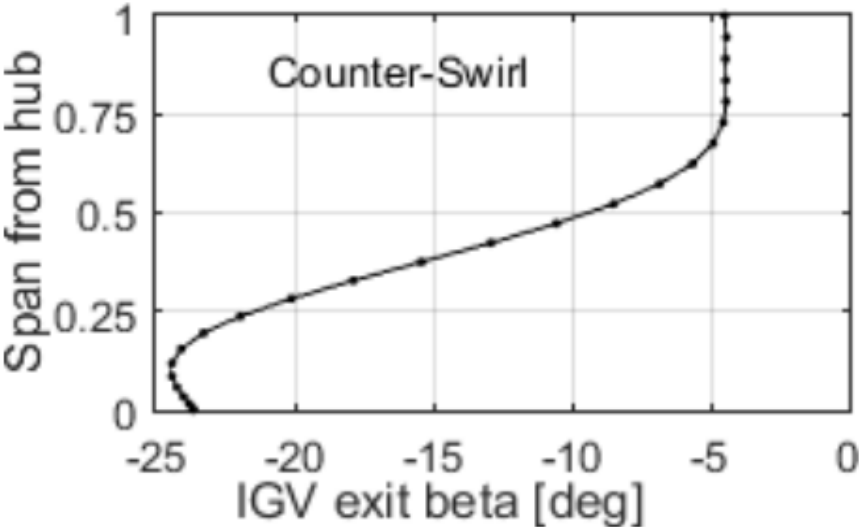


Figure 3.9 : Spanwise counter-swirl distribution [28].

As a result, inlet Mach number at the stator hub was reduced (from 0.85 to 0.75) by using IGV. Besides, De-Haller number at the stator hub was increased to more reliable value (0.83). Apparently, stator hub loading was reduced. In addition, less aggressive rotor twist assured the structural strength. De-Haller and Mach number spanwise distributions were shown in Figure 3.10.

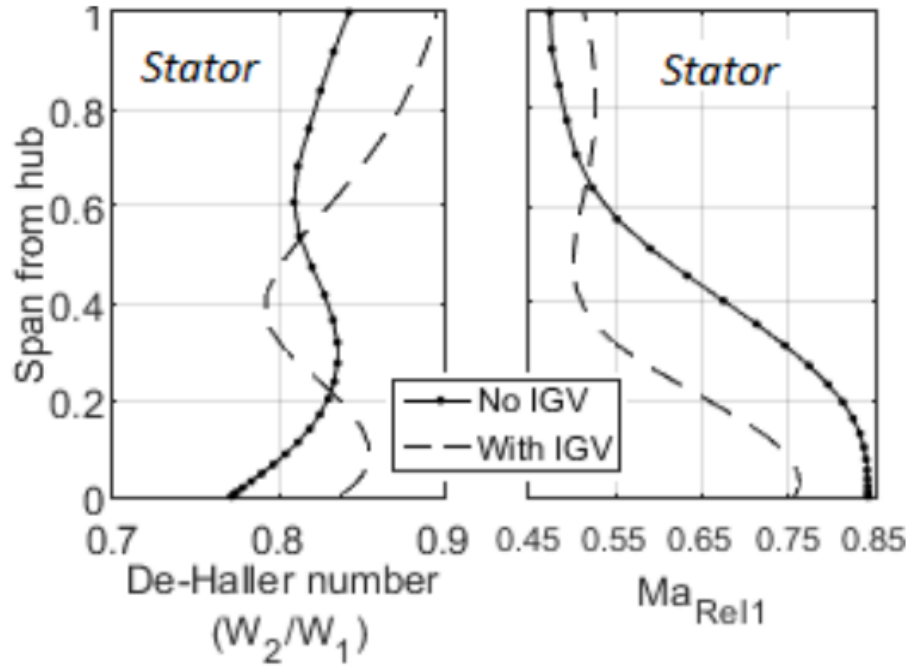


Figure 3.10 : IGV effects on stator [28].

However, using IGV takes away the simplicity of the LPC system. It also disturbs upstream flow and increases choke risk due to its nozzle behaviour. IGV-rotor interaction increases resonance risk of rotor and shock interaction. Comparison of overall performance prediction is presented in Table 3.2.

Table 3.2 : Overall performance comparison with and without IGV [28].

	Core Section			Bypass Section			Bypass ratio
	\dot{m} [kg/s]	Π	$\eta_{\text{isentropic}}$	\dot{m} [kg/s]	Π	$\eta_{\text{isentropic}}$	
Without IGV	1.250	1.61	0.937	5.480	1.41	0.843	4.38
With IGV	1.253	1.62	0.907	5.477	1.42	0.826	4.37

Obviously, IGV adversely effects core and bypass efficiencies (drops 3 points for core, 1.7 points for bypass). These efficiency drops eliminate the positive effects of IGV. Radial equilibrium and choke limit of IGV do not allow to recover or even reduce efficiency drops. Although, throughflow design method uses correlation based predictions, it is a key tool to estimate IGV effect for the system performance. Therefore, it is decided to use the concept without IGV. The following sections were proceeded by considering only one-stage (rotor-stator) design.

In the previous paragraphs, the preliminary design was explained and it is performed by using fast approach of two-dimensional axisymmetric and correlation-based (low-fidelity) inverse throughflow approach. High-fidelity three-dimensional computational

fluid dynamics (CFD) numerical simulations are necessary to evaluate accurate aerodynamic performance and to rearrange design modifications whenever required. Three-dimensional design requires axisymmetric flowpath of the LPC system, spanwise distribution of inlet and exit metal angles and minimum and maximum thicknesses which were obtained from the preliminary throughflow design tool. As determined before, DCA blade cross-sections by stacking method were used to generate rotor blades and stator vanes. LE and TE of rotor and stator were designed as circles (1 mm diameter) to provide better off-design performance and structural strength. Rotor tip gap which is crucial for off-design performance was determined as 0.5% (0.25 mm) of the rotor span. Three-dimensional final geometry is shown in Figure 3.11.

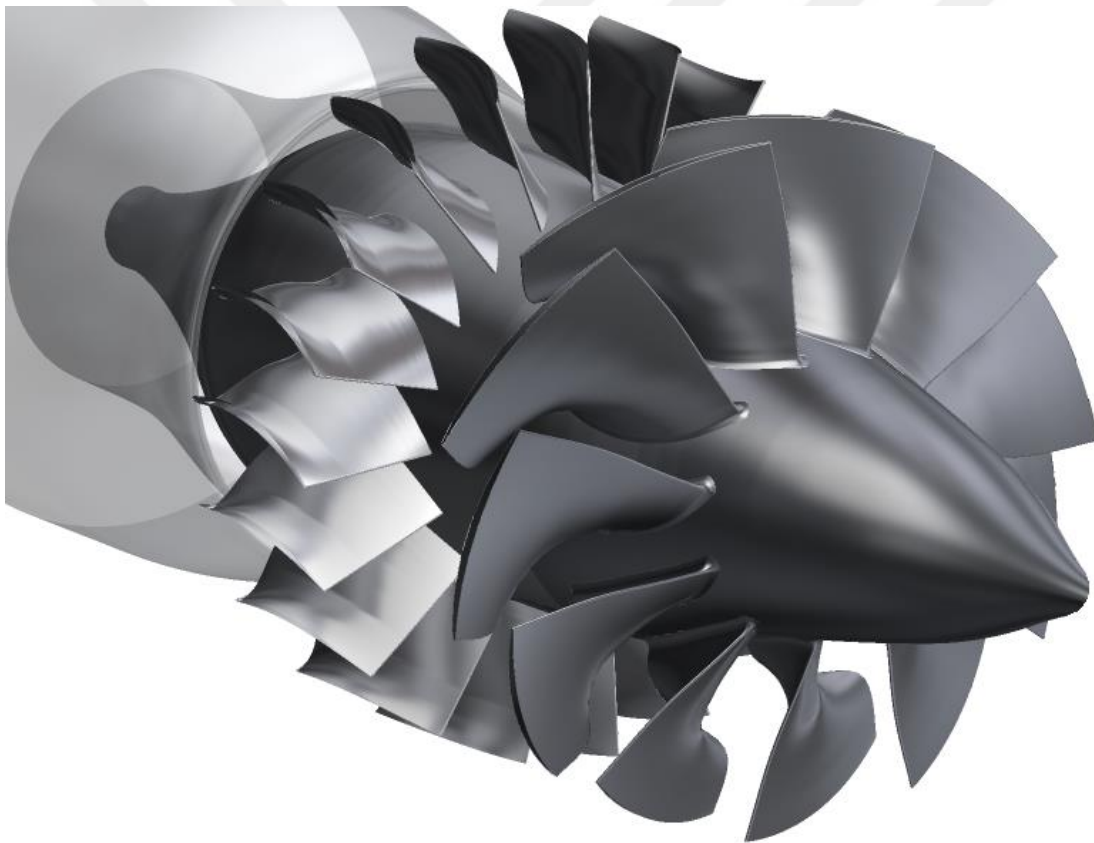


Figure 3.11 : Three-dimensional LPC system without IGV.

In Chapter 2, validation study of NASA Rotor 37 was done and it showed a good agreement with the experimental data and provided mesh-independent solutions. Same adjustments and models were applied for 3D LPC design without IGV (seen in Figure 3.11). Medium level mesh properties were defined and generated for the design. The periodic domain of the LPC system is presented in Figure 3.12.

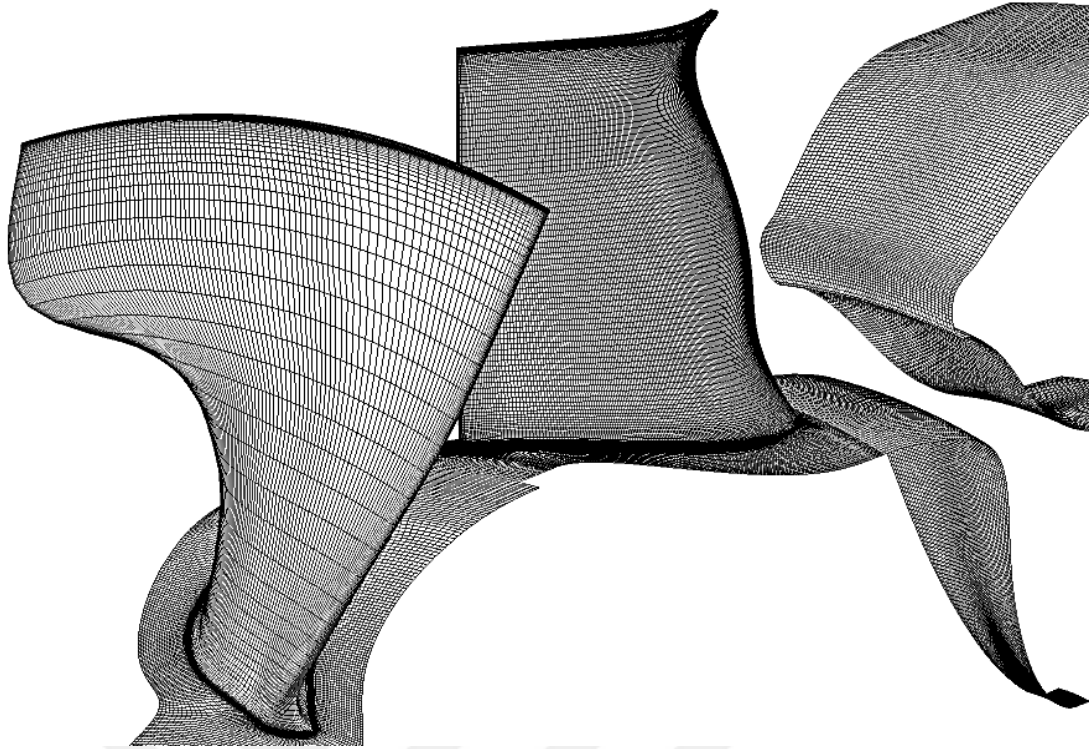


Figure 3.12 : Computational mesh of LPC at surfaces.

Boundary condition at the interface between rotor and stator flow domain was created as mixing plane. This condition averages the flow circumferentially, yet allows radial distribution effects. Total values were defined as total pressure (101325 Pa) and total temperature (288.15 K) at the inlet. Mass flows were defined at the core and bypass ducts outlet (see Table 2) to keep the bypass ratio stable at the design point. Nominal velocity of 29000 rpm was defined for rotor walls and rotor hub.

On-design CFD simulations of three-dimensional design provided accurate results from upstream inlet to stator trailing edge. However, at the outlet core section the results were quite different from the target. The main reason was mixing downstream losses of highly-loaded, transonic stator hub. Total pressure ratio reduced from 1.6 at the trailing edge of the stator to 1.51 at the core outlet. Dependent total-to-total isentropic efficiency considerably decreased from 87.4% to 79.1%. On the contrary, mid and tip section losses which were reasonably loaded, were in negligible level. To prevent mixing losses of core and bypass ducts, optimization study was performed by two-dimensional CFD calculations. Optimized losses were 2.5 kPa for core and 0.7 kPa for bypass duct at the design point. Eventually, stator downstream loss was obtained by subtraction of these losses from three-dimensional CFD results.

Moreover, highly-loaded, transonic stator downstream losses were studied. Without changing the basic design of the stator, some new configurations were created in order to minimize these losses.

There are some options to reduce stator downstream wake mixing losses. Further solidity level is one of them to reduce hub loading of the stator. The other one is to apply three-dimensional design modifications such as bow lean and sweep. Increasing number of stator blades would also reduce loading and increase solidity. However, more blades reduce the pitch distance and make the manufacturing process difficult and results further increase of mid and tip solidity which is not desired. Therefore, the first and second options were applied and three new configurations modified from the original geometry. It can be seen in Figure 3.13, Case A represents the original geometry of the stator, Case B represents 50% increased hub solidity (from 3 to 4.5), Case C's hub solidity level was similar to Case A (seen in Figure 3.13 with three-dimensional view), yet bow-lean and aft-sweep was employed, Case D had the same hub solidity as Case B, but tip solidity was reduced by 20%.

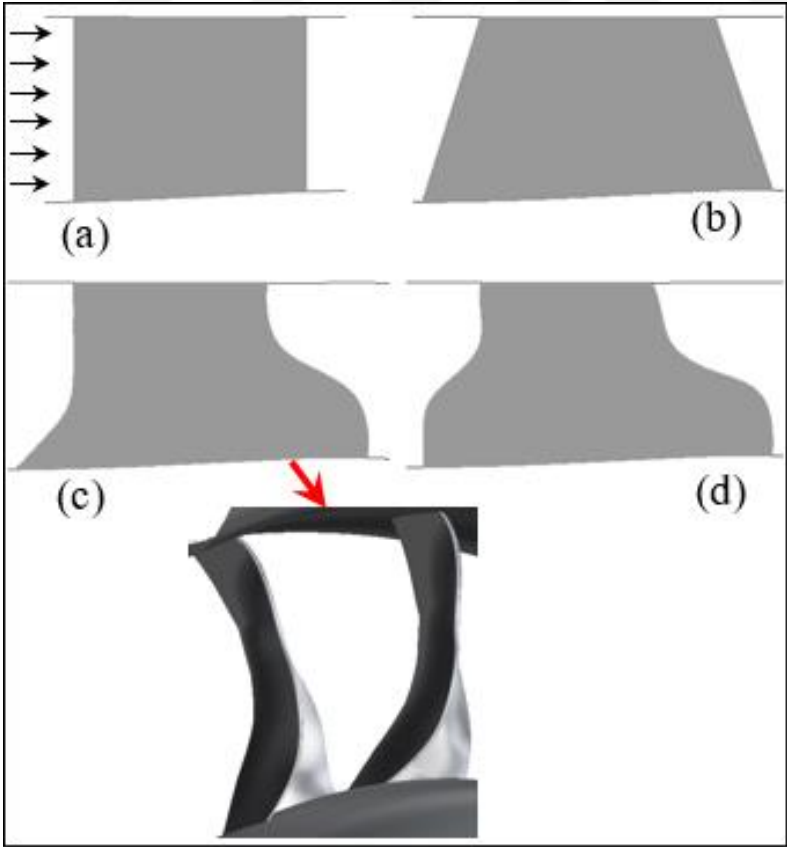


Figure 3.13 : Different stator configurations; (a) Case A (original geometry), (b) Case B, (c) Case C, (d) Case D [28].

Table 3.3 shows three-dimensional CFD results at the design point with four different stator configurations. Inlet was taken half chord upstream of the rotor to get total pressure ratio and isentropic efficiency results. Three different stations were considered for the outlet;

- Stator Trailing Edge (no mixing loss)
- Half-chords downstream (some mixing losses)
- Three-chords downstream as core and bypass outlets (all mixing losses included)

Table 3.3 : Overall performance study for four different stator configurations [28].

CASE A (ORIGINAL STATOR)		Π	η_{isent} (%)	CASE B		Π	η_{isent} (%)
Stator Trailing Edge	Core	1.6	87.4	Stator Trailing Edge	Core	1.6	87.1
	Bypass	1.39	83.1		Bypass	1.38	82.6
Half Stator Chord Down	Core	1.56	84.7	Half Stator Chord Down	Core	1.58	85.8
	Bypass	1.39	82.9		Bypass	1.38	82.2
Three Stator Chords Down	Core	1.51	79.1	Three Stator Chords Down	Core	1.54	80.3
	Bypass	1.38	80.4		Bypass	1.37	79.6
CASE C		Π	η_{isent} (%)	CASE D		Π	η_{isent} (%)
Stator Trailing Edge	Core	1.6	87.3	Stator Trailing Edge	Core	1.6	86.9
	Bypass	1.39	83.5		Bypass	1.39	83.1
Half Stator Chord Down	Core	1.58	85.7	Half Stator Chord Down	Core	1.58	85.4
	Bypass	1.39	83		Bypass	1.39	82.7
Three Stator Chords Down	Core	1.53	79.6	Three Stator Chords Down	Core	1.54	80.2
	Bypass	1.38	80.5		Bypass	1.38	80.3

Bypass efficiency levels were relatively low (~83%) comparing to core at the stator trailing edge because of the relaxed tip section. On the other hand, hub region efficiency levels were up to 87% and desired pressure ratios were achieved without considering mixing losses. Having 4.5 hub solidity, Case B provided almost the desired results, except the efficiency of the bypass region due to linear taper from hub to tip. Applying variant bow lean values by several simulations, Case C did not improve the situation at the hub region, and tip performance was slightly increased by using lower tip solidity. Case D having almost the same hub solidity as Case B, besides using improved bypass performance as Case D, was chosen for the final

design of LPC system. Three-dimensional final concept of the LPC system with modified stator and spanwise pressure ratio distribution comparison between throughflow and CFD calculations for only rotor and rotor+stator (stage) are presented in Figure 3.14.

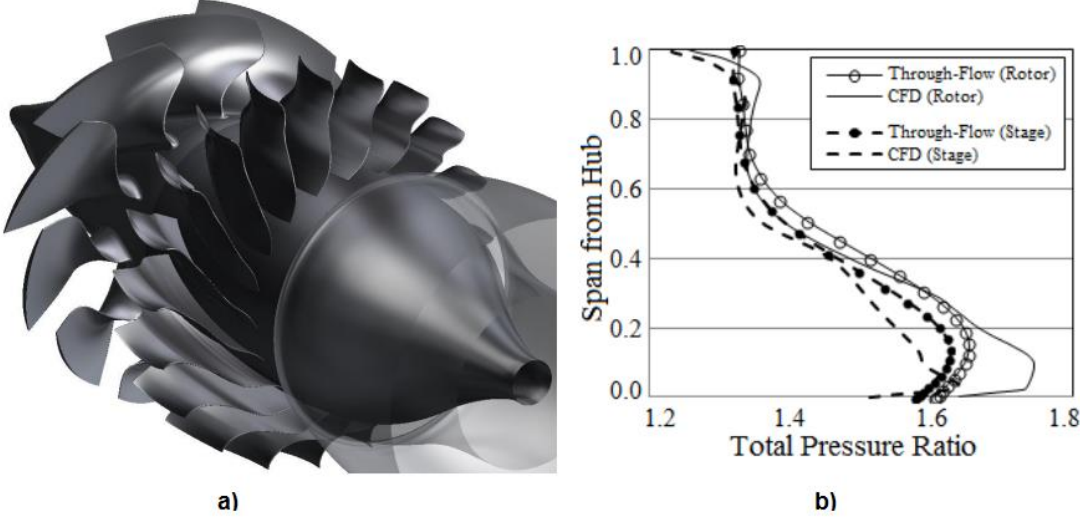


Figure 3.14 : a) Final LPC geometry, b) Spanwise pressure distribution comparison [28].

3.2 Aerodynamics Off-design Performance Investigation

In this section detailed aerodynamics and off-design performance of the novel unified-LPC system was presented. The design point was determined as near choke condition so as to create a better stall margin. The performance maps of core and bypass streams are presented in Figure 3.15.

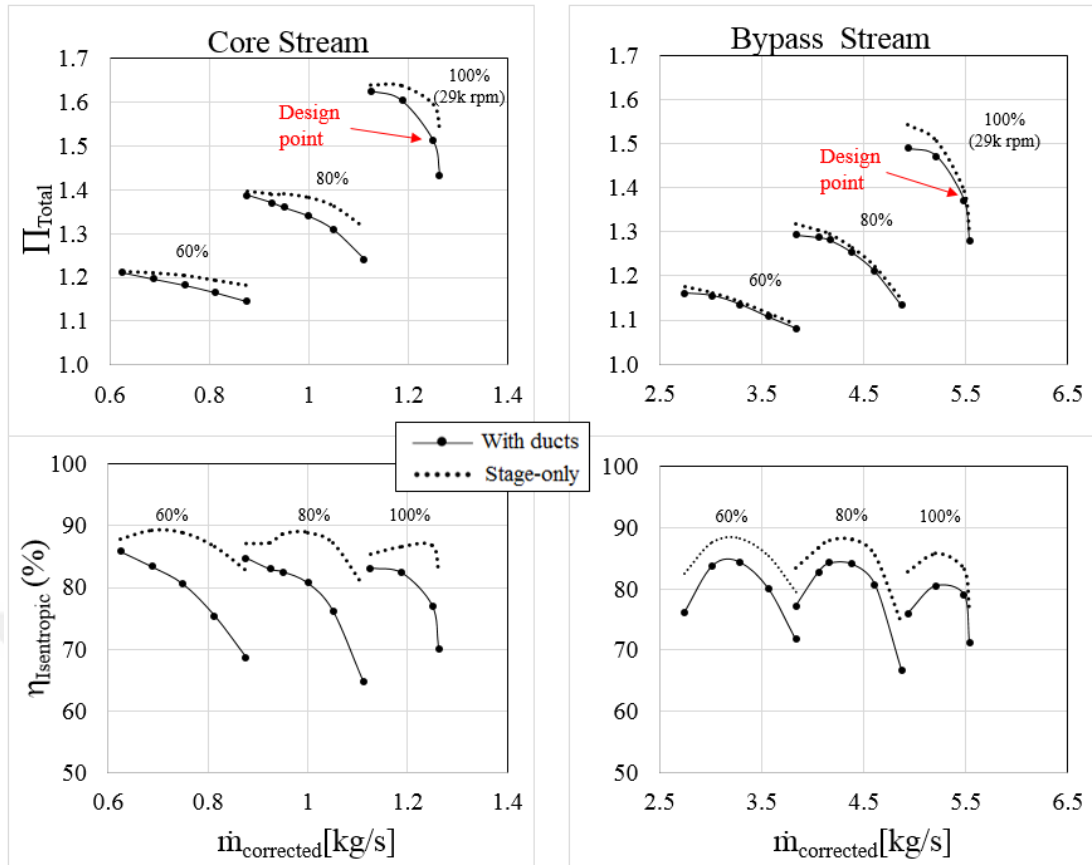


Figure 3.15 : LPC system performance maps.

In Figure 3.15, except nominal (take-off) speed (29000 rpm), low speed performance maps (60% and 80% of the nominal speed) were also presented. The calculated results were obtained for a constant bypass ratio of 4.38 that was determined and mentioned in section 3.1.1 (Design of the fan), and by changing the outlet mass flow rate. The maps were presented for both stage-only section considering downstream near stator TE, and stage+ducts considering mixing loss, core and bypass duct losses. Including non-optimized duct shapes, the performance results might not be properly evaluated at off-design condition. Optimized duct shapes (primarily core duct) could reduce the duct losses. In Figure 3.15, the design point is near choke condition as it was intended in the preliminary design step. This design point (at take-off) corresponds approximately 20% stall margin defined by GE (General Electric) in Equation 3.5 [41] and acceptable 15% stall margin defined by N.A. Cumpsty in Equation 3.6 [42]. These definitions for stall-margin also include the downstream duct losses. Stall margin values indicate that the operating range is improved in return for slight efficiency reduction. The stall margin definition by GE;

$$\text{Stall margin}_{\text{GE}} = \left(\frac{\Pi_{\text{stall}}}{\Pi_{\text{design}}} * \frac{\frac{\dot{m}_{\text{in}} \sqrt{\theta}}{\delta_{\text{design}}}}{\frac{\dot{m}_{\text{in}} \sqrt{\theta}}{\delta_{\text{stall}}}} - 1 \right) * 100\% \quad (3.5)$$

The stall margin definition by N.A. Cumpsty;

$$\text{Stall margin}_{\text{Cumpsty}} = \left(\frac{\frac{\dot{m}_{\text{out}} \sqrt{\theta}}{\delta_{\text{design}}}}{\frac{\dot{m}_{\text{out}} \sqrt{\theta}}{\delta_{\text{stall}}}} - \frac{\dot{m}_{\text{out}} \sqrt{\theta}}{\delta_{\text{design}}} \right) * 100\% \quad (3.6)$$

Throughflow code prediction and calculated CFD-Post total pressure distribution on meridional plane at design-point are presented in Figure 3.16.

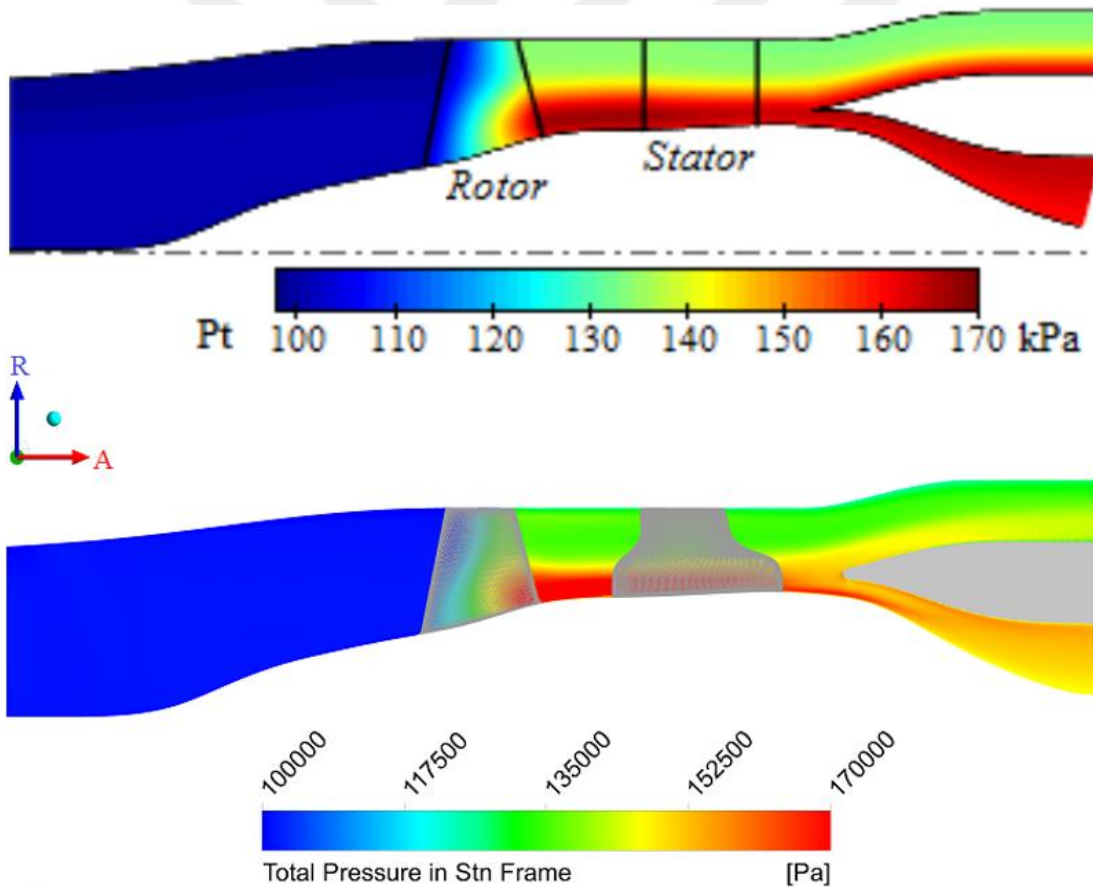


Figure 3.16 : Comparison of Throughflow code and CFD numerical solver at design point.

2D throughflow code [31] result which was already presented in Figure 3.2 shows great agreement with the calculated results and the code validates its reliability for

the turbomachinery preliminary design step. On the other hand, it does not take into account of downstream mixing losses (see the downstream of the ducts).

LPC system velocity streamlines can be seen in Figure 3.17. The streamlines demonstrate a typical turbomachinery stage flow behaviour through the rotor and the stator. The flow is smoothly separated to each duct due to the diffuser structure.

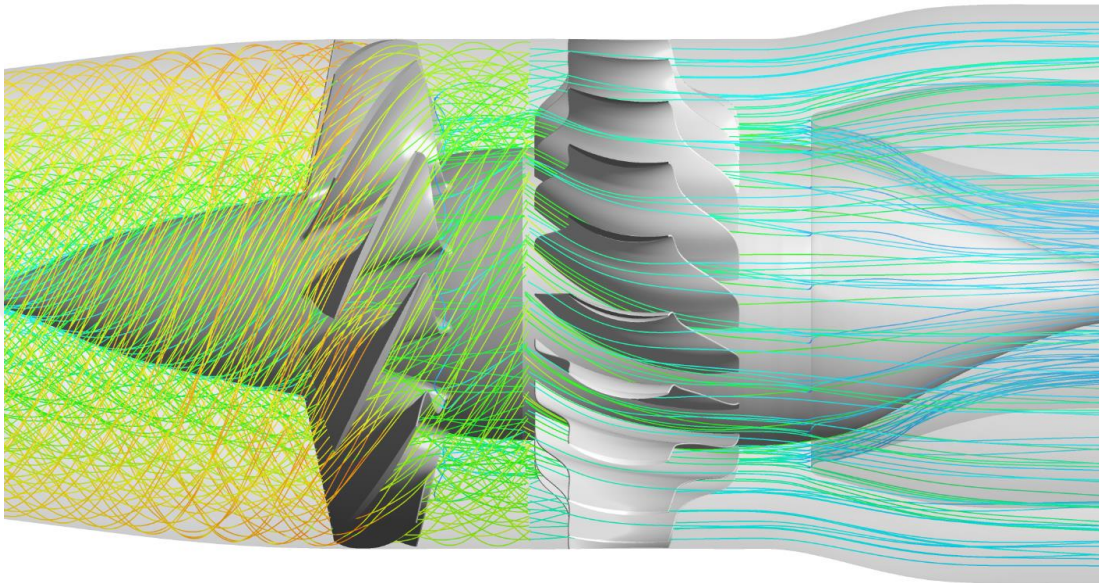


Figure 3.17 : LPC system velocity streamlines.

Detailed aerodynamics off-design investigation of the LPC was demonstrated with respect to rotor and stator blades. In figure 3.18, blade-to-blade relative Mach distribution for three operating conditions (near-stall, design point, near-choke) at nominal speed (29000 rpm) is shown from near-hub to near-shroud.

The shock formations for all three operating conditions at 0.9 span confirm the demonstration of Benini's [43] shock structure formations. The shock is formed upstream of the blade and it is less inclined to incoming flow at the stall condition. Because lower mass flow rates and higher incidence make the shock less inclined. The shock structure at the choke condition develops further shock downstream of the main shock and it is more inclined to the incoming flow. However, the design condition shock formation should normally create one main shock which should bifurcate to incoming flow at the leading edge. Instead, the main shock creates another further but weaker secondary shock near the trailing edge suction side as it only happens in choke operation. The reason is that the selected design point of the LPC (see Figure 3.15) is close to the choke point.

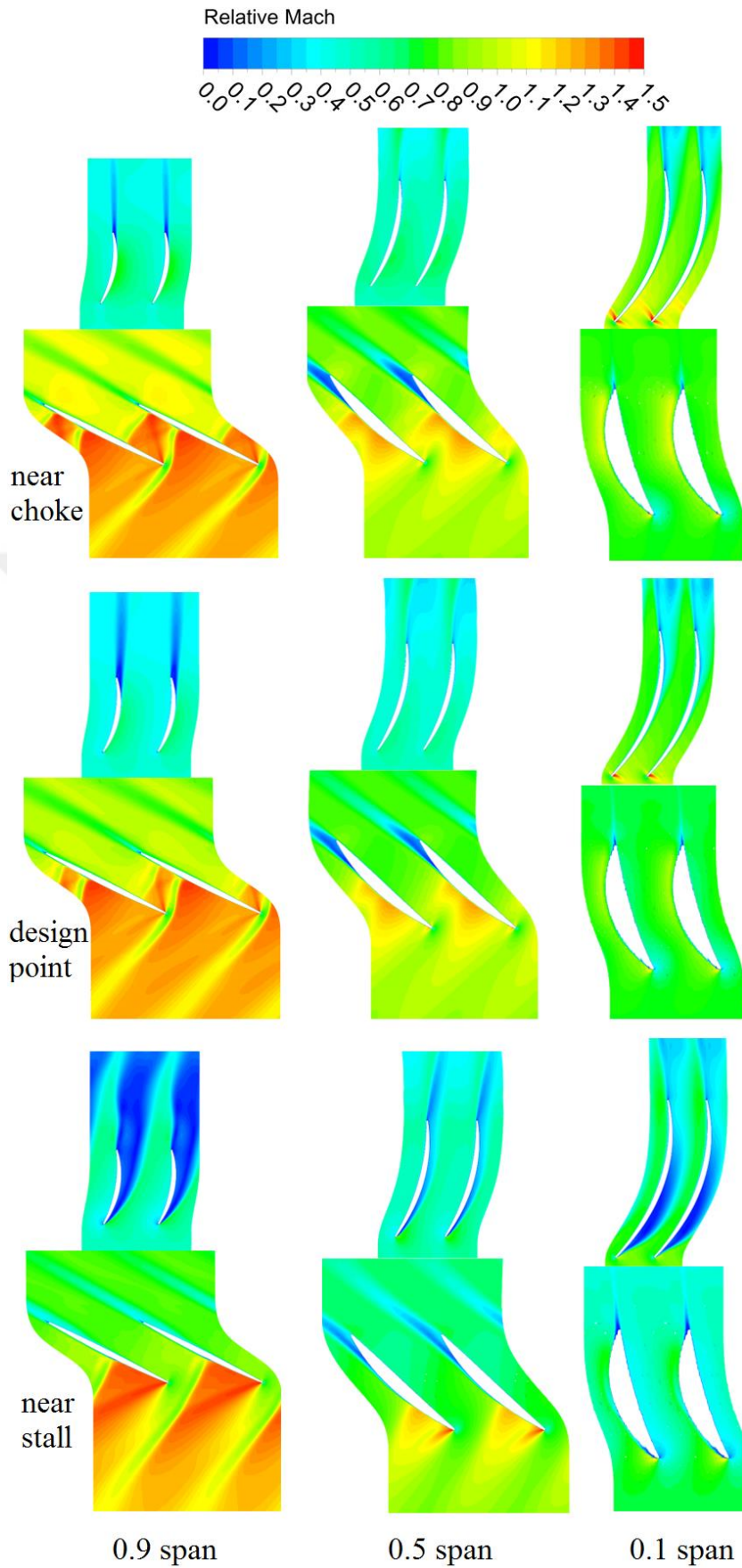


Figure 3.18 : Relative Mach distribution for three operating conditions; near-choke (top), design point (mid), near-stall (bottom).

At the design point, near hub (0.1 span) there is a spike (local acceleration) both for rotor and stator leading edges. The spike is stronger at the stator leading edge for near-choke and creates a passage shock there. This situation is normal and it is not possible to avoid due to the circular leading edge shape. The sudden acceleration is the result of a dramatic increase of the local static pressure just after the leading edge of the rotor and the stator (Figure 3.19). There is also a low-momentum region through the trailing edge which induces downstream mixing losses. Near hub, this low-momentum region is much bigger for near-stall operation and smaller for near-choke operation. The flow separates from the leading edge of the stator and creates a very large separation bubble for near-stall condition near hub. Meanline blade-to-blade view shows two acceleration zones at the rotor suction side for design point. It does not have a major effect on the performance and could be avoided with a further design optimization. However, this situation creates a shock formation at the leading edge for near-stall condition and for near-choke, the second acceleration zone creates a passage shock formation. There is a flow separation at the stator trailing edge due to the tip leakage flow influence for both design and near-choke condition. At the design step, relaxed tip design with a reduced inlet Mach (~ 0.5) makes this situation unavoidable. Furthermore, near-stall operation, the surprising thing about the stator tip is that there is a complete stall, yet it takes the least attention at the design step. Increasing the solidity or lower incidence angle would be a solution to avoid this issue. However, these solutions could reduce the design point efficiency.

Figure 3.19, chordwise static pressure distribution for three operating conditions are shown for the nominal speed of 29000 rpm. The first noticeable thing in the figure is that the static pressure trend of design point and near choke condition shows considerable increase between 0.6 and 0.9 streamwise locations. It is the reason of the double shock structure formation at the tip region which is also seen in Figure 3.18. The shock structures are clearly visible on blade surface with red dashed-lines in Figure 3.20. However, the second shock of the design point is weaker than the near-choke and it reflects its impact with relatively small static pressure rise in Figure 3.19. Another important thing, the overall blade loading is getting higher from near-choke to near-stall condition. At near-stall, this trend increases the unsteadiness of fan rotor. However, it is a normal behaviour for such a transonic rotor blade. At the trailing edge of the rotor and the stator (near 1.0 chordwise position), a flow

migration happens from pressure side to suction side which is a common and an unavoidable aerodynamic phenomenon for turbomachinery blades.

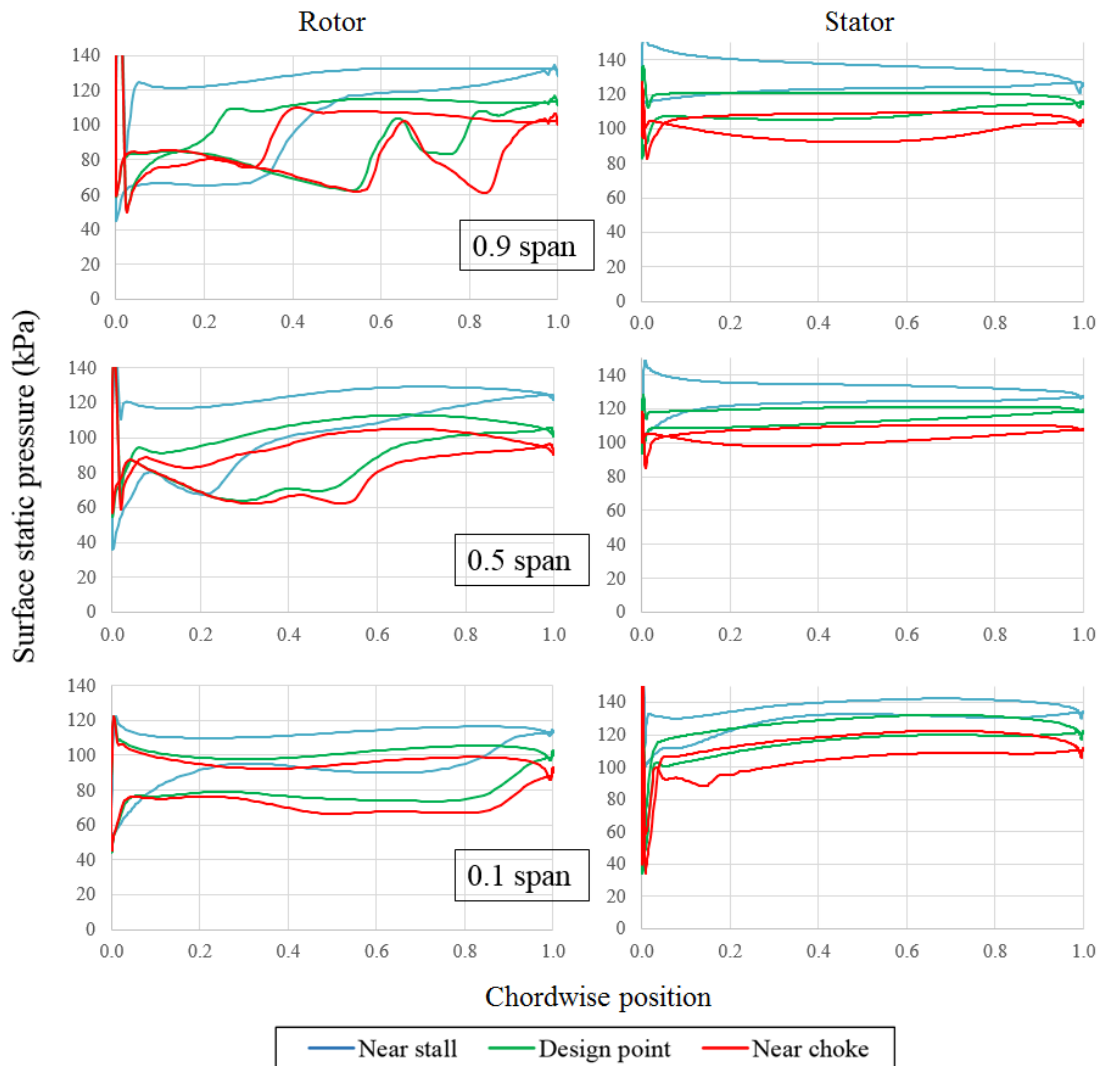


Figure 3.19 : Static Pressure chordwise distribution for 0.9 (top), 0.5 (mid), and 0.1 (bottom) spans.

Figure 3.20 demonstrates the static pressure distribution on the rotor blade surface both for Suction Side (SS) and Pressure Side (PS) at nominal speed. The red-dashed-lines represent the shock formation through different operating conditions. The boundary of the shock is becoming thicker from near-stall to near-choke condition. There is a local static pressure rise near the SS leading edge (mid to tip region) both for near-choke and design point operations. Since, relatively higher angle of attack for the rotor blade tip region makes the flow quasi-stagnated. For the near-stall operating condition the longest radial shock formation is observed. It causes a bigger flow separation zone (Figure 3.21) and rises the static pressure and therefore loading

towards the trailing edge (Figure 3.20). Besides, the tail of the shock to the blade root contributes further downstream blade loading.

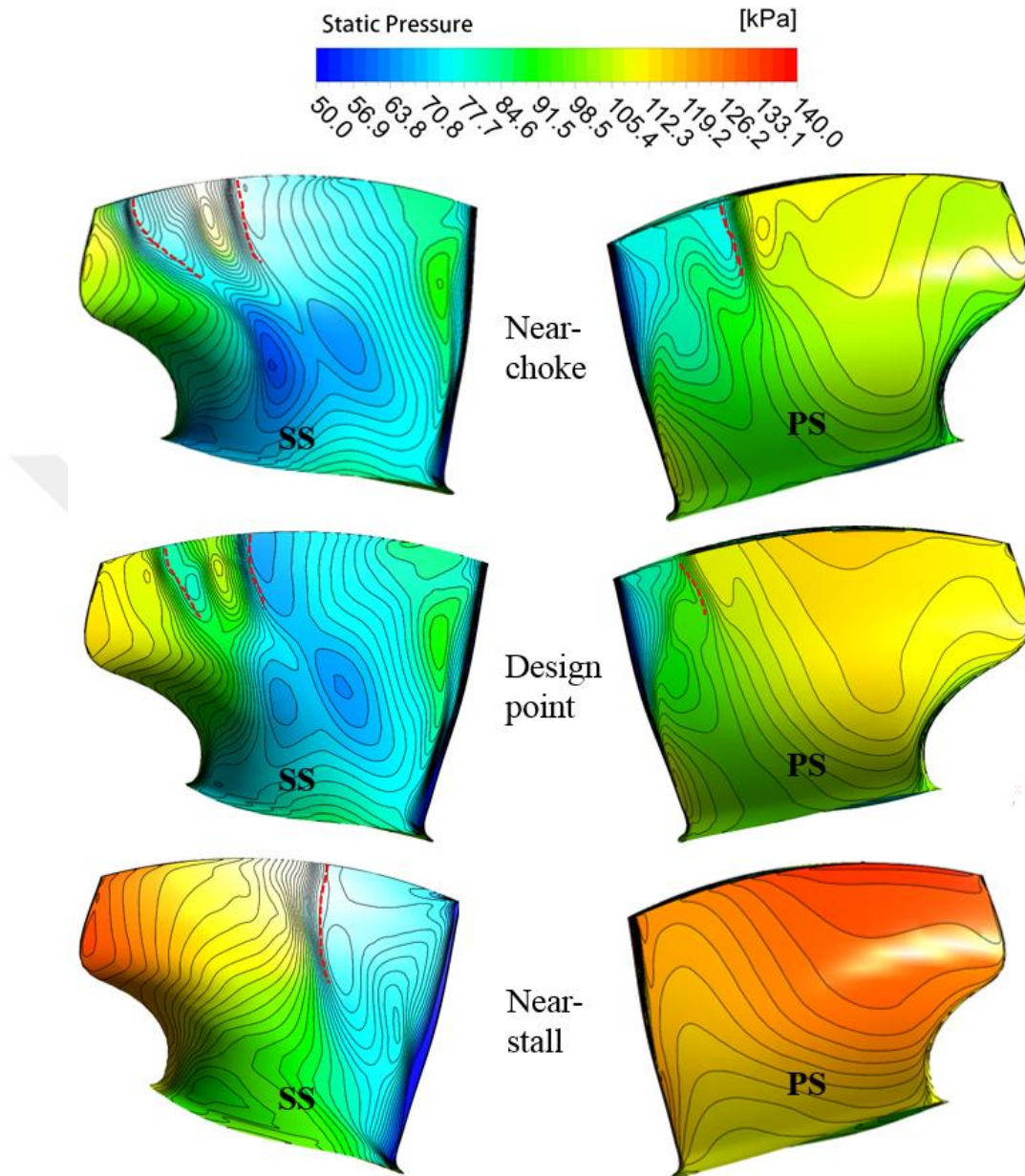


Figure 3.20 : Static Pressure distribution on fan rotor for different operating conditions.

Nominal speed suction side on-blade velocity streamlines are presented in Figure 3.21 from different perspectives. Strong radial fluid migration schemes are observed as the flow interacts with the shock. The shock structure creation gives rise to low momentum fluid accumulation at the tip region which is known to be detrimental for a stable operation. It also causes thicker boundary layer to induce further blade wake development. Therefore, the separation lines reaching the tip region are an indication of the shock formation.

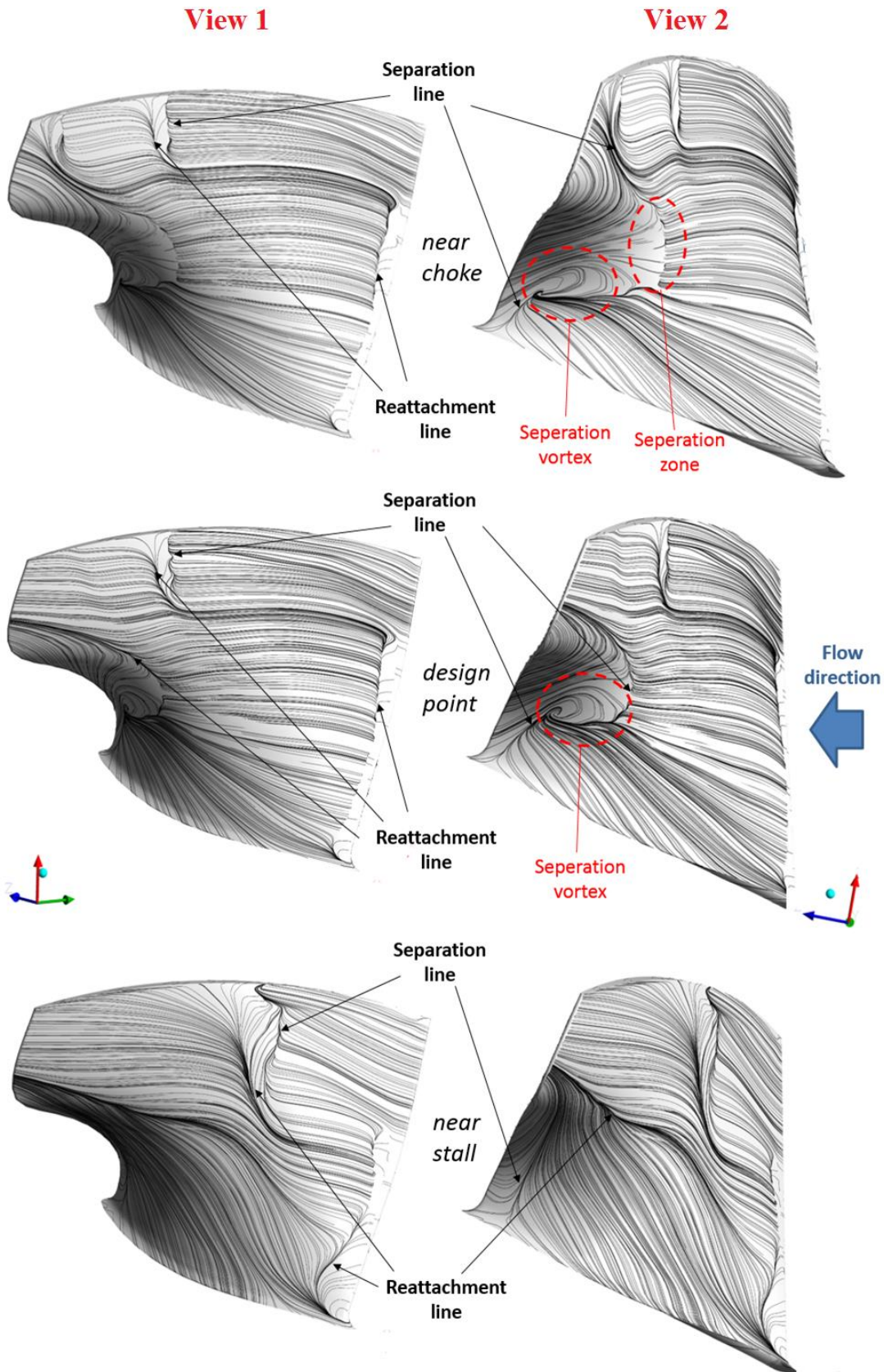


Figure 3.21 : Three operating point streamlines on rotor blade suction side from different perspectives, View 1 (left), View 2 (right).

The separation line due to the shock formation is followed by a reattachment line. The reattachment of the flow is relatively delayed for the near-stall operation with reference to design point.

There is a midspan separation zone for near-choke and design point conditions. The separation zone is relatively weak for design operation and the flow reattachment is provided near the separation. The reason of this phenomenon is the blade over curved geometry to provide highly loaded blade characteristics. Moreover, separation vortex occurs for both operating conditions. This phenomenon is the result of separation zone interaction with the corner stall separation. Near-stall operation, the corner stall separation is longer reaching the midspan region. The corner stall separation also induces the reverse flow for the design point and near-choke condition. As it is seen in Figure 3.21, reverse flow bifurcates and one side interacts with the separation vortex as mentioned, one side migrates above because of the midspan trailing edge extreme curvature. This migration even reaches near tip region at the near-choke condition.

In Figure 3.21, leading edge DCA shape delays flow reattachment. The DCA is not suitable for subsonic flows and it creates leading edge spike that is a common phenomenon for this profile. As a result, the reattachment zone is obvious until 0.7 span blade profile where it begins to become supersonic. Around tip, blade supersonic profile with sharp edges, there is no delay for the flow attachment.

Figure 3.22 shows streamwise absolute Mach distribution (in stationary frame) for design point and near-stall operation at nominal speed. In Figure 3.22, relatively thicker wake appearance is clearly visible at the downstream of the stator tip. It becomes stronger at near-stall operation causing even a complete flow separation at the outer duct. The difference of the Mach between upstream and downstream of the stator is clearly visible. This indicates a dramatic deceleration of the flow. Leaned rotor wakes are also demonstrated in the figure with black-dashed circle. The corner flow separation both for suction side of the stator hub and tip section creates low-momentum zone. The corner flow separation at the hub is weaker and smaller especially due to rotor hub radius increase (partly in stator hub as well) by providing a convergent shape flowpath. As a result, a mostly attached flow enters the core duct. Even strong wake mixing losses occur downstream of the stator, the flow remains attached. Therefore, the design strategy provides its accuracy.

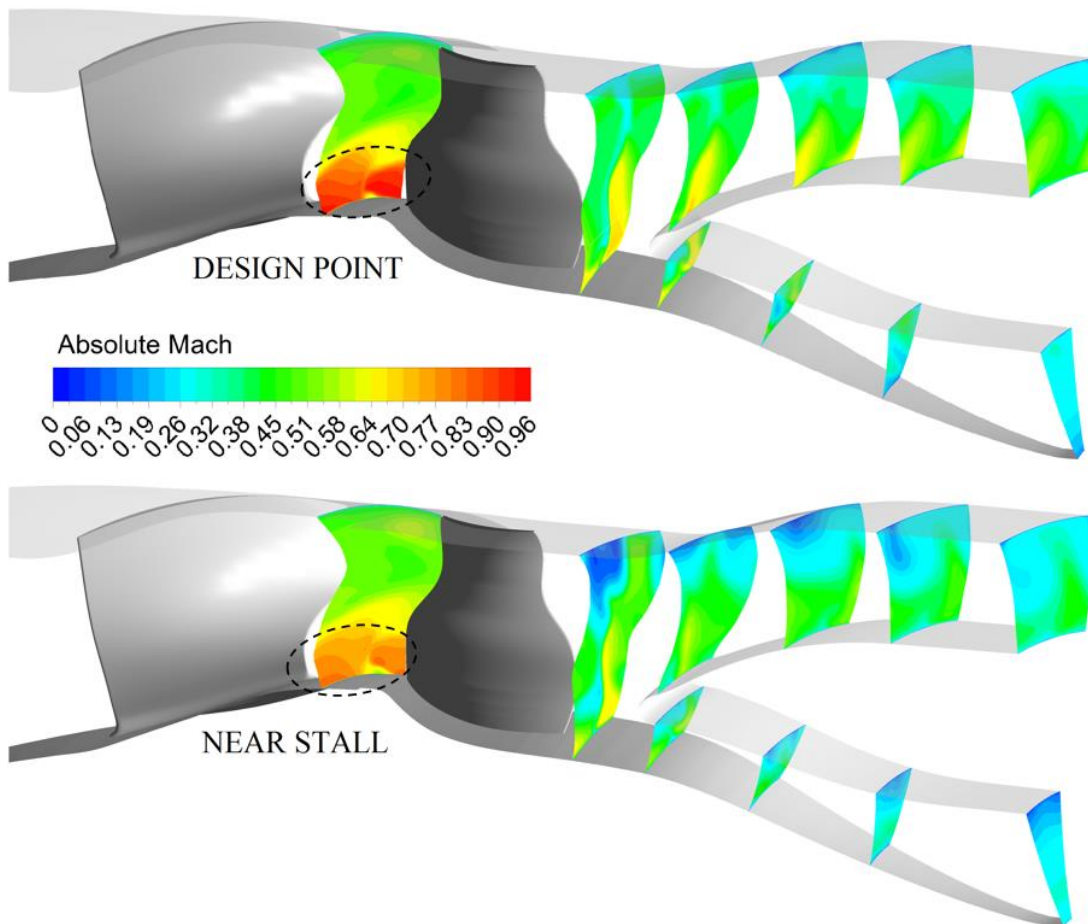


Figure 3.22 : Streamwise distribution of absolute Mach at design point (top) and near-stall (bottom).

Streamwise evaluation of meridional velocity is seen in Figure 3.23. The downstream of the stator pressure side creates an acceleration zone (leaned wake). This accelerated flow divides into core and bypass ducts. The flow is then surpassed at the core duct because of the aggressive S-shaped design. In the bypass duct, it is progressively diffused and weakens at the downstream.

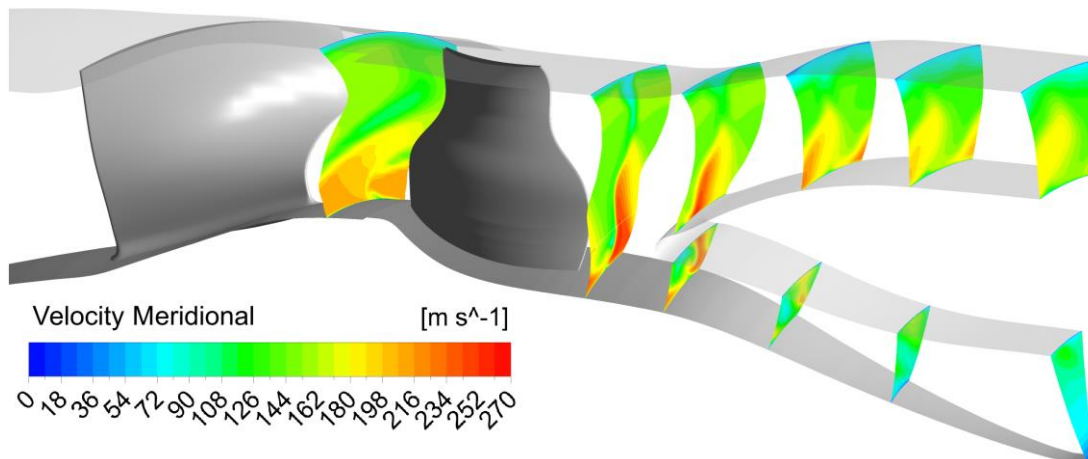


Figure 3.23 : Streamwise meridional velocity evaluation at design point.

Total pressure distribution through the flowpath is shown in Figure 3.24. It is interesting that the rotor downstream flow behaviour is formed an S-shaped low pressure zone corresponding to high momentum zone. This form represents the rotor trailing edge leaned S-shape. It is clearly visible in Figure 3.25, 3.26 and 3.27 as well. It is the reason of rotor pressure and suction side flow instantaneous encountering and mixing. This phenomenon creates intense flow vortices which is seen in Figure 3.25 and 3.26 and the flow vorticity characteristics and shear strain rate of the flow show an analogy. In addition, a similar mixing phenomenon also occurs at the stator downstream. Yet, it is weaker and more stable which does not create further intense vortices and disappears. At the core duct, vorticity characteristics of the flow is very dominant because of the corner stall separation. However, these vortices are disappeared near the core duct outlet due to the high diffusivity.

The boundary layer near tip wall is rather thicker because of the tip leakage flow of the rotor. However, it is smoothly diffused by bypass duct and became thinner (Figure 3.22, 3.25 and 3.26).

In Figure 3.27, turbulent viscosity streamwise evaluation of the flow is demonstrated. Its evaluation similarity with the meridional velocity (Figure 3.23) is clearly visible. Since, the viscosity behaviour is the direct indication of the fluid flow.

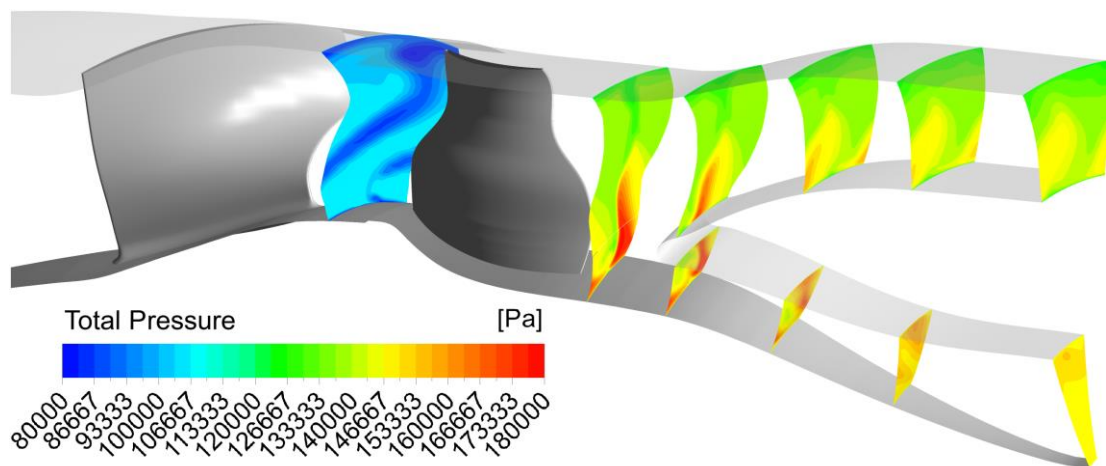


Figure 3.24 : Streamwise total pressure distribution.

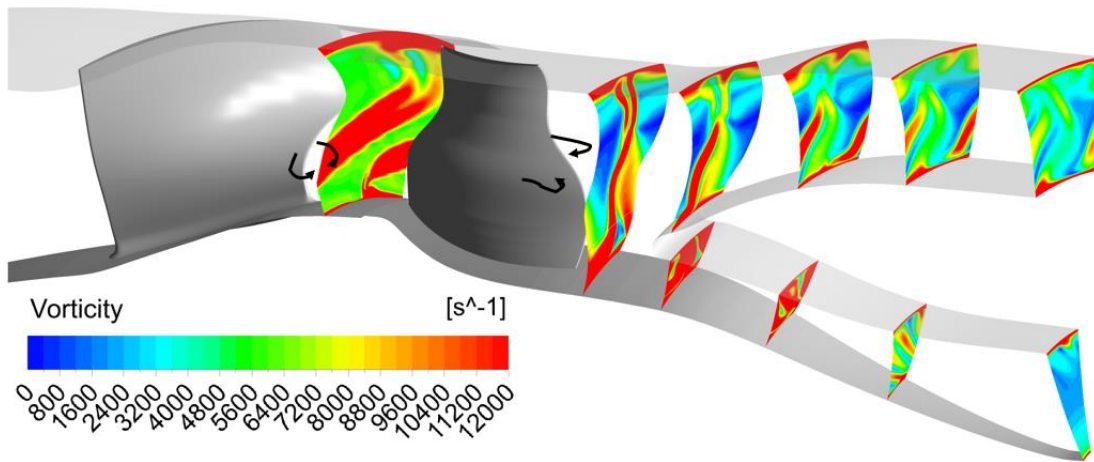


Figure 3.25 : Vorticity characteristics of the flow in the streamwise direction (Higher values were clipped).

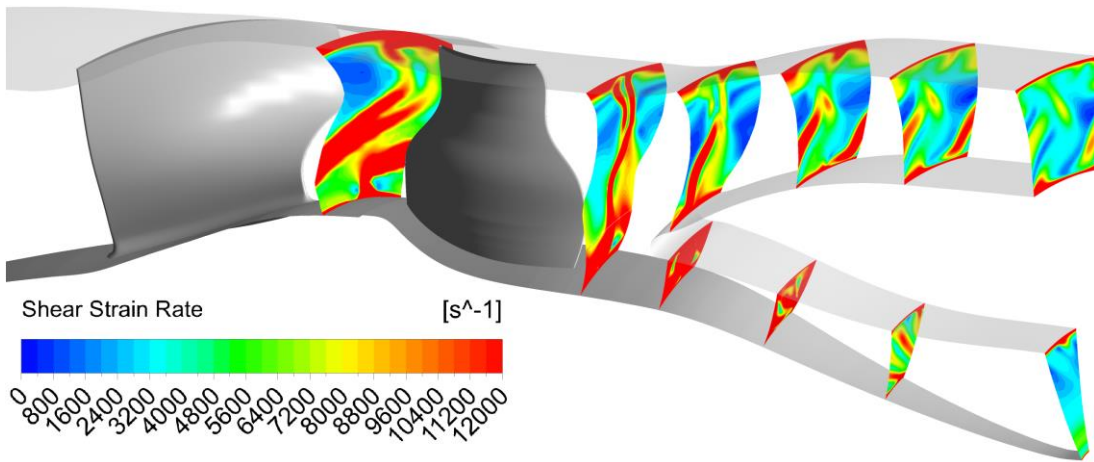


Figure 3.26 : Shear strain streamwise evaluation (Higher values were clipped).

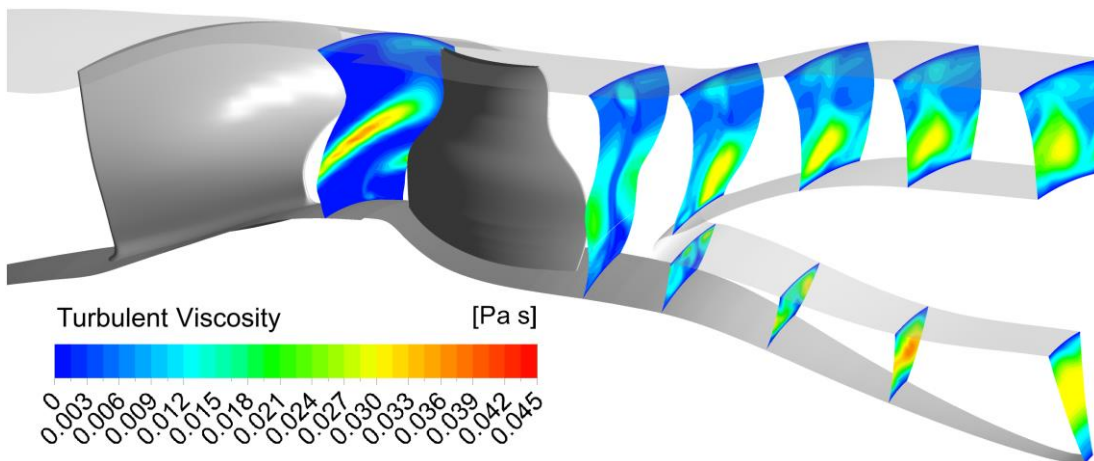


Figure 3.27 : Streamwise evaluation of turbulent viscosity.

Till now, the off-design results are evaluated by considering nominal shaft speed of 29000 rpm. The lower speed operating conditions of the LPC should also be considered to provide sufficient information about the off-design performance. In Figure 3.28, blade-to-blade relative Mach distribution is demonstrated for three

different shaft speeds (100% nominal speed, 80% speed, 60% speed) which their curves are already presented in Figure 3.15. It should be mentioned that the figures are taken from the design point for each individual shaft speed. As it is expected, near-tip (0.9 span) shock formation becomes weaker at 80% speed and another acceleration zone (near-sonic) is observed downstream of the shock on the suction side. It can also be observed in Figure 3.29. The chordwise distribution of the static pressure makes a peak between 0-0.2 chordwise position. This formation becomes weaker at 60% speed near-tip section. There is only a minor acceleration (spike) at the rotor leading edge and no separation occurs because of the lower mass flow levels. Local acceleration or even a weaker shock formation for lower shaft speeds moves away the design point from choke line. As a result performance curve of lower speeds becomes less inclined to choke line (see Figure 3.15) and rather widens operating range which is a normal outcome for such a turbomachinery.

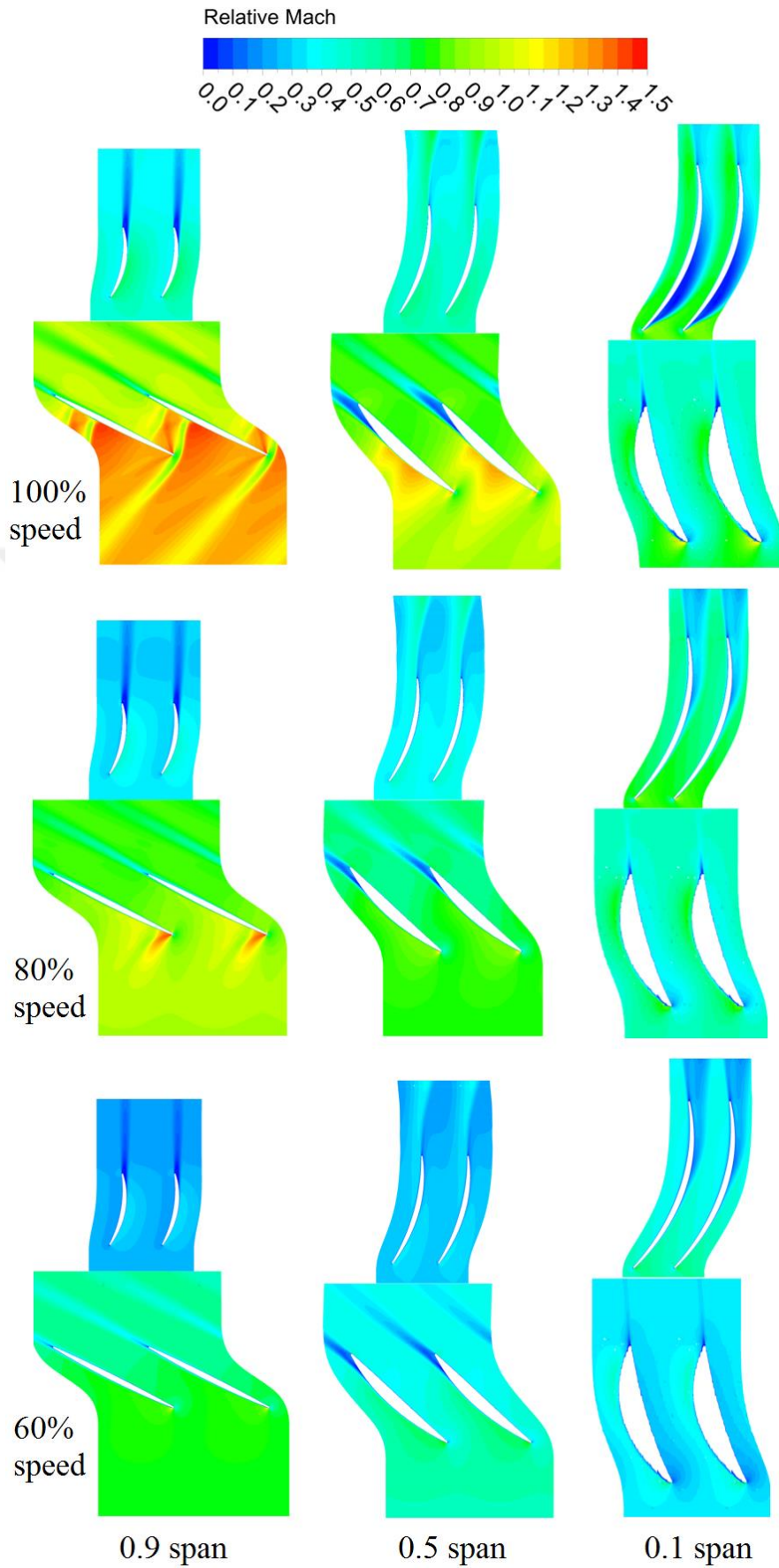


Figure 3.28 : Relative Mach distribution for different shaft speeds; 100% design speed (top), 80% speed (mid), 60% speed (bottom).

In Figure 3.29, near hub static pressure of the rotor increases between 0.8 and 1.0 chordwise positions for the suction side trends. This situation is the reason of the trailing edge flow separation which creates a low momentum zone at the rotor suction side. For all three shaft speeds, it is clearly seen at 0.1 span from the Figure 3.28. This low momentum zone could be eliminated by a relatively moderate convex shape of the suction side or by a wider chord line of the rotor blade. However, these parameters should wisely be considered in the design phase within the whole design perspective.

Another remarkable thing in Figure 3.28, stator near hub large separation zone which begins from the leading edge for nominal speed is disappeared at lower shaft speeds. Both for 60% and 80% operating speeds, this low momentum zone migrates downstream of the stator and weakens in point of size and magnitude.

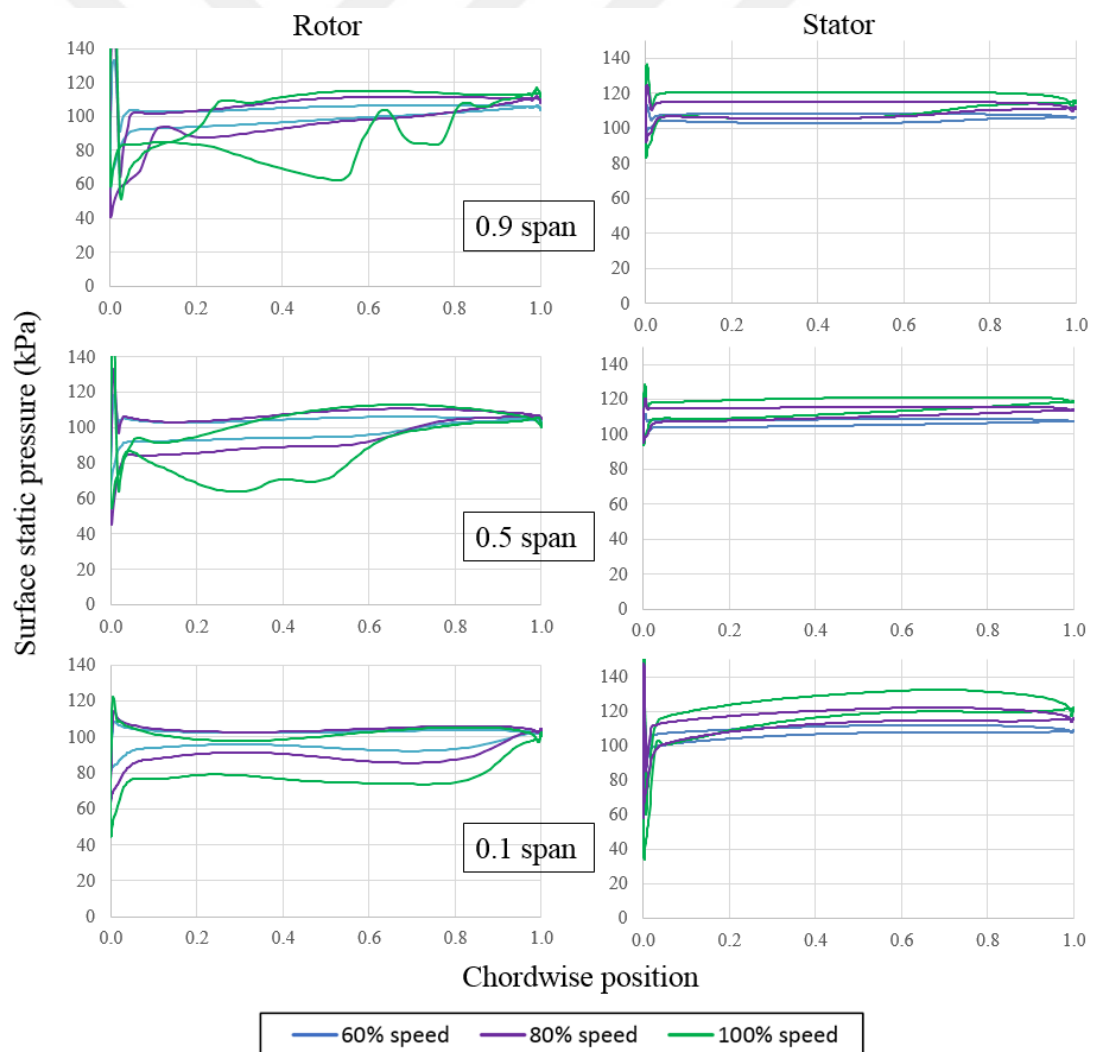


Figure 3.29 : Static Pressure chordwise distribution for 0.9 (top), 0.5 (mid), and 0.1 (bottom) spans.

Tip clearance flow behaviour is another crucial factor and should be detailly investigated. Since, pre-design requirements of the LPC were the result of the tip performance deterioration (see Table 3.1). It is an unavoidable phenomenon for such an unshrouded high speed fan blades and it induces flow instabilities and losses, effecting overall performance negatively. Note that, the rotor tip clearance is 0.25 mm which is approximately 0.5% of the blade span for this fan rotor. Figure 3.30 shows near tip (positioned at 98%), relative Mach distribution of the rotor blades.

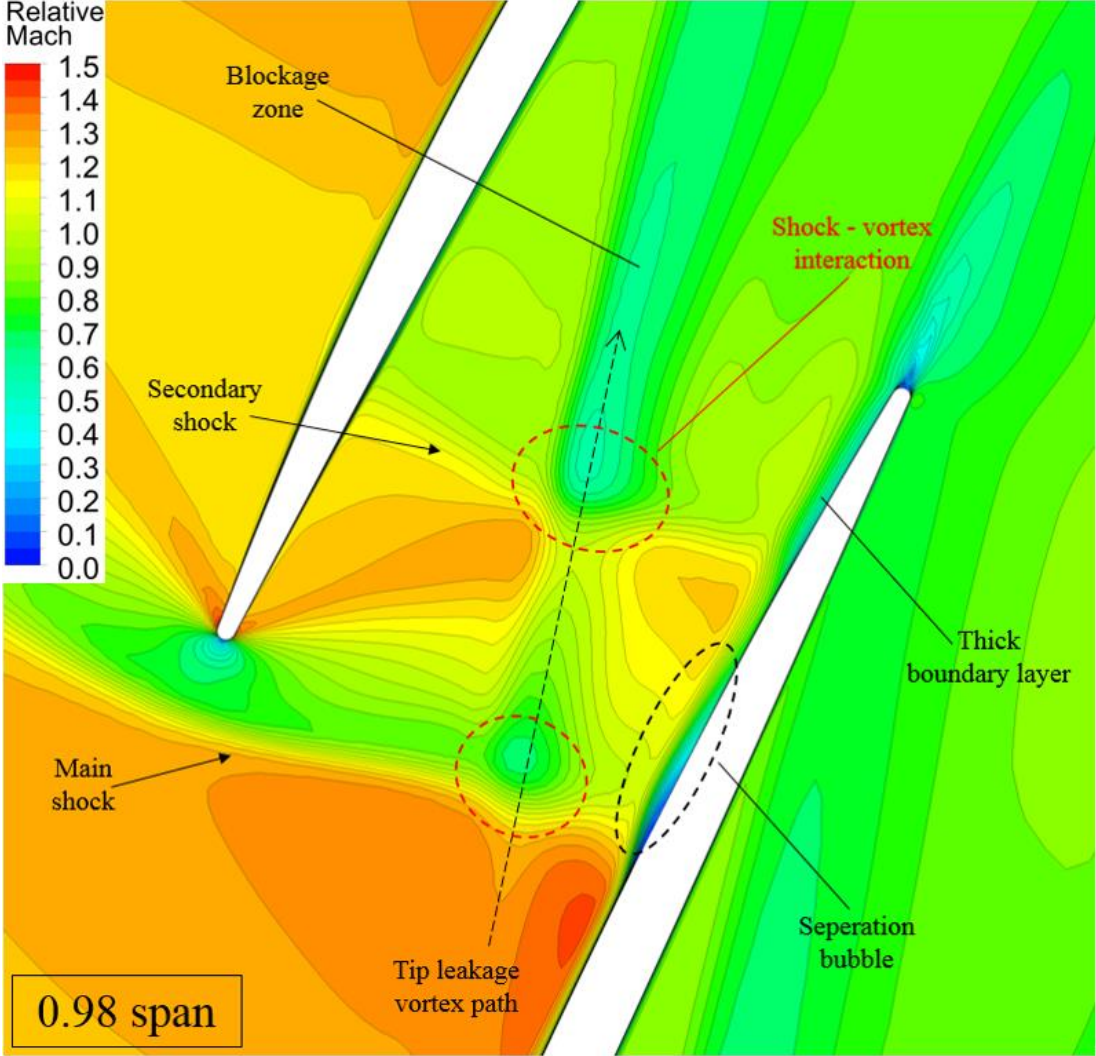


Figure 3.30 : Near tip section (0.98 span) Relative Mach distribution.

It is seen in the figure that the main shock strongly impacts on the rotor blade suction side at the half downstream region by interacting negatively with the local boundary layer. Then, thickening of the boundary layer happens and a seperation bubble is created because of the adverse pressure gradient scheme across the shock. However, the seperated flow is reattached before trailing edge and avoided further blade wakes.

Tip leakage flow also shows itself clearly in the figure. It begins downstream of the leading edge suction side and creates a tip leakage vortex downstream of the passage flow. Tip leakage vortex firstly encounters with the main shock. It generates low momentum region (by its diffusion inherent characteristics) which is called blockage zone by passing through the adverse pressure gradient due to the main shock [44]. Normally, the blockage zone intends to diffuse further by growing itself. However, it is ceased by the secondary shock-vortex interaction. This time, it becomes stronger downstream due to the secondary shock weaker characteristics. Tip leakage vortex and further weaker downstream tip vortex evaluation from 0.95 span to tip section are presented in Figure 3.31.

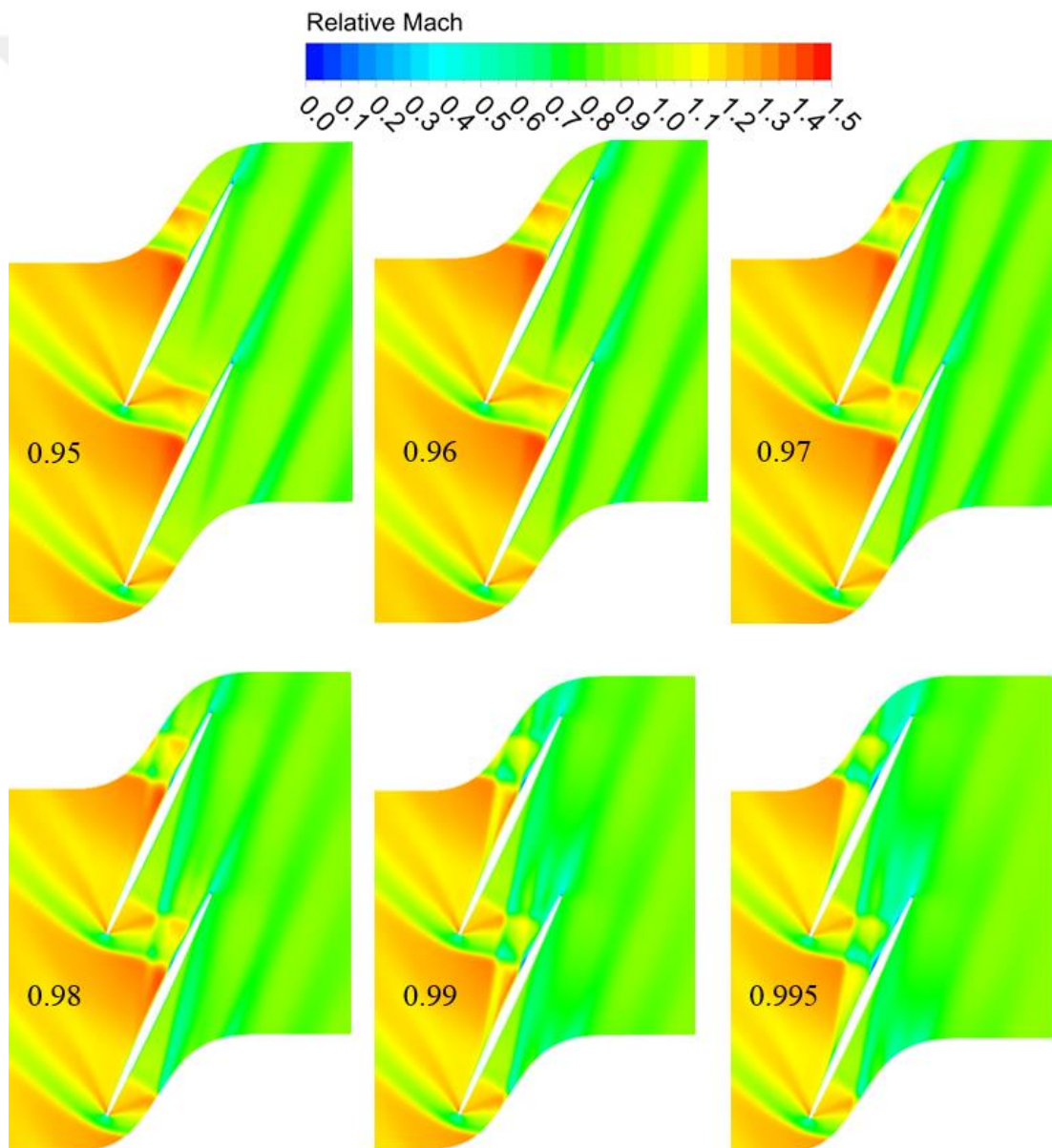


Figure 3.31 : From 0.95 span to 0.995 span tip clearance flow influence.

As approaching the tip section, the tip leakage vortex shows itself more and stronger. The weaker downstream tip leakage vortex is also occurred. Its effect by creating low momentum region close to the trailing edge is clearly visible at 0.99 and 0.995 span regions in Figure 3.31.

Figure 3.30 and 3.31 presented a general information about the tip clearance flow phenomenon. Yet, it is a 3D flow behavior and should be properly investigated. Figure 3.32 demonstrates a typical tip clearance flow occurrence and entropy generation at the blade passages.

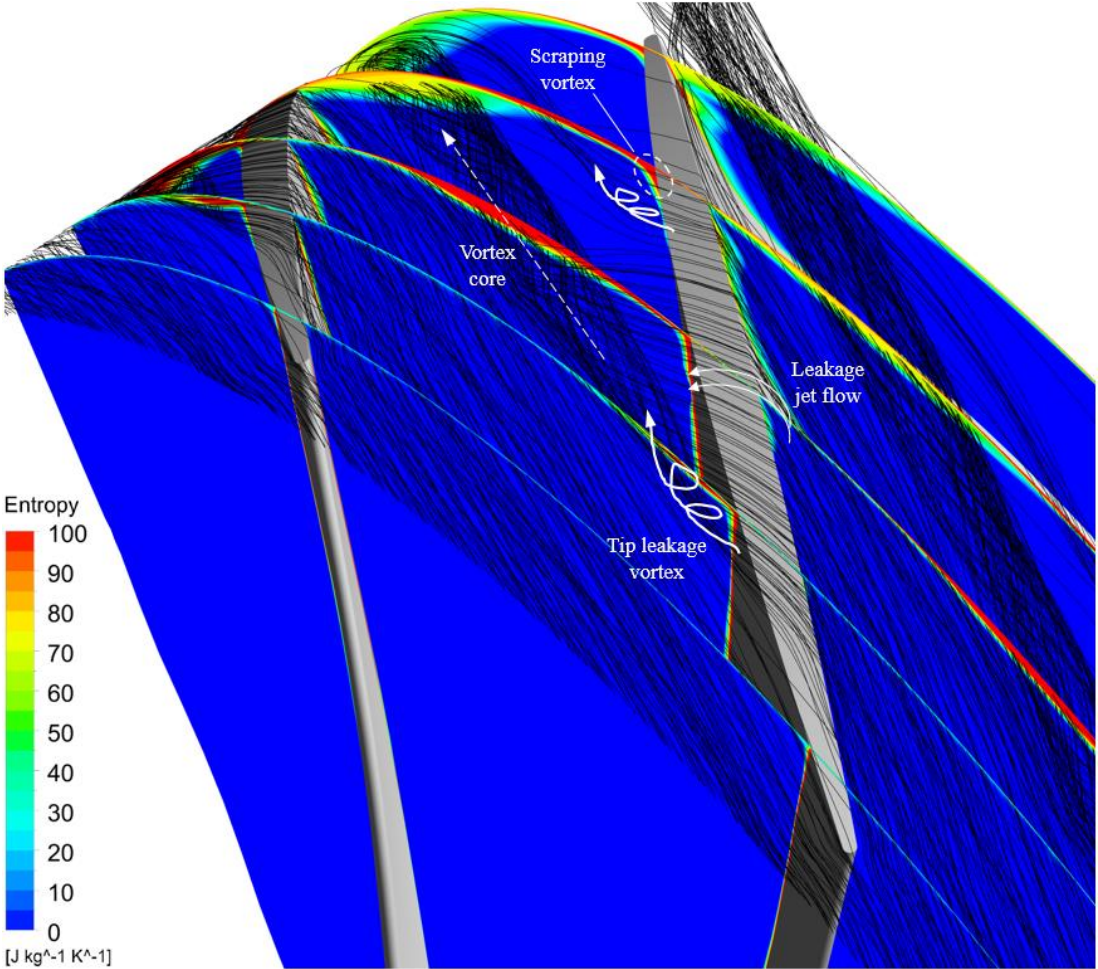


Figure 3.32 : Entropy generation and blade tip flow characteristics (lower and higher values were clipped).

As it is mentioned in Figure 3.30, tip leakage vortex generation happens due to the migration of the flow from pressure side to suction side. Suction side regular flow comes across with tip flow migration and as a results this event creates vorticies. These vorticies grown up and become stronger with the interaction of the leakage jet flow through the passage and forms a tip leakage vortex. White dashed arrow line

shows the vortex core of the tip leakage vortex. It originates the center of the entropy generation zone. The vortex core diffuses and drives its way slightly to the bottom spans and thickens the boundary layer of the entropy further downstream. However, the diffusion makes the vortex less stronger and reduces the entropy generation (see Figure 3.32 near trailing edge). There is also a relatively small entropy generation zone near the suction side blade boundary layer at the tip that is encircled with a white dashed lines. It is possibly occurred due to the scraping vortex formation. Because, the blade rotation is very close to the casing for smaller tip gaps; casing boundary layer is rolled up due to the dominating effect of the blade tip and forms a scraping vortex [45].

In the next section, the discussed fan stage (LPC) influence on the whole engine will be investigated by engine thermodynamics performance simulations.

4. ENGINE PERFORMANCE SIMULATION

In the previous section, aerodynamics investigation of the fan stage was studied detailly. Fan stage influence on the whole engine performance was presented in this section. In another words, thermodynamic matching study was carried out for each core turbojet and whole turbofan system. Their performance results were then compared in order to determine the fan stage influence on the system. At first, the existing core micro-turbojet performance simulation was studied as a reference model. After that, micro-turbofan with additional fan stage was considered. The performed comparison study is based on operating lines, thrust and SFC parameters.

As a core turbojet, AMT Nike micro gas turbine engine was considered. The core compressor (rotor + diffuser) off-design performance map was obtained with the validated solver (see chapter 2.2) of ANSYS CFX 18.2. Core compressor performance maps are presented in Figure 4.1.

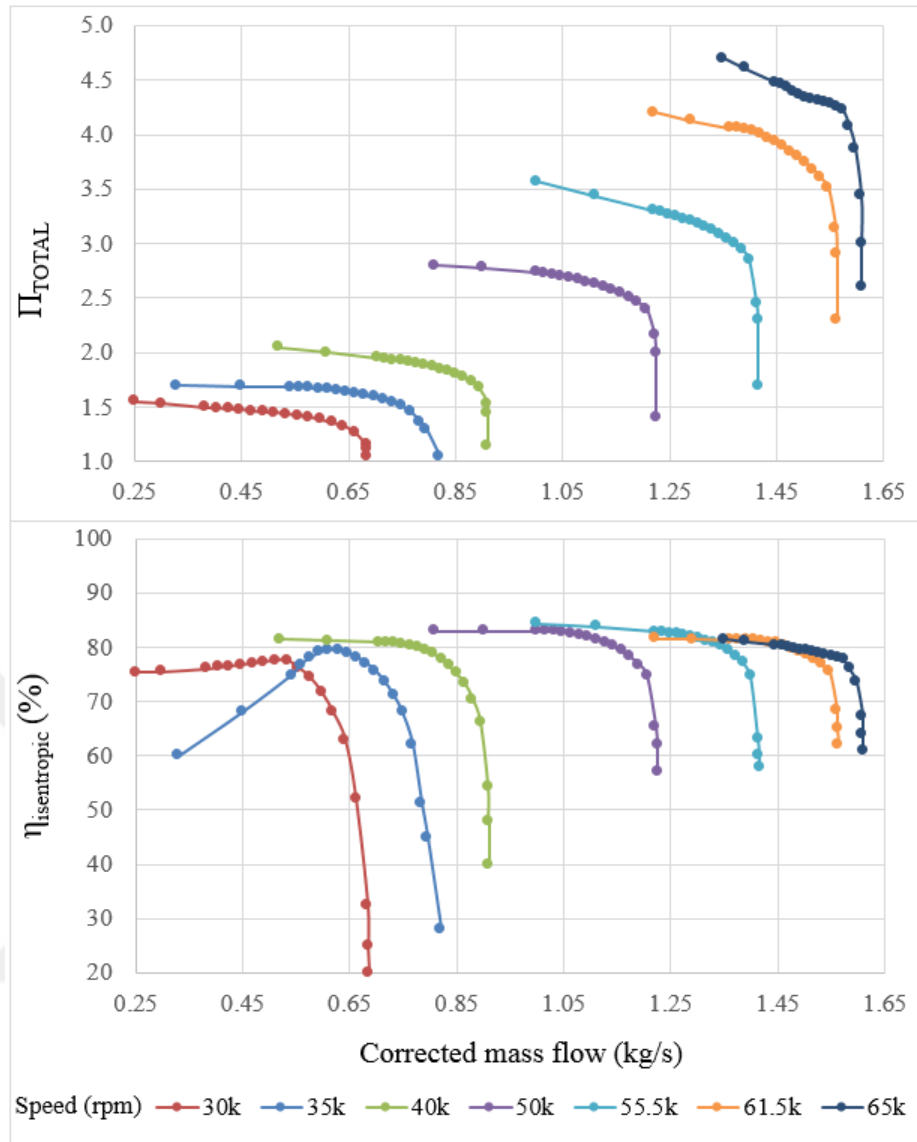


Figure 4.1 : AMT Nike core compressor performance maps.

In Figure 4.1, the performance maps were obtained from 30000 idle rpm to 65000 maximum rpm as rotational speeds. Note that, 61500 rpm is the nominal (design) shaft speed.

As it is mentioned before, turbine off-design performance maps were provided from the collaborative team at Purdue University. Turbine inlet total properties were estimated values (385035 Pa, 1344 K) by the collaborative team. Turbine off-design performance maps are presented in Figure 4.2.

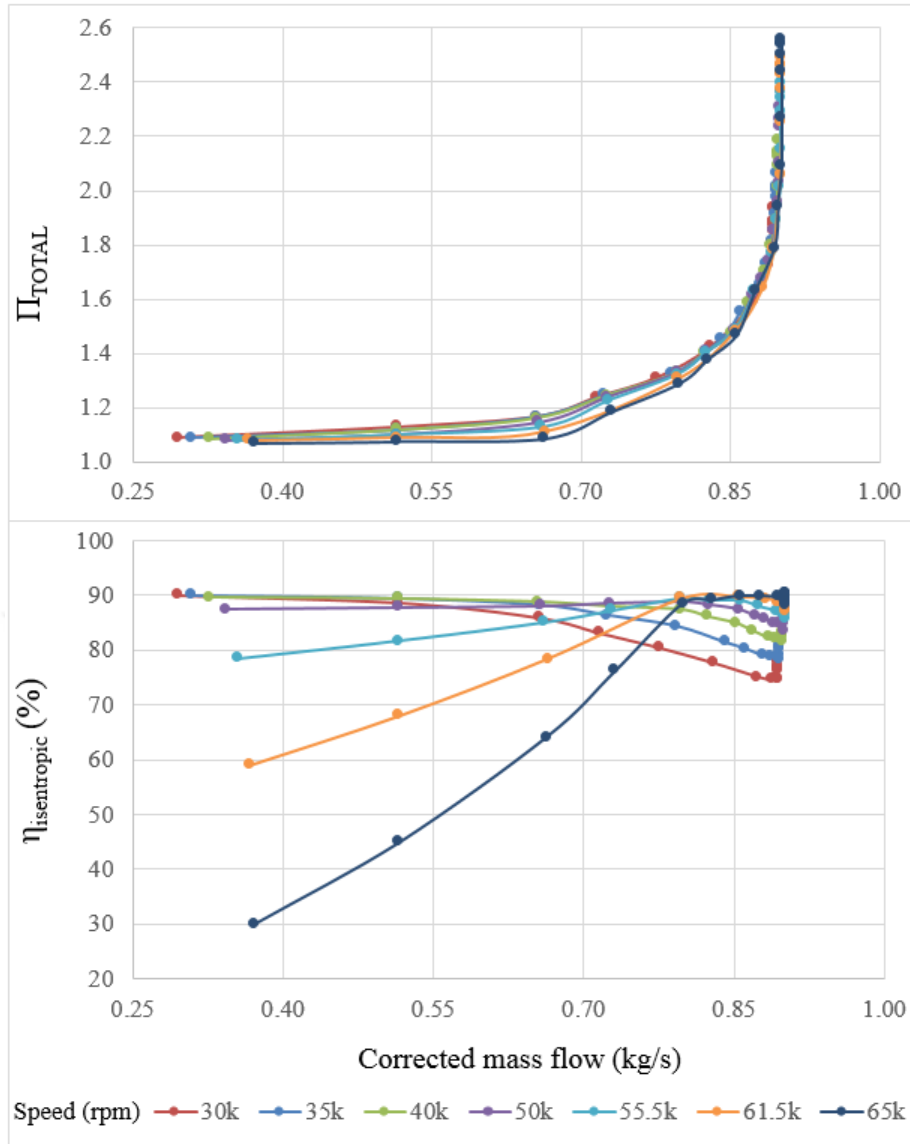


Figure 4.2 : AMT Nike turbine performance maps.

It should be mentioned that mass flow range of both maps are different, since the component maps were obtained separately with different inlet conditions. In addition, mass flow correction was done according to sea-level standards for both components. The corrected mass flows were calculated by;

$$\frac{\dot{m}_C \sqrt{\theta_C}}{\delta_C}, \frac{\dot{m}_T \sqrt{\theta_T}}{\delta_T} \quad (4.1)$$

where the non-dimensional variables were defined as follows;

$$\theta = \frac{T_t}{T_{STP}}, \delta = \frac{P_t}{P_{STP}} \quad (4.2)$$

Here, the subscript STP refers to the standard sea-level temperature and sea-level pressure (~288.15 K and 101325 Pa, respectively). T_t and P_t are the total temperature and total pressure at the inlet stations (see Figure 4.3).

The numerical tool which was used for engine performance simulations, is MATLAB R2018a with an academic license. The input parameters were defined from off-design performance maps into in-house matching code for each component. The outputs were then obtained to make the necessary comparison.

4.1 Core Turbojet Engine Performance Study

4.1.1 Matching of core compressor and turbine

At the beginning of the matching process, engine stations should be determined, as the indices of the stations will be used for input parameters and matching calculations. The core turbojet engine stations are demonstrated in Figure 4.3.

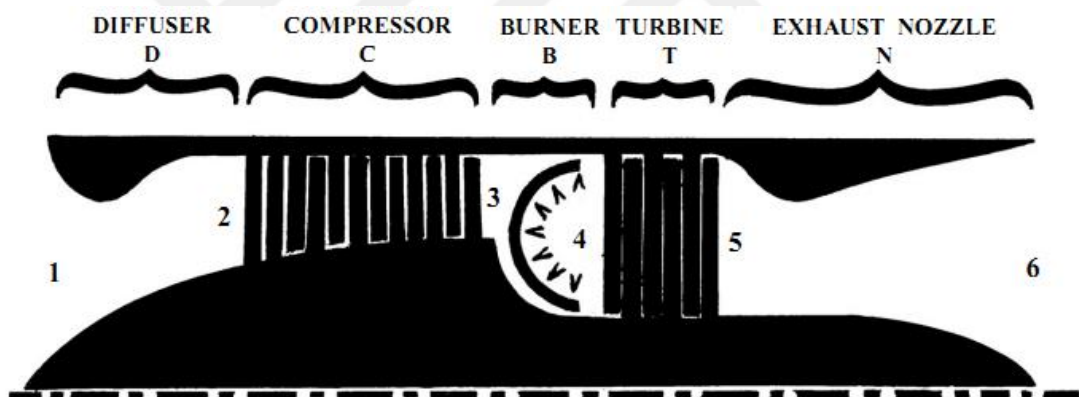


Figure 4.3 : Core turbojet engine sections and its indices [25].

In Figure 4.3, station 1 represents the air inlet of the engine inlet diffuser. Station 2 and 3 represent compressor inlet and outlet, respectively, while station 4 and 5 represent turbine inlet and outlet. Lastly, station 6 represents the exit of the engine exhaust nozzle.

Once, the core compressor and the turbine off-design performance maps are obtained, it has to be ensured that the ensemble will work in the desired situation on the same shaft. The matching process of both components is carried out due to two main balances necessary agreement;

- Mass flow balance

- Energy balance

Since, both components are on the same shaft, the core compressor and the turbine rotational speeds are the same, therefore providing the energy balance. On the other hand, a mass flow balance can be roughly obtained with;

$$\dot{m}_2 = \dot{m}_4 \text{ [kg/s]} \quad (4.3)$$

With the addition of fuel, mass balance can be rewritten;

$$(1+f)*\dot{m}_2 = \dot{m}_4 \quad (4.4)$$

As the sonic speed conditions are reached for the turbine map, the pressure ratio can still increase without any change in the mass flow rate. At this point, all the performance lines for different speeds merge into one single vertical performance line and the diagram can not be distinguishable. To display correctly on the turbine map, mass flow correction is manipulated as;

$$\frac{\dot{m}_4 \sqrt{\theta_T}}{\delta_T} * \frac{N}{\sqrt{\theta_T}} = \frac{\dot{m}_4 N}{\delta_T} \quad (4.5)$$

The second term on the left handside represents the corrected speed of the turbine. Equation 4.4 can be rewritten as;

$$(1+f)* \frac{1}{0.95*C_{pr}} * \frac{\dot{m}_2 N}{\delta_T} = \frac{\dot{m}_4 N}{\delta_T} \quad (4.6)$$

where the term $0.95*C_{pr}$ represents the ratio of turbine inlet total pressure (P_{t4}) to compressor inlet total pressure (P_{t2}). It was expressed indirectly by using C_{pr} (compressore pressure ratio). Here, pressure drop of the combustion chamber was assumed as 5% of the total pressure.

The next step is the matching of powers between two components. For the matching purposes, pressure ratio is not well suited. As a first approach, it is assumed that turbine power will be used only to drive the core compressor. Entalpy change for two components will then be identical ($P_{total} = \dot{m} * \Delta H$). Therefore, entalpy change instead pressure ratio is well suited for matching purposes. By using total entalpy change, non-dimensional specific work can be derived as follows;

$$\frac{\Delta H}{RT_t} \quad (4.7)$$

By assuming the same operating gas for a given geometry, the diameter and the gas constant parameters can then be eliminated;

$$\frac{\Delta H}{T_t} \quad (4.8)$$

Off-design maps were obtained and corrected to standard atmospheric (sea-level) conditions. By using the non-dimensional parameter of temperature (θ) from Equation 4.2, one can obtain;

$$\frac{\Delta H}{\theta} \quad (4.9)$$

As taking into account the turbine enthalpy change, the similar corrected turbine speed manipulation from Equation 4.5 can be applied as;

$$\frac{\Delta H_T}{\theta_T} * \frac{\theta_T}{N^2} = \frac{\Delta H_T}{N^2} \quad (4.10)$$

As both components rotate on the same shaft, power output of the turbine is absorbed by the core compressor;

$$\frac{\Delta H_C}{(1+f)N^2} = \frac{\Delta H_T}{N^2} \quad (4.11)$$

Lastly, although core compressor and turbine have the same mechanical speed, they do not have the same non-dimensional speed. A coefficient will be used on one of the speeds so as to be compatible with the one another;

$$\sqrt{\frac{T_{t2}}{T_{t4}}} * \frac{N}{\sqrt{\theta_C}} = \frac{N}{\sqrt{\theta_T}} \quad (4.12)$$

Once the matching steps are applied for both component maps on the in-house matching code, the maps are superimposed directly. The superimposition of the corrected maps provide one crossing point for each corresponding performance line

which presents the operating point at this condition. The corresponding pressure ratio and efficiency at this specific operating point are determined from both core compressor and turbine maps. Physical mass flow values are obtained by inversed calculation. The physical mass flow results are then recorrected into standart sea-level conditions, since performance maps are sea-level corrected. Each operating points are added into performance maps. Then they are linked one another and create operating line of the engine. The operating line of the turbojet engine is demonstrated on the core compressor and the turbine maps in Figure 4.4.

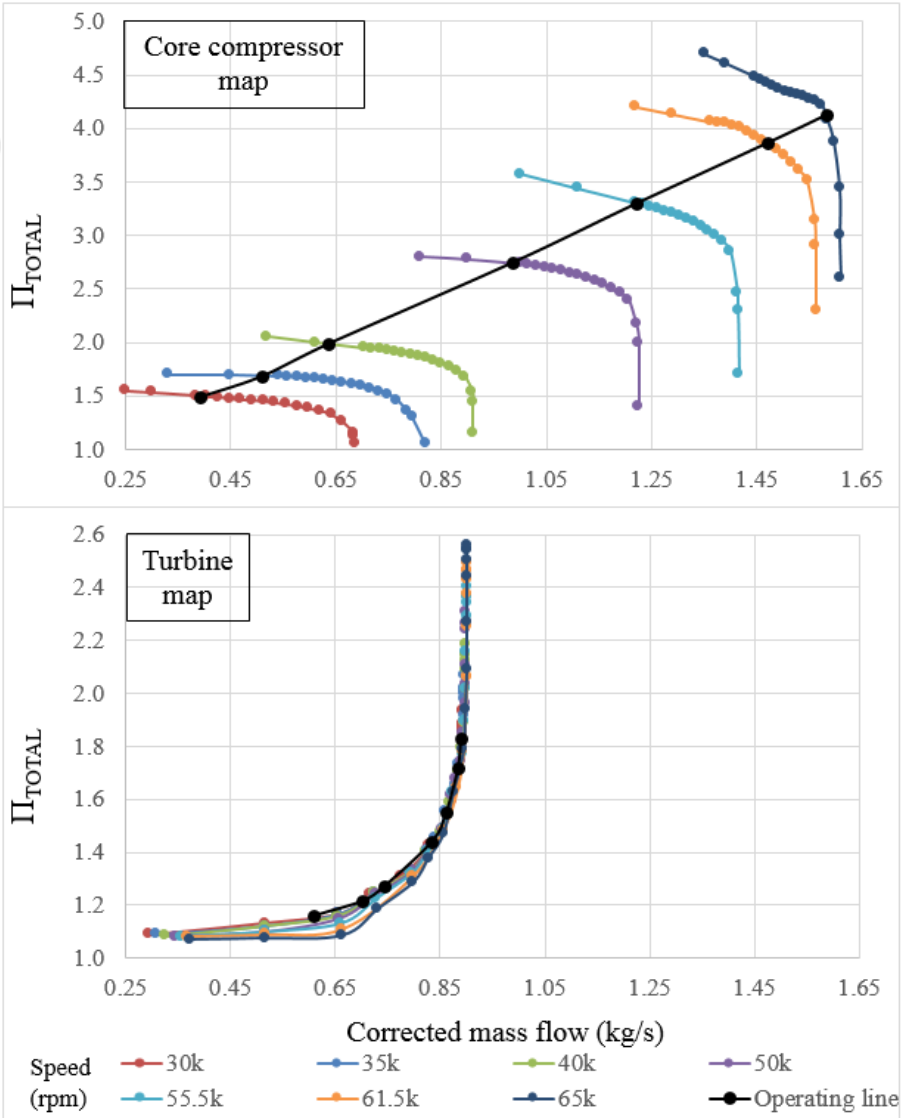


Figure 4.4 : Turbojet engine operating line on each performance maps.

As it is seen from the figure, the core compressor operates near-stall condition at the lower rotating speeds as it is matched with the turbine. Between nominal (61500 rpm) and maximum speed, the compressor operating condition slides from design

point to near-choke condition. The similar characteristic can be observed for the turbine. However, it is a normal characteristic for such a turbojet engine system.

4.1.2 Turbojet engine performance simulations

Engine performance simulations were carried out with respect to engine thrust and SFC parameters. The station 1 and 6 have the ambient atmospheric conditions changing depends on altitude. To obtain total properties of the engine inlet duct, one should find the flight speed. Before that the speed of sound at this specific condition is necessary;

$$a_1 = \sqrt{\gamma_{\text{cold}} * R * T_{s1}} \quad (4.13)$$

where T_{s1} is the static (ambient) temperature depends on altitude. γ_{cold} is the specific heat ratio of the air and R is the gas constant. Flight speed can be obtained for various Mach numbers as follows;

$$V_{\text{flight}} = V_1 = M * a_1 \quad (4.14)$$

Stagnation or total temperature of station 1 can be obtained by sum of the static and dynamic temperatures at this station;

$$T_{t1} = T_{s1} + \frac{V_1^2}{2 * c_{p,\text{cold}}} \quad (4.15)$$

where $c_{p,\text{cold}}$ is the constant-pressure heat capacity. Total pressure at station 1 can then be calculated by isentropic total-to-static formula;

$$P_{t1} = P_{s1} * \left(\frac{T_{t1}}{T_{s1}} \right)^{\frac{\gamma_{\text{cold}}}{\gamma_{\text{cold}} - 1}} \quad (4.16)$$

For the compressor inlet where is the station 2, the inlet duct losses were considered. These losses were roughly accepted as 2% of the total properties. Thus, total pressure at station 2 is found as follows;

$$P_{t2} = P_{t1} * 0.98 \quad (4.17)$$

As the air flow reaches station 2, any heat transfer loss occurs across the duct;

$$T_{t2}=T_{t1} \quad (4.18)$$

The compressor exit pressure is found from performance map by using Compressor pressure ratio (C_{pr}) at each operating point;

$$C_{pr} = \frac{P_{t3}}{P_{t2}} \quad (4.19)$$

Turbine Inlet Pressure can be obtained considering the pressure drop at the Combustion Chamber ($P_{loss\ CC}$);

$$P_{t4}=P_{t3}-P_{loss\ CC} \quad (4.20)$$

where pressure drop was estimated as 5% of the total pressure. Ideal compressor exit temperature was calculated from the isentropic compression formula. The addition of compressor efficiency (η_c) gives the real value of the compressor exit temperature;

$$T_{t3}=T_{t2} * \left(1 + \frac{1}{\eta_c} * C_{pr}^{\frac{\gamma_{cold}-1}{\gamma_{cold}}} - 1\right) \quad (4.21)$$

Then fuel mass flow (\dot{m}_{fuel}) can be obtained as follows;

$$\dot{m}_{fuel} = \dot{m}_2 * \left(\frac{c_{p_cold} + c_{p_hot}}{2}\right) * \left(\frac{T_{t4} - T_{t3}}{CF}\right) \quad (4.22)$$

Here; \dot{m}_2 as mentioned before, is the physical value of core compressor mass flow. CF is the calorific value of the fuel (44000 kj/kg). Avarage of constant pressure heat capacities of hot and cold section was assumed in order to calculate fuel mass flow rate. The fuel to air ratio (f);

$$f = \frac{\dot{m}_{fuel}}{\dot{m}_2} \quad (4.23)$$

With the addition of fuel, turbine mass flow rate (\dot{m}_4) can be found as follows;

$$\dot{m}_4 = (1+f) * \dot{m}_2 \quad (4.24)$$

The compressor exit pressure has been found from performance map by using Compressor Pressure Ratio (C_{pr}) at each operating point. Turbine inlet pressure has been already calculated by taking into account the pressure drop from Combustion Chamber. The turbine exit pressure can then be found from the turbine performance map by using Turbine Pressure Ratio (T_{pr}) at each operating point;

$$T_{pr} = \frac{P_{t4}}{P_{t5}} \quad (4.25)$$

Turbine inlet temperature (TET) was considered as 1344 K which was the assumed value to obtain turbine performance maps. The value is a typical maximum temperature of uncooled or moderately cooled turbine stage. Isentropic conditions and the turbine efficiency then determine the turbine exit total temperature;

$$T_{t5} = (T_{t5i} * T_{pr}^{\frac{\gamma_{hot}-1}{\gamma_{hot}}}) - (\eta_{tr} * (T_{t4} - T_{t5})) \quad (4.26)$$

Nozzle-exit total temperature was assumed that no heat loss occurs across the nozzle;

$$T_{t6} = T_{t5} \quad (4.27)$$

The nozzle losses were accepted as 5% of the total properties. Therefore, nozzle-exit total pressure is found as follows;

$$P_{t6} = P_{t5} * 0.95 \quad (4.28)$$

Static pressure of the nozzle is atmospheric ($P_{s6} = P_{s1}$). The static temperature of the nozzle-exit can be calculated by isentropic total-to-static conversion;

$$T_{s6} = \frac{T_{t6}}{\frac{P_{t6}^{\frac{\gamma_{hot}-1}{\gamma_{hot}}}}{P_{s6}^{\frac{\gamma_{hot}-1}{\gamma_{hot}}}}} \quad (4.29)$$

Static temperature gives the engine-exit sonic speed at this condition;

$$a_6 = \sqrt{\gamma_{hot} * R * T_{s6}} \quad (4.30)$$

Engine exit velocity for various Mach numbers can be obtained;

$$V_6 = M \cdot a_6 \quad (4.31)$$

The thrust that is gained by the turbojet engine;

$$F_t = \dot{m}_2 \cdot (1+f) \cdot V_6 - \dot{m}_2 \cdot V_1 \quad (4.32)$$

Specific thrust of the engine;

$$F_t / \dot{m}_2 = (1+f) \cdot V_6 - V_1 \quad (4.33)$$

Lastly, specific fuel consumption (SFC) can be obtained by using the specific thrust as follows;

$$SFC = \frac{f}{F_t / \dot{m}_2} \quad (4.34)$$

Before performing the engine performance simulations, the validation study of AMT Nike Engine was presented. Technical specifications of the engine were taken from the company's webpage and compared to simulation results. The comparison is shown in Table 4.1.

Table 4.1 : Comparison of engine technical specifications and simulation results.

	AMT Nike Technical Sheet	Engine Simulation Results
Thrust at design RPM at S.T.P.	784 N	973 N
Design RPM	61500	61500
C _{pr} at design RPM (Core compressor)	4 : 1	3.67 : 1
Mass flow	1250 Gr/sec	1488 Gr/sec
Maximum E.G.T.	1148 K	1196 K
Fuel consumption	1900 Gr/min	1860 Gr/min
Specific fuel consumption	40.36 Gr/(Kn*sec)	31.87 Gr/(Kn*sec)

Both parameters were obtained for S.T.P. (Standart sea level temperature and pressure). In addition, thrust and SFC values are uninstalled results which represent

the ground test performance. In Table 4.1, simulation results are slightly different from the technical sheet. The main difference is the assumed Turbine Inlet Temperature (TET) for the simulations. The value of 1344 K that is the turbine off-design assumption was also considered for engine simulations. As a result, the thrust has higher and the specific fuel consumption has lower value for simulation results. And the Exit Gas Temperature (E.G.T.) slightly differs from the existing data. The pressure ratio of 4:1 at the technical sheet is an approximation and it is not accurate. The mass flow result difference reason is the mismeasurement technique of the AMT Netherlands Company. Therefore, the simulation result is more accurate than the technical sheet. Except these differences, the simulation results are reasonable and validates the methodology.

4.2 Adaptive Turbofan Engine Performance Study

4.2.1 Matching of fan and core compressor to turbine

The matching process of turbofan engine is as almost similar as turbojet matching, and there is only one main difference. In turbojet, it was assumed that the turbine only drives the core compressor. However, in turbofan engine, the turbine drives core compressor and provides power for auxiliary elements as well. This power was assumed as the necessary fan power to drive the component. Therefore, it only differs from turbojet matching calculations by Equation 4.10 reorganization. Addition of power for auxiliary elements the Equation 4.10 changes as follows;

$$\frac{1}{(1+f)N^2} * (\Delta H_C + \frac{P}{\dot{m}_c}) = \frac{\Delta H_T}{N^2} \quad (4.35)$$

where power division by mass flow term represents the fan total entalpy. The total entalpy of the fan is the sum of core and bypass section entalpies. As a result, Equation 4.35 can be rewritten as;

$$\frac{1}{(1+f)N^2} * (\Delta H_C + \Delta H_{Fan\ core} + \frac{\dot{m}_{bypass}}{\dot{m}_{core}} * \Delta H_{Fan\ bypass}) = \frac{\Delta H_T}{N^2} \quad (4.36)$$

Total bypass entalpy (the third entalpy term in the paranthesis) is found by multiplication of bypass ratio. Therefore, bypass mass flow divided by core mass flow gives the bypass ratio (See Equation 4.36).

Once the matching steps of turbofan are applied for all component maps on the in-house matching code, the rest of the process is the same as mentioned in turbojet matching part. The operating line of the turbofan engine was obtained with the allowed maximum bypass ratio of 0.7. Since, the some of the performance lines were not matching as exceeding this value. It indicates that the turbine forces its limits and drives both core compressor and fan with a maximum bypass ratio of 0.7. The operating lines of turbojet engine and turbofan engine with 0.7 bypass ratio are demonstrated on the core compressor and the turbine maps in Figure 4.5.

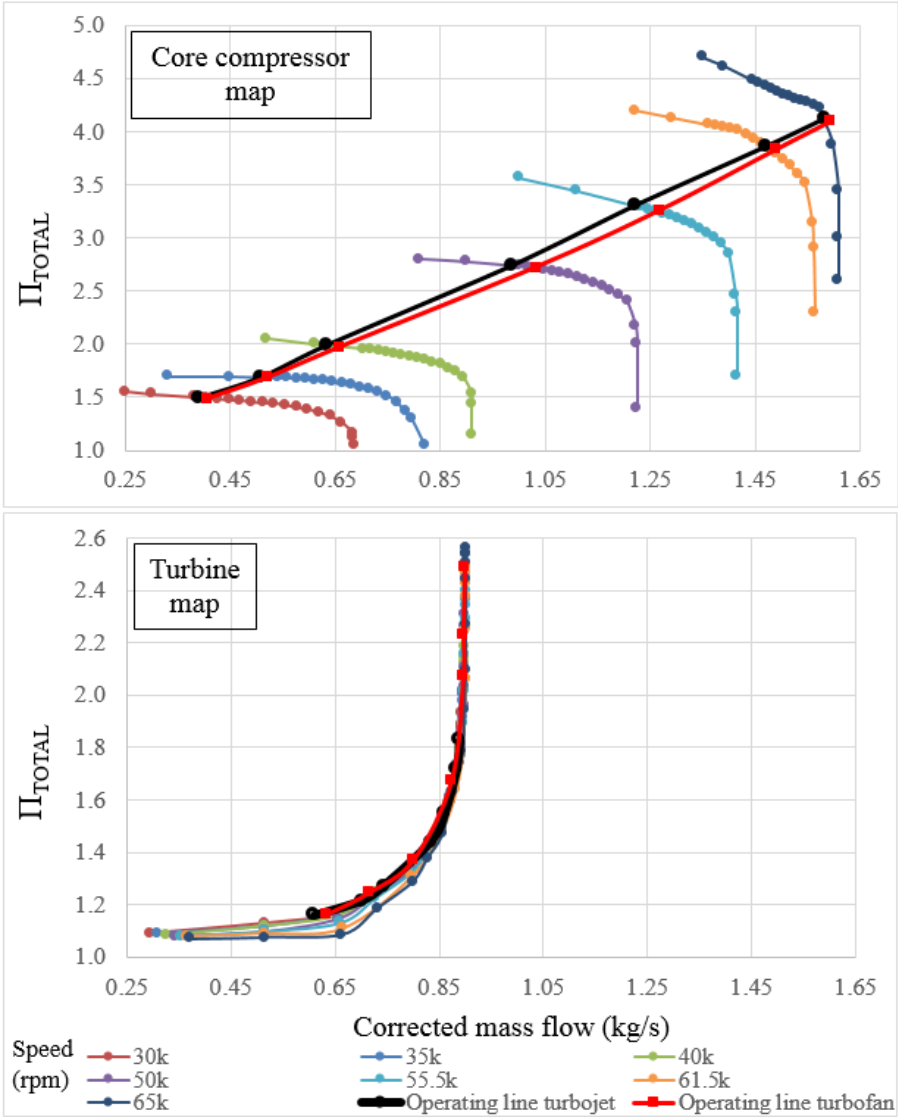


Figure 4.5 : Turbojet and turbofan engine operating lines across each performance maps.

As it is seen, addition of fan to the system forces both core compressor and turbine more than as it was in the turbojet. This is more obvious in the turbine map. At higher rotational speeds such as 55500, 61500 and 65000 rpms, the turbine works at choke condition. However, the results are expected for such an adapted turbofan structure over a turbojet engine.

It was already mentioned that the adaptive turbofan engine has a Continuously Variable Transmission (CVT) system. Considering this, the gear ratio between fan and core compressor varies across different operating speeds. It is 2:1 for 55500, 61500 (design speed) and 65000 rpms. Lower speeds, the gear ratio becomes larger. It is 2.5:1 at 50000 rpm, 4:1 at 40000 rpm, 4.66:1 at 35000 rpm and lastly 6:1 at the idle rotation of 30000 rpm. These gear ratios are the most efficient ones for each operation. As a result, CVT structure shows its positive functionality on the turbofan engine and therefore it provides infinite operating options for the engine concept.

4.2.2 Turbofan engine performance simulations

Engine performance simulations were carried out following the similar principle as it was performed in turbojet engine. The stations which were represented for turbojet is the same, except some differences. The upstream flow of the fan was named as station 0. This time station 1 represents the fan inlet region. Station 2 represents not only the compressor upstream flow but also the LPC stator downstream. The turbofan engine stations are represented by Figure 4.6.

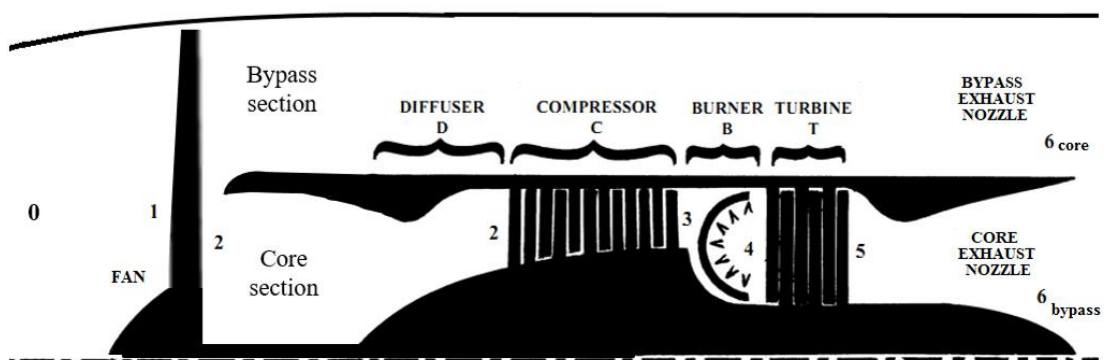


Figure 4.6 : Turbofan engine sections and its indices [25].

To obtain total properties at the fan inlet duct, one should find the flight speed. Before that the speed of sound at the specific condition is necessary;

$$a_0 = \sqrt{\gamma_{\text{cold}} * R * T_{s0}} \quad (4.37)$$

The flight speed for various Mach numbers by using the speed of sound;

$$V_{\text{flight}} = V_0 = M * a_0 \quad (4.38)$$

Total (stagnation) temperature of the upstream flow of the fan (station 0) can be obtained as follows;

$$T_{t0} = T_{s0} + \frac{V_0^2}{2 * c_{p_cold}} \quad (4.39)$$

Total pressure at station 0 can be found by isentropic total-to-static relation;

$$P_{t0} = P_{s0} * \left(\frac{T_{t0}}{T_{s0}} \right)^{\frac{\gamma_{\text{cold}}}{\gamma_{\text{cold}} - 1}} \quad (4.40)$$

At the fan inlet (Station 1), the intake duct losses are considered. These losses are assumed as 2% of the total properties. Total pressure at the fan inlet is therefore;

$$P_{t1} = P_{t0} * 0.98 \quad (4.41)$$

There is no heat transfer loss across the intake duct;

$$T_{t1} = T_{t0} \quad (4.42)$$

Fan core duct exit total pressure is found by using fan pressure ratio at core section ($F_{\text{pr_core}}$) at each operating point;

$$F_{\text{pr_core}} = \frac{P_{t2}}{P_{t1}} \quad (4.43)$$

By accounting the efficiency of the fan core section ($\eta_{\text{fan_core}}$), one can find the fan exit temperature as follows;

$$T_{t2} = T_{t1} * \left(1 + \frac{1}{\eta_{\text{fan_core}}} * F_{\text{pr_core}}^{\frac{\gamma_{\text{cold}} - 1}{\gamma_{\text{cold}}}} - 1 \right) \quad (4.44)$$

Similarly, core compressor exit pressure is found by using Compressor pressure ratio (C_{pr}) at each operating point;

$$C_{pr} = \frac{P_{t3}}{P_{t2}} \quad (4.45)$$

Using the core compressor efficiency (η_c), the real value of the compressor exit temperature can be calculated;

$$T_{t3} = T_{t2} * \left(1 + \frac{1}{\eta_c} * C_{pr}^{\frac{\gamma_{cold} - 1}{\gamma_{cold}}} - 1\right) \quad (4.46)$$

Fuel mass flow, fuel-to-air ratio, turbine inlet and exit total properties can be obtained with the same way as used for the turbojet engine. On the other hand, this time there are two exit nozzles. Core nozzle-exit total temperature was assumed that no heat loss occurs across the core nozzle;

$$T_{t6_core} = T_{t5} \quad (4.47)$$

Throughout the core nozzle-exit duct, 5% of total properties are lost. Therefore;

$$P_{t6_core} = P_{t5} * 0.95 \quad (4.48)$$

Static pressure of the core nozzle-exit is atmospheric ($P_{s6_core} = P_{s1}$). Static temperature can then be found as follows;

$$T_{s6_core} = \frac{T_{t6_core}}{\frac{P_{t6_core}}{P_{s6_core}}^{\frac{\gamma_{hot} - 1}{\gamma_{hot}}}} \quad (4.49)$$

Core section engine-exit sonic speed at this condition;

$$a_{6_core} = \sqrt{\gamma_{hot} * R * T_{s6}} \quad (4.50)$$

Core section engine-exit velocity for various Mach numbers;

$$V_{6_core} = M * a_{6_core} \quad (4.51)$$

The thrust gained from the core section flow;

$$F_{t_core} = \dot{m}_2 * (1+f) * V_{6_core} - \dot{m}_2 * V_0 \quad (4.52)$$

Next, bypass nozzle total properties and engine-exit velocity should be found. In this direction, bypass duct exit total pressure can be obtained by considering the Fan bypass pressure ratio (F_{pr_bypass}). In addition, bypass duct losses were accepted as 5% of the total properties. As a result bypass nozzle exit total pressure can be obtained as follows;

$$P_{t6_bypass} = 0.95 * F_{pr_bypass} * P_{t0} \quad (4.53)$$

Static pressure at the bypass nozzle exit is atmospheric ($P_{s6_bypass} = P_{t0}$). Total temperature at the bypass duct exit (T_{t6_bypass}) can be found from the total bypass enthalpy which was used in turbofan matching. Bypass nozzle-exit static temperature is found similar to core section;

$$T_{s6_bypass} = \frac{T_{t6_bypass}}{\frac{P_{t6_bypass}^{\frac{\gamma_{cold}-1}{\gamma_{cold}}}}{P_{s6_bypass}^{\frac{\gamma_{cold}-1}{\gamma_{cold}}}}} \quad (4.54)$$

Bypass section engine-exit sonic speed at this condition;

$$a_{6_bypass} = \sqrt{\gamma_{cold} * R * T_{s6_bypass}} \quad (4.55)$$

Bypass section engine-exit velocity for various Mach number values;

$$V_{6_bypass} = M * a_{6_bypass} \quad (4.56)$$

The thrust that is gained from the bypass flow;

$$F_{t_bypass} = BPR * (\dot{m}_2 * V_{6_bypass} - \dot{m}_2 * V_0) \quad (4.57)$$

where BPR is the bypass ratio. As mentioned before, the allowed maximum BPR is 0.7 in this simulation conditions. As a result, the sum of core and bypass section thrust gives the total thrust gained by the turbofan engine;

$$F_{\text{total}} = F_{\text{t_core}} * F_{\text{t_bypass}} \quad (4.58)$$

The specific thrust of the engine is;

$$\frac{F_{\text{total}}}{\dot{m}_2} \quad (4.59)$$

Finally, specific fuel consumption (SFC) of the turbofan engine can be found as follows;

$$\text{SFC} = \frac{f}{F_{\text{total}}/\dot{m}_2} \quad (4.60)$$

The performance comparison of turbojet and adaptive turbofan engine for S.T.P. (stationary ground condition) at design speed is demonstrated in Table 4.2.

Table 4.2 : Comparison of turbojet and adaptive turbofan at S.T.P. condition.

	Engine Simulation Results (Turbojet)	Engine Simulation Results (Turbofan)	
Thrust at design RPM at S.T.P.	973 N	1998 N	
Design RPM	61500	61500	
Cpr at design RPM (Core compressor)	3.86 : 1	3.84 : 1	
Mass flow	1488 Gr/sec	core 2254 Gr/sec	bypass 1578 Gr/sec
Maximum T.E.T.	1344 K	1344 K	
Fuel consumption	1860 Gr/min	2532 Gr/min	
Specific fuel consumption	31.87 Gr/(Kn*sec)	21.12 Gr/(Kn*sec)	

As it is seen from Table 4.2, total thrust (uninstalled) of the turbofan engine with a bypass ratio of 0.7 doubles the reference turbojet model. The Low pressure compressor in other saying ‘the fan stage’ shows its obvious positive functionality on the system. With the addition of fan stage also allows the system to suck much more air into the core section. As a result, air mass flow dramatically increases at the rate of 50% (from 1488 gr/sec to 2254 gr/sec). Although, fuel mass flow increases

correspondingly, SFC (uninstalled) value of the turbofan engine over reference turbojet reduces around 33%. Apart from the comparison of S.T.P. ground engine simulations, both engines were also compared at a specific altitude of 10000 m for the compressor design speed. The altitude level was determined by considering the operating altitudes of equivalent Medium-altitude long endurance (MALE) UAV applications. The simulation results are presented in Table 4.3 for different Mach values.

Table 4.3 : Reference turbojet and adaptive turbofan performance comparison at 10000 m altitude.

61500 rpm @ 10000 m altitude	Turbojet					Turbofan				
Mach	0.2	0.4	0.6	0.8	1.0	0.2	0.4	0.6	0.8	1.0
Thrust (N)	101	202	302	403	503	148	296	444	592	738
Thrust uninstalled (N)	190	380	570	759	948	378	755	1133	1510	1886
SFC [Gr/(Kn*sec)]	342.2	169.7	111.6	82.0	63.9	327.4	162.0	106.1	77.5	59.9
SFC uninstalled [Gr/(Kn*sec)]	181.6	90.0	59.2	43.5	33.9	128.5	85.3	41.6	30.4	23.5

In Table 4.3, turbofan engine concept also shows its superiority over turbojet at 10000 m altitude. Comparing to ground performance, similar trends are observed at this specific altitude as well. Uninstalled total thrust almost doubles with the addition of fan stage and normal thrust increases almost at the rate of 50% for different operations. Uninstalled SFC which is the valid measure of SFC reduces around 30% for variable Mach values.

In conclusion, as it is expected, LPC system provides greater thermodynamic performance results both for total thrust and SFC parameters. The results also show the feasibility of the turbofan structure on the micro-scaled UAV engine applications.

The next chapter will investigate the reliability study of the fan rotor by considering its structural integrity and vibrational behavior.

5. AEROMECHANICAL INVESTIGATION OF THE FAN BLADE

The reliability of turbomachinery is crucial and should satisfy that the rotating components work in a safe condition. This section takes into account the structural integrity and vibrational behavior of the fan rotor blade. In other words, the aeromechanical investigation of the rotor blade was carried out considering both steady and unsteady effects. The simulations were performed in ANSYS Mechanical. The flow chart of the aeromechanical study is illustrated in Figure 5.1.

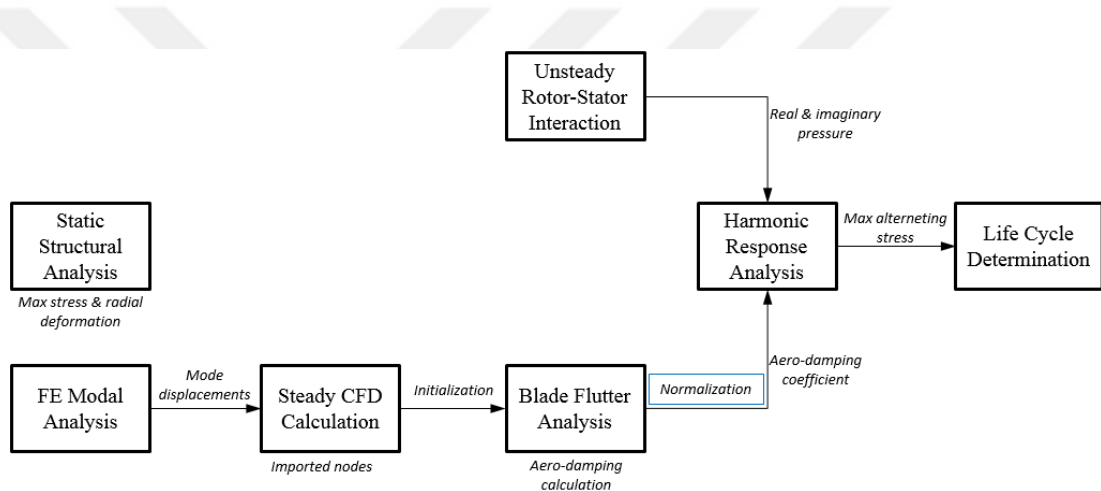


Figure 5.1 : Aeromechanical study flow chart.

5.1 Static Structural Simulations

Static Structural finite element analysis was carried out to observe steady stress levels of the rotor blade. The selected material was Titanium Alloy (Ti6A14V ELI). This material was chosen due to high stress levels occurrence as a result of such a highly-twisted design and it is commonly used material in aviation industry especially for turbomachinery because of its light weight, corrosion resistance, and high strength (the yield stress is 930 MPa and the ultimate tensile strength is 970 MPa). A bladed-disc (blisk) which is intended in production stage as well, was designed with a 4-mm-radius hub fillet same as the CFD simulations. The computational domain is a periodic section (1 of the 11 rotor blades). The determined boundary conditions are fixed support at the arm of the blisk (surface A) and rotation

of the blisk. The computational domain and boundary conditions of the periodic blisk geometry are shown in Figure 5.2.

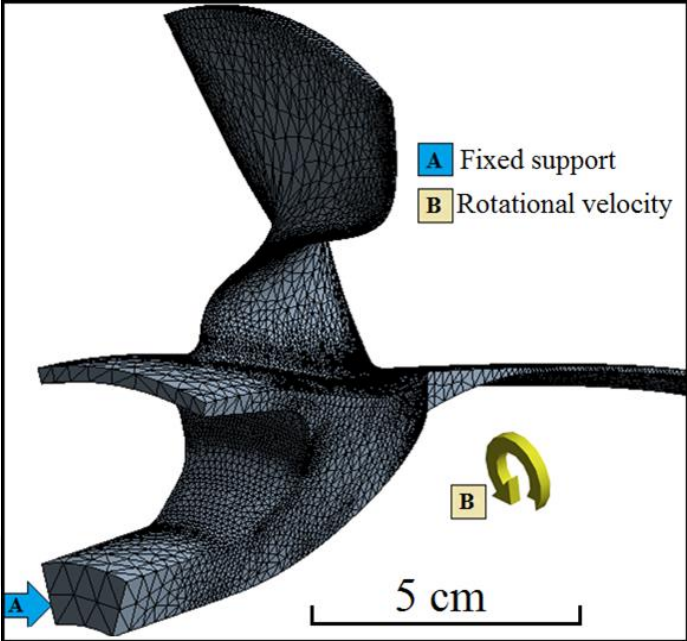


Figure 5.2 : Rotor blisk design, computational domain and boundary conditions.

The analyses were carried out in nominal speed (29000 rpm) and maximum speed (35000 rpm) operations. The results are presented in Figure 5.3.

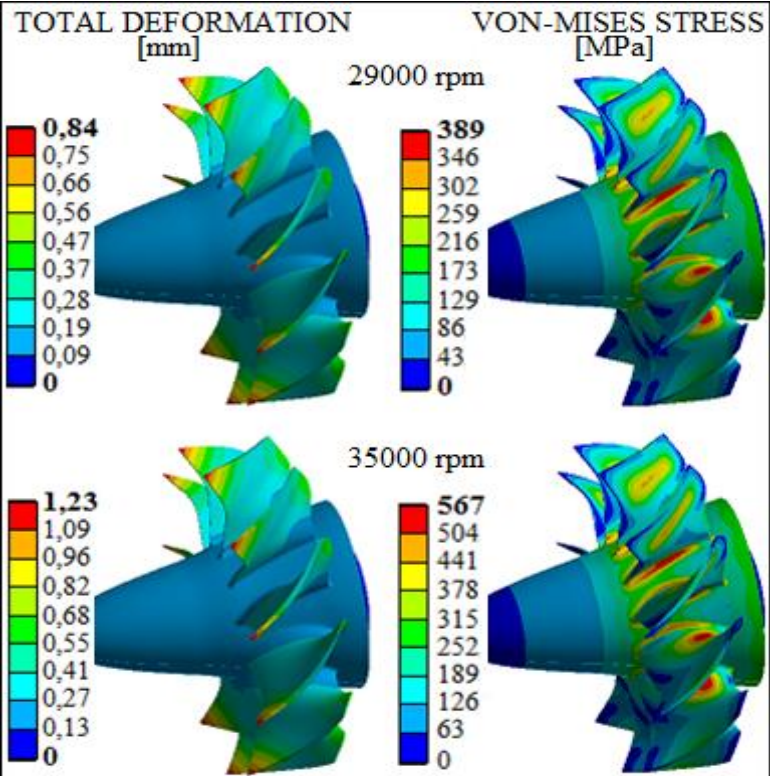


Figure 5.3 : Total deformation and max equivalent Von-misses stress.

Considering the maximum speed (35000 rpm) results, the maximum stress is 567 MPa at the blade root. Even in maximum speed the safety factor of the blade is 1.6. This result is achieved by designing rather thick blade profiles. The radial deformation which is originated from centrifugal force is 0.30 mm at the nominal speed (29000 rpm) and 0.44 mm at the maximum speed (35000 rpm). To achieve the targeted tip gap value (0.25 mm), blades should be manufactured shorter. In conclusion, the results are in acceptable levels. Next part will examine the vibrational and unsteady behavior of the rotor blade.

5.2 Finite Element Modal Analysis

Modal analysis of the fan blade was carried out to find the natural frequencies of the structure. The resonance point of natural frequencies were determined via Campbell Diagram. These resonance points were the result of each blade natural frequency and excitation speedline interaction on the Campbell Diagram. There are 11 rotors and 20 stators. The excitation speedlines are $11 \cdot \text{EO}$ (Engine Order) from self excitation of the rotor, $20 - 11 = 9 \cdot \text{EO}$ from phase lag between rotor and downstream stator and $20 \cdot \text{EO}$ from downstream stator excitation. Although, stators are one-chord downstream away from the rotor, the most critical and the highest one which is the stator excitation on the rotor was determined as the speedline ($20 \cdot \text{EO}$) in the diagram. In the Campbell Diagram, 7 natural frequencies of the rotor are crossing with the speedline of $20 \cdot \text{EO}$ and have a potential to create resonance on rotor blade. The Campbell Diagram and resonance points of the rotor blade are shown in Figure 5.4.

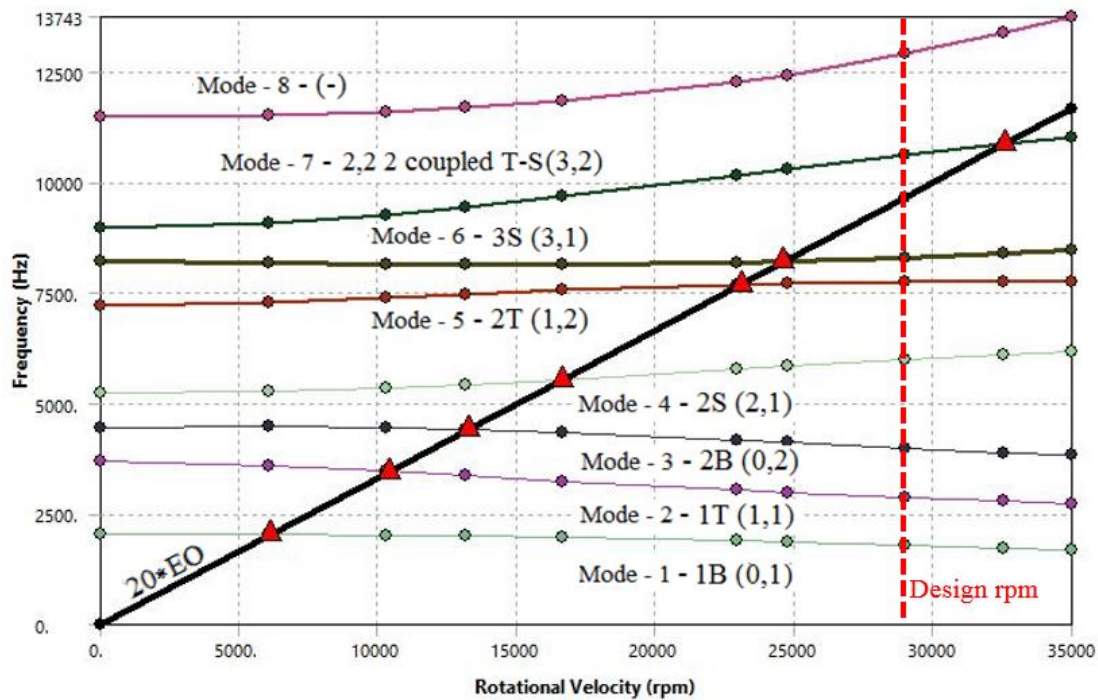


Figure 5.4 : Campbell Diagram of the fan rotor.

In Figure 5.4, these mode shapes are;

- *1B, 2B*: First&Second Bending
- *1T, 2T*: First&Second Torsion
- *2S, 3S*: Second&Third Chordwise Bending
- *2, 2 2 coupled T-S*: Coupled Torsion and Chordwise Bending

The analysis are simulated with a blade only model rather than blisk itself. Since, blade with the other instruments (nosecone, root body etc.) consist of many modes. And the blisk model creates confusion, since the obtained modes (natural frequencies) contribute to flutter on rotor blade or contribute to flutter on the other instruments. The crossing mode shapes indicating resonance in the Campbell Diagram are demonstrated with blade only model in Figure 5.5.

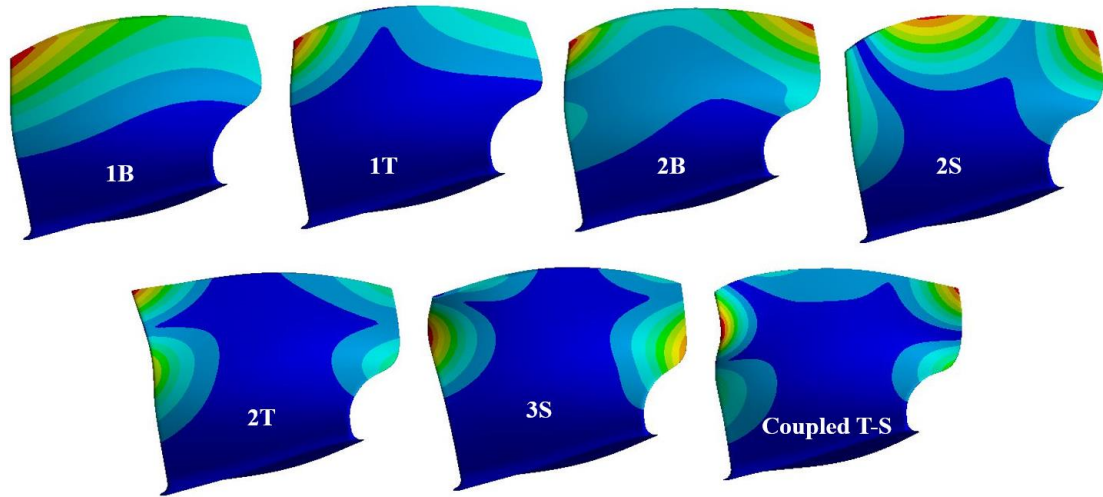


Figure 5.5 : Resonanced mode shapes.

These resonance points are around 6000, 11000, 14000, 17000, 23000, 25000 and 33000 rpms (see Figure 5.4). At the design speed, there is no resonance potential. Each vibrating mode shape of the rotor blade will be investigated to provide the complete reliability of the structure. However, in this study only one of the most critical modes (6th mode) which is at 25000 rpm, was studied.

5.3 Aerodynamic Damping Calculation

Aerodynamic damping was calculated by Fourier Transformation Blade Flutter Analysis [32] with deformed mesh in ANSYS CFX 18.2. This method solves flow over vibrating blades with prescribed modeshape blade displacements. In this direction, 6th vibrating mode shape deformation values were imposed into ANSYS CFX as nodes. Then the nodes were expanded into a full model as shown in Figure 5.6. It is important to note that in CFX, Steady Rotor-Stator analysis was done in advance to be used as initialization for Fourier Transformation Blade Flutter Analysis. Since, this method demands steady CFD analysis in order to initiate the solution.

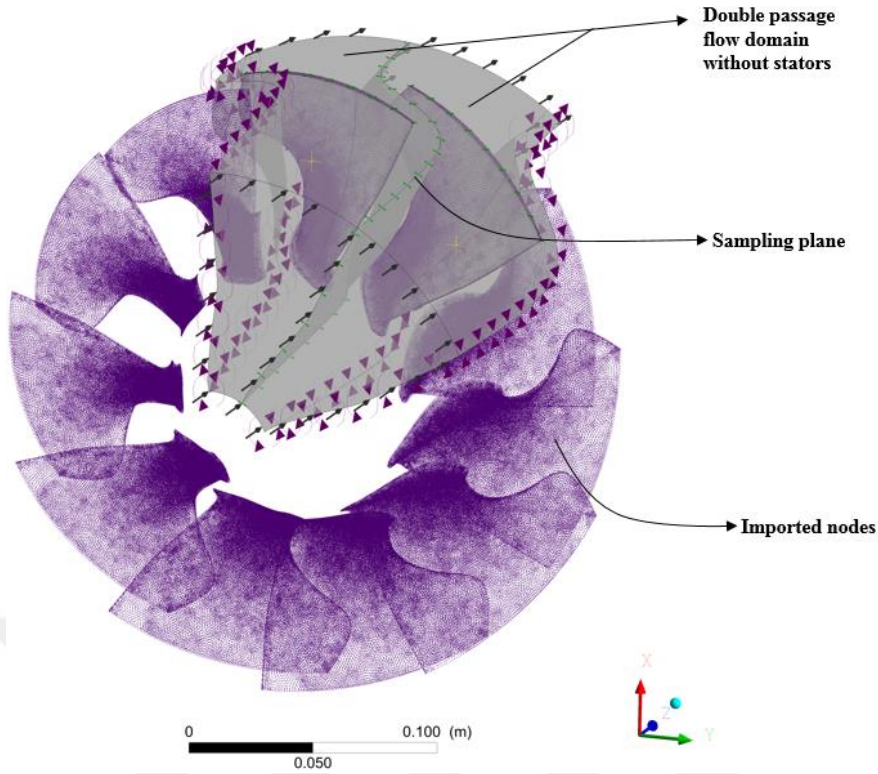


Figure 5.6 : Imported nodes of the specific mode.

Seen in Figure 5.6, Double Passage Method which uses internal interface, converges very rapidly comparing to single passage model. Internal interface called as Sampling Plane where is between blade passages, collects the fluid properties with high accuracy and then transfers data back to the periodic boundaries with a suitable phase lag [32]. On the other hand, this method does not consider rotor-stator interaction. Therefore stator was not included in the computational domain. Rotor-stator interaction will later be considered in cold geometry with transient analysis.

In order to carry out blade flutter calculations, it is crucial to consider aerodynamic effects between neighbouring blades. For a blisk structure consisting of finite number of blades (N_{BL}), there is a limited number of nodal diameters (ND) and therefore corresponding Inter Blade Phase Angles (IBPA) between neighbouring blades. IBPA is calculated as follows [46];

$$IBPA = \frac{2\pi ND}{N_{BL}} \quad (5.1)$$

where ND is

- $0 \leq ND \leq N_{BL} / 2$ for even number of blades
- $0 \leq ND \leq (N_{BL} - 1) / 2$ for odd number of blades

To find out the most critical aerodynamic damping value for Harmonic Response Analysis, all IBPAs should be considered. As a result; $(11-1)/2=5$ Nodal Diameters which are 1, 2, 3, 4, 5 corresponding to IBPAs of 0,57 , 1,14 , 1,71 , 2,28 , 2,85 radians, were analyzed with their negative counterparts. Totally 10 IBPAs were obtained.

Blade flutter analysis obtains the aerodynamic damping as a work per vibration cycle which has the unit of energy (joule). However, Harmonic Response Analysis requires aerodynamic damping coefficient which is a normalized value. Aerodynamic damping normalization is done [47] by;

$$\sigma = \frac{W_{\text{cycle}}}{\omega^2 A_{\text{max}}^2} \quad (5.2)$$

where ω is the natural frequency of the specific mode, A_{max} is the amplitude of the maximum displacement which is 0.56 mm for a given mode. Non-normalized and normalized aerodynamic damping as a function of predetermined IBPAs are shown in Figure 5.7.

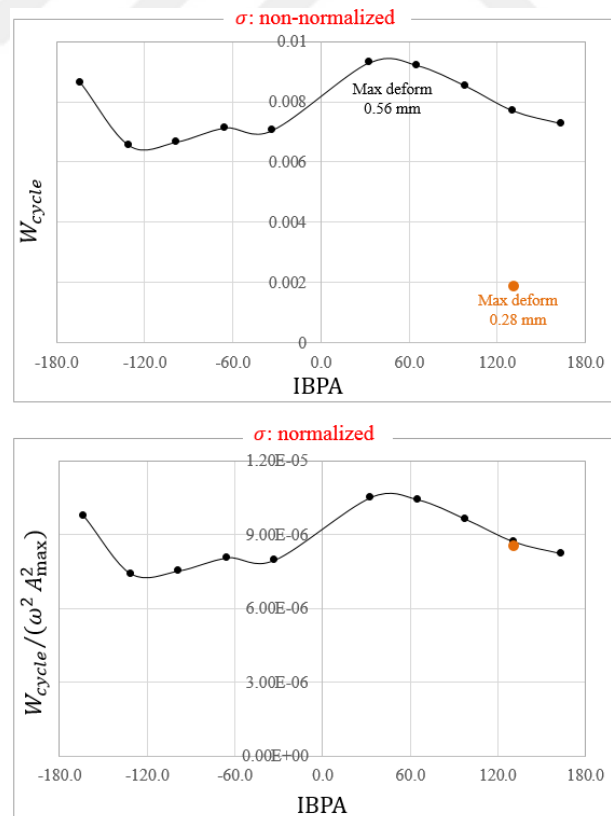


Figure 5.7 : Non-normalized and normalized aerodynamic damping as a function of several IBPA's near 25000 rpm.

As it is seen in Figure 5.7 that the most critical damping value is obtained at -4 ND corresponding to about -130° . However all modes were damped and therefore none of the damping results were used for Harmonic Response Analysis. It is important to note that positive damping values indicate that the blade vibration is damped, whereas negative damping values indicate that the vibration is not damped and rather excited. Therefore, the graphic shows that the mode is fully damped and no further vibration occurs.

Maximum deformation amplitude of the blade is 0.56 mm. However, damping result of the given mode with 0.5 scaled physical deformation (0.28 mm) shows discrepancy with nominal value of 0.56 mm in Figure 5.7. Yet, normalized damping result of 0.28 mm and 0.56 mm maximum deformations are almost equal. It proves that the damping is independent from the deformation amplitude (eigenvalue).

5.4 Unsteady Rotor-Stator Interaction Simulations

In parallel, unsteady rotor-stator interaction CFD simulations were performed in ANSYS CFX using Time Transformation method. The resulting mean (real) and oscillating (imaginary) pressure components were mapped on the rotor blade to be used as input for Harmonic Response Analysis.

5.5 Harmonic Response Analysis

Harmonic Response Analysis is an important method to determine the blade structure life cycle. It can be carried out with two ways;

- Modesuperposition Harmonic Analysis
- Full Harmonic Analysis

At first, modesuperposition harmonic analysis was studied. However, in ANSYS Mechanical software modesuperposition method appeared some problems. Instead, Full Harmonic Analysis which eliminates pre-stress effects was used. Note that, pre-stress effects in Harmonic Analysis have minor influence on the blade life cycle.

To perform the analysis, unsteady pressure mapping was imposed into Harmonic Response Analysis by real (mean) and imaginary (oscillating) pressure components. Mapped real and imaginary pressure can be seen in Figure 5.8.

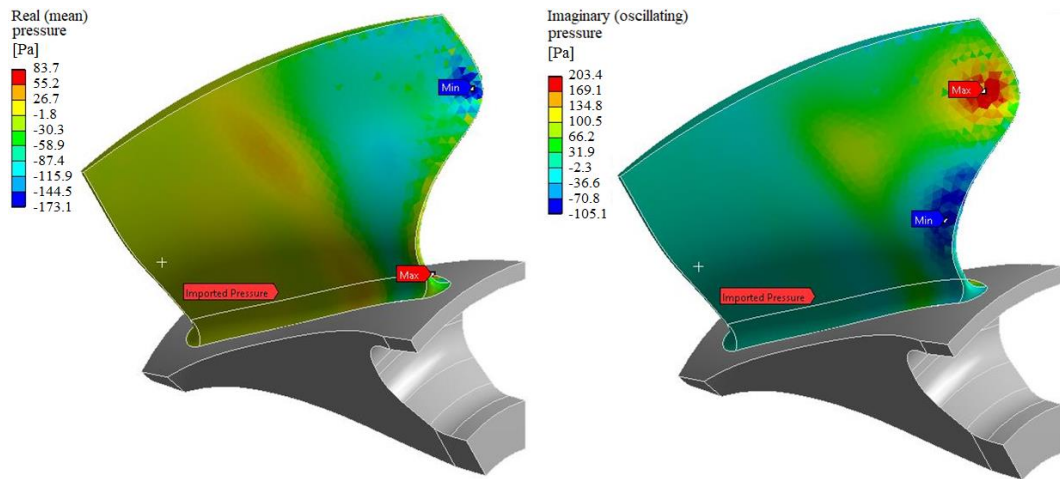


Figure 5.8: Unsteady complex real (left) and imaginary (right) pressure mapping.

The results are shown in figure 5.9 and 5.10. In Figure 5.9 the resulted deformation is about $10e-7$ mm level and can be avoidable. And maximum alternating stress is about 55 kPa that is based on stator excitation (see Figure 5.10). It was mentioned before that the results were obtained by considering only the unsteady stator blade excitation to rotor blade.

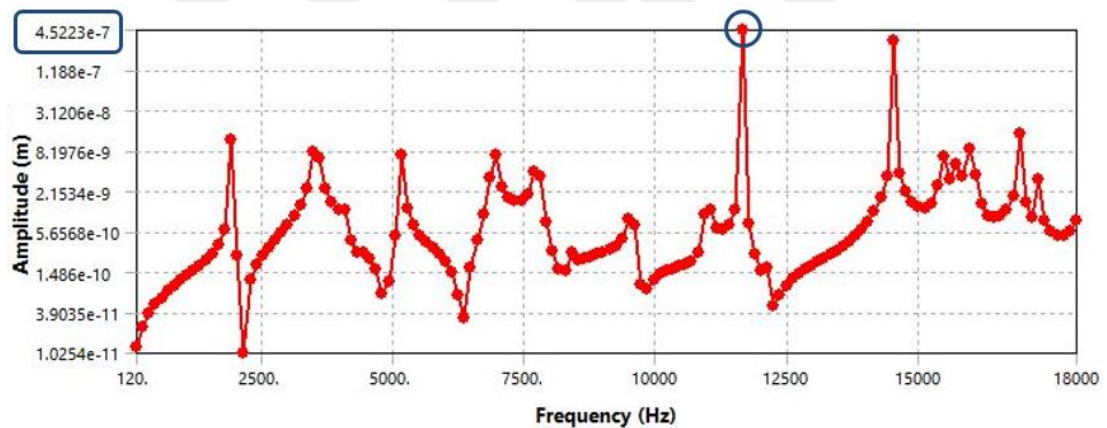


Figure 5.9: Deformation-frequency response graph.

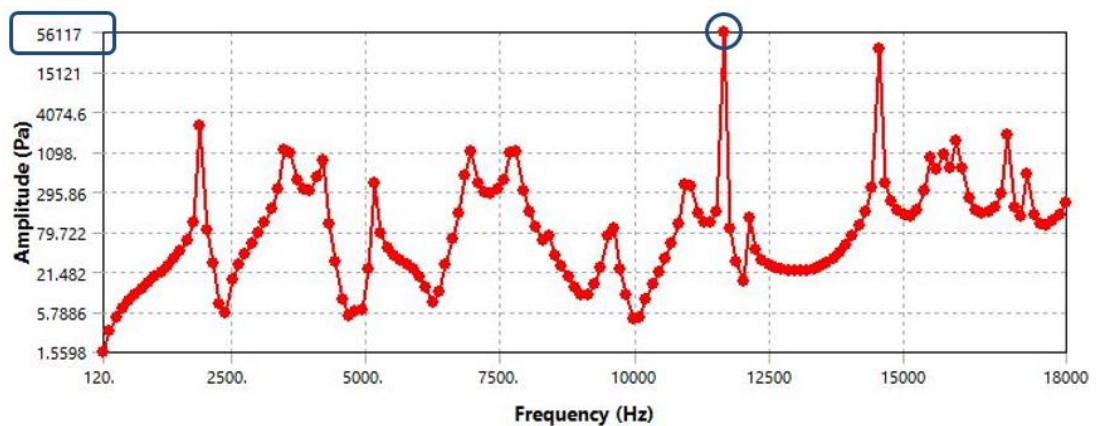


Figure 5.10: Alternating stress-frequency response graph.

From different studies [48; 49], alternating stress-life cycle graphics of Titanium alloy (Ti6A14V ELI) were evaluated. The results show that 55 kPa of maximum alternating stress is so small that could be avoidable in respect to life analysis. Therefore, it indicates that the rotor blade has an infinite life for the selected Titanium Alloy material.



6. CONCLUSION

A novel unified-LPC system for an adaptive micro-scaled turbofan engine was investigated in this thesis in every respect, from aerodynamic characteristics and positive functionality in point of thermodynamical performance to reliability of the system with the aeromechanical analyses. The studies showed that such a unified-LPC system is feasible and reliable for an existing micro-turbojet engine to be converted into an adaptive turbofan system.

At first, the unified-LPC components of highly-loaded transonic fan rotor blades and corresponding stator vanes were examined from aerodynamical perspective. Their aerodynamics characteristics were presented for different operations and various operating conditions. Furthermore, the effect of the highly-loaded fan stage on the core engine by the core duct was presented and some suggestion are made. Although, it was a challenging design and its thermodynamic requirements were difficult to be provided, the aerodynamical behaviour of the system proved its feasibility in micro-scaled turbofan engines. In the future, manually optimized stator design may be further optimized by considering more parameters within an optimization tool. Apart from that, the core and bypass ducts had been designed by an axisymmetric throughflow design tool [32] and the tool does not take into account the mixing losses. Utilizing from the aerodynamics investigation of the mixing flow behaviour of the LPC system, the ducts may further be optimized.

Secondly, an in-house map-based engine thermodynamic code was developed. The code was validated against the existing micro-turbojet engine. The results showed the positive functionality of the unified-LPC system by increasing the maximum thrust 105% and reducing the specific fuel consumption 33%. They were obtained for allowable 0.7 bypass ratio with variable gear ratio. For further studies, the code may be enhanced systematically. It may contain the engine's variable bypass ratio feature, altitude changes, and corresponding variable gear ratio parameter in its algorithm. The enhanced version of the code would be applicable for future UAV engines or even for larger scaled applications.

Finally, the aeromechanical investigations of such a challenging rotor of the unified-LPC was carried out. The results showed that the highest resonance was damped for all Inter Blade Phase Angles. This indicated a flutter-free rotor and its life cycle analysis showed an infinite life for the selected material. The reliability of the component for LPC system was therefore provided. However, in the further studies, the rest of the resonance points will be investigated in order to be ensured rotor's stability and structural integrity into the system. On the other hand, the aeromechanical study and methodology carried out in this thesis, expected to be instructive for researchers who desires to examine turbomachinery unsteady mechanical behaviour numerically in all respects.

In conclusion, such a novel LPC design is the first time in the open literature. The innovative concept and its investigation in this thesis is expected to present a unique guidelines for future UAV engine applications mainly and for future turbofan engines.

REFERENCES

- [1] Hooper, P. (2005). Stepped piston engines for multi-fuel UAV application. *IMEchE Conference on Propulsion Systems for Unmanned Aircraft*.
- [2] Lieh, J., Spahr, E., Behbahani, A., & Hoying, J. (2011, July). Design of hybrid propulsion systems for unmanned aerial vehicles. In *47th AIAA/ASME/SAE/ASEE Joint Propulsion Conference & Exhibit* (p. 6146).
- [3] Cirigliano, D., Frisch, A. M., Liu, F., & Sirignano, W. A. (2017). Diesel, Spark-Ignition, and Turboprop Engines for Long-Duration Unmanned Air Flights. *Journal of Propulsion and Power*, 34(4), 878-892. doi: <https://doi.org/10.2514/1.B36547>
- [4] Chiang, H. W. D., Hsu, C. N., Lai, A., & Lin, R. (2002, January). An investigation of steady and dynamic performance of a small turbojet engine. In *ASME Turbo Expo 2002: Power for Land, Sea, and Air* (pp. 1097-1104). American Society of Mechanical Engineers.
- [5] Collie, W., Burgun, R., Heinzen, S., Hall, C., & Chokani, N. (2003, January). Advanced propulsion system design and integration for a turbojet powered unmanned aerial vehicle. In *41st Aerospace Sciences Meeting and Exhibit* (p. 415).
- [6] Toal, D. J., Keane, A. J., Benito, D., Dixon, J. A., Yang, J., ... & Kill, N. (2014). Multifidelity multidisciplinary whole-engine thermomechanical design optimization. *Journal of Propulsion and Power*, 30(6), 1654-1666. doi: <https://doi.org/10.2514/1.B35128>
- [7] Copenhaver, W. W., Mayhew, E. R., Hah, C., & Wadia, A. R. (1996). The effect of tip clearance on a swept transonic compressor rotor. *Journal of turbomachinery*, 118(2), 230-239. doi: <https://doi.org/10.1115/1.2836630>
- [8] Benini, E., Biollo R. (2007, October). Aerodynamics of swept and leaned transonic compressor-rotors. *Journal of Applied Energy*, 84(10), 1012-1027. doi: <https://doi.org/10.1016/j.apenergy.2007.03.003>
- [9] Benini, E., & Biollo, R. (2008). Effect of forward and aft lean on the performance of a transonic compressor rotor. *International Journal of Turbo and Jet Engines*, 25(1), 13-26. doi: <https://doi.org/10.1515/TJJ.2008.25.1.13>
- [10] Passrucker, H., Engber, M., Kablitz, S., & Hennecke, D. K. (2003). Effect of forward sweep in a transonic compressor rotor. *Proceedings of the Institution of Mechanical Engineers, Part A: Journal of Power and Energy*, 217(4), 357-365. doi: <https://doi.org/10.1243%2F095765003322315414>
- [11] Michel, U. (2011). The benefits of variable area fan nozzles on turbofan engines. In *49th AIAA Aerospace Sciences Meeting including the New Horizons Forum and Aerospace Exposition*(p. 226). doi: <https://doi.org/10.2514/6.2011-226>
- [12] Hughes, C. E., Podboy, G., Woodward, R. P., & Jeracki, R. (2013). The Effect of Bypass Nozzle Exit Area on Fan Aerodynamic Performance and Noise in a Model Turbofan Simulator.

- [13] Wilfert, G., Sieber, J., Rolt, A., Baker, N., Touyeras, A., & Colantuoni, S. (2007, September). New environmental friendly aero engine core concepts. In *XVIII International Symposium of Air Breathing Engines, Beijing, China, Sept* (pp. 2-7).
- [14] Rolt, A. M., & Kyprianidis, K. (2010). Assessment of New Aero Engine Core Concepts and Technologies in the EU Framework 6 NEWAC Programme. In *ICAS 2010 Congress Proceedings, Paper No. 408*.
- [15] Goulas, A., Donnerhack, S., Flouros, M., Misirlis, D., Vlahostergios, Z., & Yakinthos, K. (2015). Thermodynamics cycle analysis, pressure loss, and heat transfer assessment of a recuperative system for aero-engines. *Journal of Engineering for Gas Turbines and Power*, 137(4), 041205. doi: <https://doi.org/10.1115/1.4028584>
- [16] Xu, L., Kyprianidis, K. G., & Grönstedt, T. U. (2013). Optimization study of an intercooled recuperated aero-engine. *Journal of Propulsion and Power*, 29(2), 424-432. doi: <https://doi.org/10.2514/1.B34594>
- [17] Kyprianidis, K. G., Rolt, A. M., & Grönstedt, T. (2014). Multidisciplinary analysis of a geared fan intercooled core aero-engine. *Journal of Engineering for Gas Turbines and Power*, 136(1), 011203. doi: <https://doi.org/10.1115/1.4025244>
- [18] Kyprianidis, K. G., & Rolt, A. M. (2015). On the optimization of a geared fan intercooled core engine design. *Journal of Engineering for Gas Turbines and Power*, 137(4), 041201. doi: <https://doi.org/10.1115/1.4028544>
- [19] Hendricks, E., & Tong, M. (2012, September). Performance and weight estimates for an advanced open rotor engine. In *48th AIAA/ASME/SAE/ASEE Joint Propulsion Conference & Exhibit* (p. 3911). doi: <https://doi.org/10.2514/6.2012-3911>
- [20] Alexiou, A., Roumeliotis, I., Aretakis, N., Tsalavoutas, A., & Mathioudakis, K. (2012). Modeling contra-rotating turbomachinery components for engine performance simulations: the geared turbofan with contra-rotating core case. *Journal of Engineering for Gas Turbines and Power*, 134(11), 111701. doi: <https://doi.org/10.1115/1.4007197>
- [21] Kadosh, K., & Cukurel, B. (2017). Micro-turbojet to turbofan conversion via continuously variable transmission: thermodynamic performance study. *Journal of Engineering for Gas Turbines and Power*, 139(2), 022603. doi: <https://doi.org/10.1115/1.4034262>
- [22] Royce, R. (1996). *The jet engine*. Foxit Reader.
- [23] Cengel, Y. A., & Boles, M. A. (2002). Thermodynamics: an engineering approach. *Sea*, 1000, 8862.
- [24] Cengel, Y. A. (2010). *Fluid mechanics*. Tata McGraw-Hill Education.
- [25] Baskharone, E. A. (2006). *Principles of turbomachinery in air-breathing engines*. Cambridge University Press.
- [26] Wu, C. H. (1952). *A general theory of three-dimensional flow in subsonic and supersonic turbomachines of axial-, radial, and mixed-flow types* (No. NACA-TN-2604). National Aeronautics and Space Administration Washington DC.
- [27] Palman, M., Leizeronok, B., & Cukurel, B. (2019). Mission Analysis and Operational Optimization of Adaptive Cycle Microturbofan Engine in Surveillance and Firefighting Scenarios. *Journal of Engineering for Gas Turbines and Power*, 141(1), 011010. doi: <https://doi.org/10.1115/1.4040734>

- [28] İlhan, M., Gürbüz, M. T., & Acarer, S. (2019). Unified low-pressure compressor concept for engines of future high-speed micro-unmanned aerial vehicles. *Proceedings of the Institution of Mechanical Engineers, Part G: Journal of Aerospace Engineering*, 0954410019840968. doi: <https://doi.org/10.1177%2F0954410019840968>
- [29] Karadimas, G. (1988). Design of high-performance fans using advanced aerodynamics codes. *Journal of turbomachinery*, 110(4), 419-425. doi: <https://doi.org/10.1115/1.3262214>
- [30] Bryce, J. D., Cherrett, M. A., & Lyes, P. A. (1993, May). Three-dimensional flow in a highly loaded single-stage transonic fan. In *ASME 1993 International Gas Turbine and Aeroengine Congress and Exposition* (pp. V001T03A002-V001T03A002). American Society of Mechanical Engineers. doi: <https://doi.org/10.1115/93-GT-003>
- [31] Acarer, S., & Özkol, Ü. (2019). Off-design analysis of transonic bypass fan systems using streamline curvature through-flow method. *International Journal of Turbo & Jet-Engines*, 36(2), 137-146. doi: <https://doi.org/10.1515/tjj-2016-0083>
- [32] ANSYS, CFX. (2017, August). *ANSYS CFX-Solver Theory Guide*: ANSYS, Inc. Software Documentations for Release 18.2.
- [33] Menter, F. R. (2009). Review of the shear-stress transport turbulence model experience from an industrial perspective. *International journal of computational fluid dynamics*, 23(4), 305-316. doi: <https://doi.org/10.1080/10618560902773387>
- [34] Suder, K. L. (1996). Experimental investigation of the flow field in a transonic, axial flow compressor with respect to the development of blockage and loss.
- [35] Mansour, M. L., Holbrook, G., Gunaraj, J., Qizar, M., & Mangat, V. (2008, January). Validation and calibration of modern CFD RANS codes for the prediction of transonic axial-centrifugal compressors. In *ASME Turbo Expo 2008: Power for Land, Sea, and Air* (pp. 385-392). American Society of Mechanical Engineers. Ddoi: <https://doi.org/10.1115/GT2008-50652>
- [36] Chima, R. (2009, February). SWIFT code assessment for two similar transonic compressors. In *47th AIAA Aerospace Sciences Meeting Including the New Horizons Forum and Aerospace Exposition* (p. 1058). doi: <https://doi.org/10.2514/6.2009-1058>
- [37] Giffin, R. G., Parker, D. E., & Dunbar, L. W. (1971, May). Experimental quiet engine program aerodynamic performance of Fan A. *NASA CR-120858*.
- [38] Dossena, V., Perdichizzi, A., & Savini, M. (1998, June). The influence of endwall contouring on the performance of a turbine nozzle guide vane. In *ASME 1998 International Gas Turbine and Aeroengine Congress and Exhibition* (pp. V001T01A022-V001T01A022). American Society of Mechanical Engineers. doi: <https://doi.org/10.1115/98-GT-071>
- [39] Dickens, T., & Day, I. (2011). The design of highly loaded axial compressors. *Journal of Turbomachinery*, 133(3), 031007. doi: <https://doi.org/10.1115/1.4001226>
- [40] Marn, A. (2008). On the aerodynamics of aggressive intermediate turbine ducts for competitive and environmentally friendly jet engines.
- [41] Fowler, T. W. (1989). *Jet Engines and Propulsion Systems for Engineers*. *GE Aircraft Engines, USA*.
- [42] Cumpsty, N. A. (1989). *Compressor aerodynamics* (No. BOOK). Longman Scientific & Technical.

- [43] Biollo, R. (2008). Systematic investigation on swept and leaned transonic compressor rotor blades.
- [44] Suder, K. L. (1997, June). Blockage development in a transonic, axial compressor rotor. In *ASME 1997 International Gas Turbine and Aeroengine Congress and Exhibition* (pp. V001T03A059-V001T03A059). American Society of Mechanical Engineers.
- [45] Kumar, A., & Pradeep, A. M. (2018, June). Performance Evaluation of a Tandem Rotor Under Design and Off-Design Operation. In *ASME Turbo Expo 2018: Turbomachinery Technical Conference and Exposition* (pp. V02AT39A009-V02AT39A009). American Society of Mechanical Engineers. doi: <https://doi.org/10.1115/GT2018-75478>
- [46] ANSYS, CFX. (2018). 18.0. *ANSYS CFX Tutorials*.
- [47] Elder, R., Woods, I., Patil, S., Holmes, W., Steed, R., & Hutchinson, B. (2013, June). Investigation of efficient CFD methods for the prediction of blade damping. In *ASME Turbo Expo 2013: Turbine Technical Conference and Exposition* (pp. V07BT33A009-V07BT33A009). American Society of Mechanical Engineers.
- [48] Prevéy, P. S., Hornbach, D. J., Jacobs, T. L., & Ravindranath, R. (2002). *Improved damage tolerance in titanium alloy fan blades with low plasticity burnishing* (No. N68335-01-C-0274). LAMBDA RESEARCH CINCINNATI OH.
- [49] Jayaraman, N., Prevey, P. S., & Ravindranath, R. (2005). *Improved damage tolerance of Ti-6Al-4V aero engine blades and vanes using residual compression by design*. LAMBDA RESEARCH CINCINNATI OH.

CURRICULUM VITAE

Muhammet Tayyip GÜRBÜZ

02-02-1990, İzmir/TURKEY

EDUCATION

M.Sc (2016-2019) : Mechanical Engineering, İzmir Katip Çelebi University

B.Sc (2009-2014) : Mechanical Engineering, Kocaeli University

P.S (2008-2009) : Preparation School (English), Kocaeli University

List of Publications:

- İlhan, M., Gürbüz, M. T., & Acarer, S. (2019). Unified low-pressure compressor concept for engines of future high-speed micro-unmanned aerial vehicles. *Proceedings of the Institution of Mechanical Engineers, Part G: Journal of Aerospace Engineering*, 0954410019840968. doi: <https://doi.org/10.1177%2F0954410019840968> (online published, in press)
- Gürbüz, M. T., İlhan, M., & Acarer, S., Karadeniz Z.H. (2019). Investigation of Radial Turbines for Wind Energy Harvesting *Proceedings of the Institution of Mechanical Engineers, Part A: Journal of Power and Energy*, JPE-19-0027.R1. (Accepted, in press)
- Kırmızıgöl, S.F., Gürbüz, M. T., İlhan, M., & Acarer, S., ‘Magnus Etkisi ile Çalışan Model Uçak Ön Tasarımı’ *Journal of R&D*, pp.48-49, March 2018-1, *Figes Engineering* (non-referee publication)

Conference Papers

- İlhan, M., Gürbüz, M. T., & Acarer, S., Karadeniz Z.H. ‘Radyal Türbin Mimarisinin Rüzgar Enerjisi Alanında Kullanımının Doğrulanmış Sayısal Akış Benzetimleri İle İncelenmesi’ *21st National Heating Science and Technique Congress September 13-16, 2017, Çorum/Turkey*
- Kırmızıgöl, S.F., Gürbüz, M. T., İlhan, M., & Acarer, S., ‘Magnus Etkisi ile Çalışan Model İHA Tasarımı, Simülasyonları ve İmalatı’ *VII. National Aviation and Space Conference, September 12-14 2018, Samsun/Turkey*
- Tatlı, Ö.F., Dursun, M.N., Gürbüz, M. T., & Acarer, S., ‘Düşey Kalkış Kabiliyetli Hibrit Rotorlu Model İHANın Ön İncelemesi’ *VII. National Aviation and Space Conference, September 12-14 2018, Samsun/Turkey*